Investigations in Formation and Properties of Spray-Dried Microparticles using Monodisperse Spray Drying

by

Zheng Wang

A thesis submitted in partial fulfillment of the requirements for the degree of

Master of Science

Department of Mechanical Engineering
University of Alberta

Abstract

The scaling up of monodisperse spray drying and the formation and properties of several spray-dried particle systems are investigated in this thesis. First, gallium focused ion beam milling was used to manufacture multi-orifice plates installed in a vibrating orifice atomizer in order to increase the production rate of the monodisperse spray drying. The dual-orifice plate achieved an average production rate of 23.8 ± 2.0 mg/hr for the model particles, allowing sufficient powder masses for microscopic and spectroscopic analysis, as well as particle fragility testing within a reasonable spray drying operation time. The monodispersity of the spray-dried particles using the dual-orifice plate was proved by an in-line aerodynamic particle sizer and scanning electron microscopy. These results demonstrate that multi-orifice plates are capable of increasing the powder production rate of monodisperse spray drying while maintaining the monodispersity of the spray-dried particles.

Second, the crystallization kinetics of spray-dried leucine particles from a co-solvent system were investigated using the scaled-up monodisperse spray drying. Leucine was dissolved in a water-ethanol co-solvent at ratios of 0.25/0.75, 0.5/0.5 and 1/0 w/w, and spray dried at inlet temperatures of 20, 40 and 80 °C. Numerical models were used to determine the time available for crystallization, which is an important parameter for predicting the crystallization kinetics at different co-solvent ratios and drying temperatures. Increasing the time available for crystallization correlated qualitatively with larger crystal size, more porous structure and lower particle fragility. These results highlight the importance of controlling crystal size and particle morphology via solvent environment and drying temperature during particle design and manufacturing processes for desired product properties.

Finally, various shell-forming excipients for dry powder dosage forms were investigated to maintain powder dispersibility when the powders are exposed to a high-humidity environment simulating an out-of-package scenario. Various combinations of trehalose with leucine, trileucine, or pullulan were selected as the candidate excipient systems and were compared with neat trehalose particles. Scaled-up monodisperse spray drying was used to produce sufficient powder masses for dispersibility testing. The powder dispersibility was characterized as the emitted dose from a dry powder inhaler. The results indicated that trehalose/leucine 70/30 w/w maintained the highest emitted dose of 90.3 ± 10% at a 60 L/min flow rate after 60 min exposure to 90% relative humidity and 25 °C compared with trehalose/pullulan 70/30 w/w and trehalose/trileucine 97/3 w/w, showing the superior protection of leucine against moisture. Further investigations under more challenging conditions at a 15 L/min flow rate on the trehalose/leucine system with various compositions (70/30, 80/20, 90/10 w/w) showed that higher leucine concentration generally provided better protection against moisture and maintained higher powder dispersibillity. Therefore, leucine may be considered an appropriate shell-forming excipient for dry powder dosage forms to maintain powder dispersibility against moisture during administration.

Preface

Chapter 2 of this thesis is a paper manuscript entitled “Morphology and Formation of Crystalline Leucine Microparticles from a co-Solvent System using Multi-Orifice Monodisperse Spray Drying,” submitted for publication under the authorship of Zheng Wang, Mani Ordoubadi, Hui Wang, and Reinhard Vehring. I was responsible for experimental design, data collection, data analysis, and manuscript composition. Mani Ordoubadi assisted with experimental design and data analysis, and contributed to manuscript edits. Hui Wang assisted with data collection and data analysis, and contributed to manuscript edits. Reinhard Vehring was the supervisory author at the University of Alberta and was involved in concept formation, discussion of results, and manuscript composition.

Chapter 3 of this thesis is a paper manuscript entitled “Leucine Enhances the Dispersibility of Trehalose-Containing Spray-Dried Powders on Exposure to a High Humidity Environment,” submitted for publication under the authorship of Zheng Wang, Hui Wang, and Reinhard Vehring. I was responsible for experimental design, data collection, data analysis, and manuscript composition. Hui Wang assisted with data collection and data analysis, and contributed to manuscript edits. Reinhard Vehring was the supervisory author at the University of Alberta and was involved in concept formation, discussion of results, and manuscript composition.

Acknowledgements

I would like to express my sincere gratitude to all who have helped me in this journey. Only with your help could I have completed my graduate studies successfully.

First and foremost, I would like to thank Dr. Reinhard Vehring for his supervision of my graduate studies. Dr. Vehring is an outstanding teacher who taught me a great deal about scientific research. He is also a mentor who has guided my critical thinking. Finally, Dr. Vehring has been a friend who always cared about me and my fellow-graduate students and treated us sincerely. I feel very lucky to have worked with him.

My thanks also go to my colleagues in the Particle Engineering group at the University of Alberta. They helped me without hesitation when I had difficulties, and I was constantly inspired by their wisdom. It was my great honor to work with and learn from them.

Special thanks go to the staff at the Nanofabrication and Characterization Facility at University of Alberta, in particular, Shihong Xu and Peng Li. Thanks to their expertise with the equipment and their patience training me, I was able to operate the equipment and obtain valuable results for my research. Special thanks also go to Luba Slabyj, who helped me edit my writing in every detail and was always happy to assist.

Last but not least, I would like to thank my parents, Ping Ye and Rongwei Wang, for their loving encouragement and their support of my studies. I would also like to thank Xinyu Kang for her sweetest company in this journey.

Table of Contents

List of Tables

List of Figures

Chapter 1. Introduction

Spray drying is a technique used to obtain dry powders by spraying liquid feeds into a hot drying gas stream (Sosnik and Seremeta 2015). This drying method was first introduced in 1860, and the first patent for spray drying was issued in 1872 (Cal and Sollohub 2010). So far, the spray drying process has been widely applied in the food (Shishir and Chen 2017; Tontul and Topuz 2017; Schmitz-Schug et al. 2016; Erbay et al. 2014) and pharmaceutical (Ziaee et al. 2019; Arpagaus et al. 2018; Sosnik and Seremeta 2015; Jain et al. 2012) industries. Conventional spray drying produces polydisperse particles of varying sizes, morphologies, aerodynamic properties, nutritional values, and other physicochemical properties. These variations may negatively influence the product quality in industrial applications and bring complexities to research studies. Therefore, monodisperse spray drying which is capable of producing particles with a narrow size distribution and similar morphologies and properties, becomes advantageous. Monodisperse spray drying utilizes monodisperse droplet generators to produce uniform droplets which are subsequently dried into particles. Due to the relatively low feed throughput of monodisperse droplet generators, the powder production rate of monodisperse spray drying is also relatively low. In a lab-scale monodisperse spray dryer equipped with a vibrating orifice atomizer (Ivey et al. 2018), the powder production rate is not sufficient for the sample requirements of some typical assays. As a result, increasing the powder production rate of monodisperse spray drying is necessary to achieve successful sample assays in research studies. With the help of scaled-up monodisperse spray drying, some particle systems which are complicated to study in a polydisperse model can then be studied in the monodisperse model with sufficient sample quantities for assays. For example, crystallization

kinetics of spray-dried crystalline particles, which are very sensitive to the initial droplet size, can be studied in a monodisperse model to reduce the complexities in the influence of the initial droplet size. Moreover, the internal distribution, structure and solid phase of two-component particle systems can also be affected by the initial droplet size, thus requiring monodisperse spray drying to precisely control the particle size in the investigations of these particle systems.

Chapter 1 of this thesis gives an introduction to the spray drying technique. In Chapter 2 of this thesis, multi-orifice plates are investigated to increase the powder production rate of monodisperse spray drying. A dual-orifice plate manufactured by gallium focused ion beam is shown to successfully increase the powder production rate while maintaining the monodispersity of the spray-dried particles. Using the scaled-up monodisperse spray drying, crystalline Leucine particles spray dried from a co-solvent system are investigated in a monodisperse model to study the crystallization kinetics and particle formation of crystalline spray-dried particles. In Chapter 3, the scaled-up monodisperse spray drying is also used to manufacture sufficient powders of various two-component particle systems to achieve enhanced robustness against moisture for nasal dry powder drug delivery. The dispersibility of the powders when exposed to a high relative humidity environment and the particle morphology and solid phases before and after exposure to moisture are investigated.

This thesis aims to investigate and utilize the scale up of monodisperse spray drying for the exploration of the formation and properties of several spray-dried particle systems. Two chapters of this thesis present work that has previously been prepared for publication as research articles.

1.1. Spray Drying

There are four fundamental steps in the spray drying process: (i) atomization of the liquid feed, (ii) contact of droplets and drying gas, (iii) drying of atomized droplets, and (iv) separation and collection of the dried particles from the drying gas. The details of the spray drying process are discussed in the following sections. A schematic of the conventional spray drying process is shown in Figure 1.

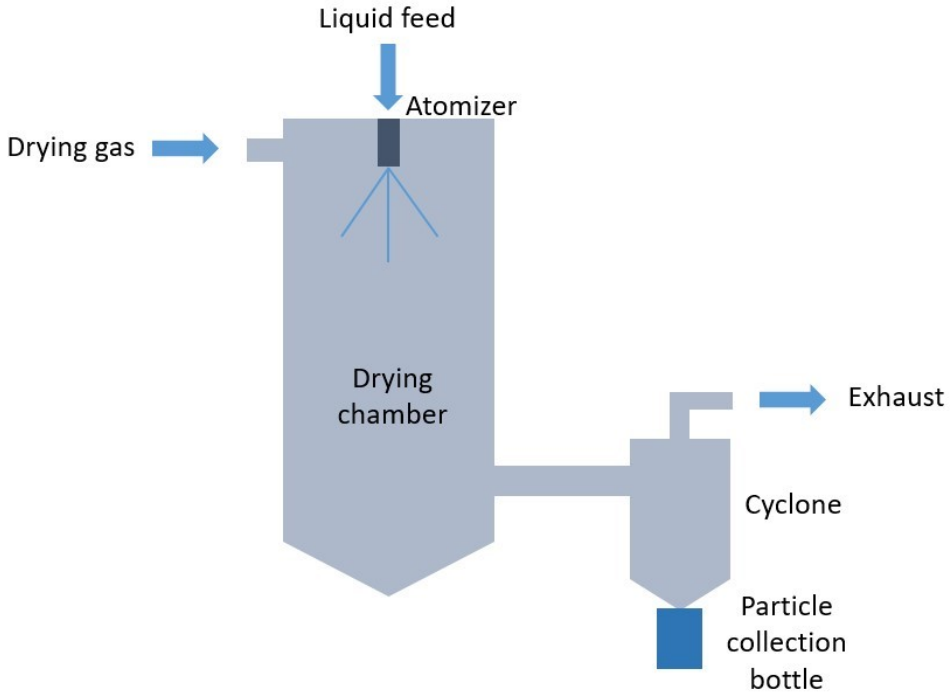

Figure 1 Schematic of the conventional spray drying process

1.1.1. Atomization of the liquid feed

In the first step, the liquid feed is atomized into spray or aerosol. The primary purpose of this step is to greatly increase the surface area of the liquid feed, thus leading to more efficient heat and mass

transfers (Tontul and Topuz 2017). Atomization can be achieved by different atomizers, including the three basic types: are rotary atomizers, hydraulic nozzles, and pneumatic nozzles (Tontul and Topuz 2017).

Rotary atomizers consist of a horizontally placed disc with radially oriented grooves. The disc is powered by an independent electric motor for rotation, with drive transmission devices. The liquid feed is supplied to the center of the rotating disc, where centrifugal force propels the liquid feed outwards, releasing it from the perimeter of the disc at a relatively high speed. Rotary atomizers are reliable, easy to operate and capable of handling fluctuating feed rates (Jain et al. 2012). Compared with other atomizers, rotary atomizers have relatively low production yield due to the higher fraction of deposition on the drying chamber, thus limiting its use for large-scale production of expensive feeds (Tontul and Topuz 2017; Huang et al. 2006).

Hydraulic nozzles, or one-fluid nozzles, are based on the principle of the pressurized fluid flowing through a nozzle with a decreasing diameter. The fluid flowing through the nozzle loses part of its pressure but gains velocity and undergoes atomization into droplets. Hydraulic nozzles can only be used for feeds with relatively low viscosities (Tontul and Topuz 2017). The feed rate is the only parameter in controlling and adjusting the performance of this type of nozzle, which greatly limits the ability to control the properties of final products (Cal and Sollohub 2010). The atomized droplets from hydraulic nozzles are generally less homogeneous than the droplets from rotary atomizers (Jain et al. 2012). Hydraulic nozzles also wear out more quickly and have a higher risk of clogging than other atomizers (Cal and Sollohub 2010).

Pneumatic nozzles, or multi-fluid nozzles, use compressed carrier gas to achieve the atomization of the liquid feed. Due to the high frictional forces between the liquid feed and the compressed gas, the liquid feed disintegrates into droplets. Two-fluid nozzles that use one atomizing gas (usually air) and one liquid feed are widely used for pharmaceutical applications. The key parameter of this type of atomizer is the air-to-liquid ratio, which is the ratio of the mass flow of the compressed air to the mass flow of the liquid feed. The droplet diameter depends on the air-to-liquid ratio, gas properties, liquid feed properties, and nozzle design.

Besides the three conventional types of atomizers, other atomizers are also available. Ultrasonic nozzles utilize ultrasonic waves to create vibrations and atomize the liquid feed. The advantages of ultrasonic nozzles include the ability to self-clean, wide control over the atomized droplet size, and narrow droplet size distribution (Cal and Sollohub 2010). The droplet size depends on the working frequency and remains constant if the frequency does not change. In addition, low velocities of the atomized droplets decrease the likelihood of chamber wall deposition and thus increase the production yield (Tontul and Topuz 2017; Cal and Sollohub 2010).

1.1.2. Contact of droplets and drying gas

The contact of droplets and drying gas takes place in the drying chamber immediately after the atomization step. The hot drying gas contacts the liquid spray, prompting droplet evaporation and drying. Heat and mass transfer then take place simultaneously. Heat is transferred from the drying gas to droplet by convection, while vapor is transported from the droplet to drying gas by convection

(Wisniewski 2015). Momentum is also exchanged between droplets and drying gas if they have different velocities before contact. Subsequently, the relative velocity between droplets and drying gas becomes very small, and droplets move along with the drying gas stream.

Regarding the direction of the liquid feed atomization with respect to the direction of the drying gas flow, spray drying can be classified into three models: co-current , counter-current , and mixed. In the co-current model, the liquid feed is sprayed in the same direction as the drying gas. The final dried particles are in contact with the coolest drying gas; thus heat-sensitive materials are preferred (Sosnik and Seremeta 2015). In the counter-current model, the liquid feed is sprayed in the opposite direction of the drying gas. The atomized droplets come into contact with the coolest drying gas first, ensuring a gradual increase in the droplet temperature (Tontul and Topuz 2017). This model is desirable for its high thermal efficiency but cannot be used with heat-sensitive materials (Sosnik and Seremeta 2015). In the mixed model, both co-current flow and counter-current flow are used in the drying process (Tontul and Topuz 2017; Sosnik and Seremeta 2015).

The operation configurations in spray drying can be either open-cycle or closed-cycle. In an open-cycle spray drying, the drying gas is not re-circulated. This configuration is preferred in most of the cases due to its higher stability and cost-effectiveness (Sosnik and Seremeta 2015). In a closed-cycle the drying gas, which is usually an inert gas (e.g. nitrogen), is recycled after the particles are collected and re-heated into drying gas again. This configuration is used to avoid the mixing of explosive gases and the reactions of oxygen-sensitive substances (Sosnik and Seremeta 2015).

1.1.3. Dying of atomized droplets

Drying of droplets takes place as the droplets evaporate. Initially the droplet has a nearly constant evaporation rate. Due to the heat transfer, the drying gas temperature decreases rapidly, while the droplet surface temperature remains almost unchanged due to the latent heat of evaporation and could be represented by the wet bulb temperature (Wisniewski 2015). The partial water vapor pressure is also nearly constant during this time period (Tontul and Topuz 2017; Wisniewski 2015). At a certain moisture content precipitation takes place, and the drying rate decreases and becomes dependent on the water diffusion rate (Tontul and Topuz 2017). The temperature of the droplet increases, and when the drying process is complete the temperature of the dried particle is close to that of the surrounding gas (Tontul and Topuz 2017; Wisniewski 2015).

1.1.4. Separation and collection of the dried particles from the drying gas

The final step takes place in the particle separation and collection system, which has to be designed to match the drying gas flow rate, particle size distribution, and powder load (Wisniewski 2015). The most common particle separation and collection systems include cyclones, bag filters, scrubbers, and electrostatic precipitators (Tontul and Topuz 2017). The most commonly used separation device, the cyclone, separates the solid particles from the drying gas by centrifugal force created through the rapid rotating of the drying gas. The particles move towards the wall of the device and are separated from the drying gas core at the central axis of the device. The particles then impact on the wall and fall down due to gravity into the collection bottle at the bottom of the device. The cyclone cut-off diameter depends on the drying gas flow rate, gas viscosity, cyclone diameter, and a cyclone

configuration factor. The cyclone cut-off diameter needs to be verified experimentally. Generally, smaller cyclone cut-off diameters can be achieved with smaller cyclone diameters or with a larger drying gas flow rate. Bag filters stop the movement of the particles when they pass through the fabric along with the drying gas. An appropriate filtering unit with bag filters may be capable of separating particles with a diameter < 1 μm (Cal and Sollohub 2010). Scrubbers can be used to collect the particles that deposit on the wall of drying chamber. Electrostatic precipitators, which operate on the principle of electrostatic fields to separate particles, are rarely used due to their high cost (Cal and Sollohub 2010).

1.2. Particle Engineering

Particle engineering, which combines elements from different fields of science, provides the theoretical knowledge for the design of microparticles for different applications. Particle engineering is necessary and even critical in acquiring a deeper understanding of the particle formation process since it is difficult to use only empirical approaches in particle designs with so many process parameters, especially for complex structured microparticles. While many different methods can be used to manufacture microparticles, this thesis focuses exclusively on particle engineering via spray drying. The theory of particle engineering via spray drying has been developed and discussed previously in detail (Vehring 2008; Vehring et al. 2007), and a brief summary of this research is given in the following sections.

1.2.1. Particle size

Most spray-dried particles can be considered spherical, and their size can be described in terms of geometric diameter, d_g. The geometric diameter is an important parameter since it affects the forces acting on the particles in fluid flows and the packing of particles in powder form. It is also frequently used as a reference since it can be directly accessed through ultramicroscopic techniques. In respiratory delivery, the aerodynamic diameter, d_a, is a critical parameter defined as the equivalent diameter of a unit-density sphere with the same settling velocity as the measured particle. The aerodynamic diameter can be related to the geometric diameter by

$$d_a = \sqrt{\frac{\rho_P}{\rho^*}} d_g \tag{1}$$

where ρ_P is the particle density, and ρ^* is the unit density, 1 g/cm^3. Equation (1) is valid for spheres in the continuum regime. The particle density can be calculated by dividing the mass of the particle by the volume of a sphere of diameter d_g. The particle density can be significantly lower than the true density of the dried material since it includes internal and external voids (Vehring 2008). Using a simple mass balance, the geometric diameter of the dry particle can also be expressed as

$$d_g = \sqrt[3]{\frac{c_F}{\rho_P}} d_D \tag{2}$$

where c_F is the feed solution concentration, and d_D is the droplet diameter. Combining equation (1) and (2), we get

$$d_a = \sqrt[6]{\frac{\rho_P}{\rho^*}} \sqrt[3]{\frac{c_F}{\rho^*}} d_D \tag{3}$$

Equation (3) shows that the aerodynamic diameter of the spray-dried particle is most effectively controlled by the initial droplet diameter and also by the feed solution concentration, while it is a weak function of the particle density. We should understand the point that changes in the droplet size distribution and the feed solution concentration, which may be encountered in the scale-up

process, can lead to a significant change in the aerodynamic properties of the spray-dried particles.

1.2.2. Distribution of components in spray-dried particles

The most critical part of particle engineering is to understand and control the mechanisms that how components distribute during spray drying process. The radial distribution of components is determined by several different driving forces. Surface activity of the component may cause a diffusional flux toward the droplet surface, while the receding surface of an evaporating droplet can cause increased solute concentration at the surface, leading to a diffusional flux toward the center of the droplet. The diffusional motions of all the components inside the evaporating droplet should be well understood if the distribution of the components in spray-dried particles is to be properly predicted.

Without internal convection, the distribution of the components in an evaporating droplet can be determined using a non-linear diffusion equation. If the diffusion coefficient is constant and interactions between the solutes are negligible, the diffusion equation becomes Fick's second law of diffusion. If the droplet evaporates at a constant evaporation rate, this equation has an analytical solution. The evaporation rate, κ, is defined as

$$d^2(t) = d_0^2 - \kappa t \tag{4}$$

Using equation (4), the droplet drying time, or droplet lifetime, can be approximated by

$$\tau_{\mathrm{D}} = \frac{d_0^2}{\kappa} \tag{5}$$

A dimensionless Peclet number, Pe, is defined as

$$Pe_i = \frac{\kappa}{8D_i} \tag{6}$$

The Peclet number is a very useful parameter in predicting the distribution of the components in the evaporating droplets and spray-dried particles. The Peclet number can be used to derive the surface enrichment, E_i:

$$E_i = \frac{c_{\mathrm{s},i}}{c_{\mathrm{m},i}} = \frac{e^{\frac{Pe_i}{2}}}{3\beta_i} \tag{7}$$

The surface enrichment is defined as the ratio of the surface concentration, $c_{\mathrm{s},i}$, to the mean concentration in the droplet, $c_{\mathrm{m},i}$. β is a function that must be integrated numerically. In its place, an analytical approximation accurate within 1% in the range of $Pe < 20$ can be used:

$$E_i = \frac{c_{\mathrm{s},i}}{c_{\mathrm{m},i}} \approx 1 + \frac{Pe_i}{5} + \frac{Pe_i^2}{100} - \frac{Pe_i^3}{4000} \tag{8}$$

Equations (7) and (8) are based on the assumption that solute concentration at any point inside the evaporating droplet changes at the same rate as the mean concentration, a state known as asymptotic (Boraey and Vehring 2014). This assumption may not be valid for relatively large Peclet numbers. An improved version of the model with more accuracy for relatively large Peclet numbers has been discussed elsewhere (Boraey and Vehring 2014).

Another very useful parameter, $\tau_{\mathrm{sat},i}$, the time for a component to reach saturation at the droplet surface, can be expressed as

$$\tau_{\mathrm{sat},i} = \tau_{\mathrm{D}}\left(1 - \left(S_{0,i}E_i\right)^{\frac{2}{3}}\right) \tag{9}$$

where $S_{0,i}$ is the initial saturation of the component, defined as the ratio of the initial concentration of the component, $c_{0,i}$, to the solubility of the component, $c_{\mathrm{sol},i}$:

$$S_{0,i} = \frac{c_{0,i}}{c_{\mathrm{sol},i}} \tag{10}$$

1.3. Monodisperse Spray Drying

The conventional atomizers discussed in the previous sections usually generate polydisperse droplets and spray-dried particles. The typical droplet size for spray drying with rotary atomizers, hydraulic nozzles, pneumatic nozzles, and ultrasonic nozzles ranges from 1-600, 10-800, 5-300, and 5-1000 μm, respectively (Wu et al. 2007). The polydisperse droplets with wide size distributions may have different trajectories inside the drying chamber, leading to different drying kinetics and possible droplet-droplet and droplet-wall collisions. Thus, the spray-dried particles may have different particle sizes, densities, shapes, structures, etc. However, the uniformity of particles is important in certain industries, e.g. functional food products, pharmaceuticals, and catalysts (Wu et al. 2007). The accuracy and reproducibility of designed particle models in research are also negatively influenced by the polydispersity of the particles.

One way to maintain uniformity of particles is to produce droplets with a very narrow size distribution that follow similar and simple trajectories (Wu et al. 2007). This can be achieved by using a monodisperse droplet generator (MDG) in a regular spray dryer. The MDG is capable of producing highly uniform droplets while keeping simple droplet trajectories, which leads to uniform spray-dried particles. In addition, due to the uniform size and simple trajectories, the droplet drying process is more controllable and predictable, and collisions between particles and the dryer wall that may cause product loss and energy waste are reduced. In the following sections, the principles of monodisperse droplets generation as well as some existing types of MDGs are introduced.

1.3.1. Principles of monodisperse droplet generation

The generation of monodisperse droplets is achieved by a breakup of the uniform liquid jet. Plateau derived the minimum unstable wavelength of the disturbances on an infinitely long liquid cylinder as (Plateau 1873):

$$\lambda_{\min} = \pi d_{\mathrm{j}} \tag{11}$$

where d_{j} is the diameter of the cylindrical liquid jet. For an inviscid, incompressible, cylindrical liquid jet in vacuum, Rayleigh derived the optimal wavelength for the most unstable disturbances as (Rayleigh 1878):

$$\lambda_{\mathrm{opt}} = 4.508 d_{\mathrm{j}} \tag{12}$$

From the mass balance of the disintegrated liquid cylinder section and the final droplet, we can derive the geometric diameter of the droplets as

$$\frac{\pi}{6}\rho d_{\mathrm{D}}^3 = \frac{\pi}{4}\rho d_{\mathrm{j}}^2 \lambda \;\Rightarrow\; d_{\mathrm{D}} = \sqrt[3]{\frac{3}{2}\lambda d_{\mathrm{j}}^2} \tag{13}$$

where λ is the wavelength of the disturbance. When equations (12) and (13) are combined, the geometric diameter of the droplets for the most unstable disturbances is derived as

$$d_{\mathrm{D,opt}} = 1.89 d_{\mathrm{j}} \tag{14}$$

Weber extended the theory by taking the viscosity of the liquid into account and providing a relationship for the optimal wavelength of the disturbance for viscous jets (Weber 1931):

$$\lambda_{\mathrm{opt,v}} = \sqrt{2}\pi\left(1 + \frac{3\mu_{\mathrm{l}}}{\sqrt{\rho_{\mathrm{l}}\sigma d_{\mathrm{j}}}}\right) \tag{15}$$

where μ_{l} is the viscosity of the liquid, ρ_{l} is the density of the liquid, and σ is the surface tension coefficient of the liquid.

Different disintegration mechanisms are observed as a function of the liquid flow rate, which can be classified into four primary breakup regimes--the Rayleigh regime, the first wind-induced regime, the second wind-induced regime, and the atomization regime (Dumouchel 2008; Lin, S P and Reitz 1998). Among these regimes, the droplets that break up in the Rayleigh regime are the most uniform, stable and organized. Therefore, the disintegration of the droplets should be kept in the Rayleigh regime to produce monodisperse droplets. It was reported that the Rayleigh regime can be achieved if the following conditions are met (Sterling and Sleicher 1975; Ranz 1956):

$$We_{\mathrm{L}} = \frac{\rho_{\mathrm{l}} v_{\mathrm{j}}^2 d_{\mathrm{o}}}{\sigma} > 8; \tag{16}$$

$$We_{\mathrm{G}} = \frac{\rho_{\mathrm{g}} v_{\mathrm{j}}^2 d_{\mathrm{o}}}{\sigma} < 0.4 \ \text{ or } \ 1.2 + 3.41 \left(\frac{\mu_{\mathrm{l}}}{\sqrt{\rho_{\mathrm{l}} d_{\mathrm{o}} \sigma}}\right)^{0.9} \tag{17}$$

where v_{j} is the jet velocity, d_{o} is the nozzle diameter which can be considered as equivalent to the jet diameter, and ρ_{g} is the gas density.

1.3.2. Monodisperse droplet generators

Depending on the types of disturbances, MDGs can be classified into three basic categories: electro-hydrodynamic droplet generators (EHDGs), thermo-hydrodynamic droplet generators (THDGs), and mechano-hydrodynamic droplet generators (MHDGs) (Liu et al. 2015).

EHDGs use an electric field for the atomization of droplets. Due to the electric field, the liquid at the nozzle tip gains surface charge and transforms into a conical meniscus, called a Taylor cone. A thin jet is then ejected from the apex of the cone and subsequently disintegrates into droplets. The droplet diameter is smaller than the orifice diameter, and the droplet size distribution is very narrow (Wu et al. 2007). One advantage of producing droplets smaller than the orifice diameter is the lower

risk of clogging of the orifice (Liu et al. 2015).

THDGs utilize thermal energy to produce pressure pulses and achieve droplet generation. A heating element generates heat pulses that vaporize a small amount of liquid and cause the formation of gas bubbles. The gas bubbles then collapse due to condensation when moving to colder areas in the liquid. The continuous formation and collapse of the gas bubbles produce pressure pulses, leading to monodisperse droplet generation. THDGs are not suitable for heat-sensitive ingredients due to the heating process. Since the pressure pulses are determined by the formation and collapse of the gas bubbles, which are difficult to control, THDGs lack the capability of optimizing the monodispersity of the droplets. Moreover, compared with other types of MDGs, THDGs require more time for single droplet generation, which could lead to a low production rate (Liu et al. 2015).

MHDGs rely on mechanical energy for droplet breakup. One type of MHDG uses shear force generated by an external flowing fluid to produce monodisperse droplets. Through solvent extraction and evaporation, monodisperse particles can be achieved. Another type of MHDG uses vibration force generated by piezoelectric transducers to disintegrate the liquid jet into droplets. The piezoelectric transducer is controlled by a frequency generator to vibrate at a certain frequency. With an appropriate vibrating frequency, the liquid jet can break up into droplets with a narrow size distribution. One advantage of the piezoelectric transducer is its precise control over the disturbances, thus the monodispersity of the droplets can be optimized. As one type of MHDG which does not use thermal energy in the atomization process, piezoelectric-driven MHDGs are also compatible with heat-sensitive materials. However, the manufacturing of piezoelectric-driven

MHDGs is rather complicated, and the clogging of the orifice may be encountered during the droplet generation process (Liu et al. 2015).

Chapter 2. Morphology and Formation of Crystalline Leucine Microparticles from a co-Solvent System using Multi-Orifice Monodisperse Spray Drying

2.1. Introduction

Spray drying, a process to obtain dry powders by spraying liquid feeds into drying gas, is widely applied in the food (Shishir and Chen 2017; Tontul and Topuz 2017; Schmitz-Schug et al. 2016) and pharmaceutical (Ziaee et al. 2019; Arpagaus et al. 2018; Sosnik and Seremeta 2015) industries. Manufactured powders are often required to have specific properties for different applications. For example, efficient respiratory delivery requires particles sized within the respirable range (1-5 μm) (Mehanna et al. 2014), ideally with low-density and improved dispersibility (Vehring 2008), and with protection against moisture-induced deterioration in aerosolization performance (Li et al. 2016), etc. Although spray drying is a one-step process, particle formation during spray drying is complex and affected by many variables and processes. Therefore, in order to design target particles that can be readily manufactured, it is critical for particle engineering to draw on the necessary particle formation theory (Vehring 2008).

The liquid feed for spray drying can be in the form of a solution, emulsion, or suspension (Gharsallaoui et al. 2007). In solution-based spray drying, the droplet surface recedes quickly as the liquid droplets evaporate, promoting higher surface concentrations. Meanwhile, the solutes diffuse from the droplet surface towards the low-concentration core (Boraey and Vehring 2014). When the solute concentration at the droplet surface reaches the solubility limit, i.e. surface saturation, precipitation on the droplet surface can begin (Vehring 2008). For a crystallizing excipient,

nucleation can commence when a specific level of supersaturation is reached, the value of which is a function of solvent composition and drying conditions. The time available for crystallization, which is considered as the time window for crystal nucleation, crystal growth, and polymorphic transformation, is an important parameter in crystallization kinetics since it can greatly influence the particle properties and morphologies (Ordoubadi et al. 2019; Baldelli et al. 2016). The time available for crystallization is dependent on the initial feed concentration, initial droplet size, solubility, and evaporation rate. The initial feed concentration can be well controlled through careful feed preparation, and the initial droplet size is a known function of atomizer settings. However, the solubility and evaporation rate can change significantly, depending on the solvent environment.

A Co-solvent system has frequently been used in spray drying to manipulate the solubility of pharmaceutical actives and excipients in order to obtain reasonable feed concentration (Boraey et al. 2013; Carr et al. 2011). Unlike the evaporation rate in a single solvent system, the evaporation rate in a co-solvent system can change (Ordoubadi et al. 2019). As a result, there can be great differences between the two types of systems in the time available for crystallization, leading to different crystallization kinetics and consequently different particle properties. The polymorphic forms of spray-dried particles can also be different in co-solvent systems, depending on the crystallization kinetics and the nature of the solvent system (Lee et al. 2011). Numerous studies have investigated the crystallization process of spray-dried particles. For instance, McDonagh investigated the crystallization of paracetamol particles spray dried from a water/ethanol co-solvent system and correlated the particle size, density, and morphology with the inlet temperature of the spray drying and the ethanol concentration of the feed (McDonagh and Tajber 2019). Lu

investigated the droplet shrinkage, particle morphology, and polymorphic forms of mannitol particles spray-dried from an aqueous solution, correlating these characteristics with initial droplet size and feed concentration (Lu et al. 2020). Baldelli studied the influence of the crystallization process on the properties of sodium nitrate particles spray dried from an aqueous solution (Baldelli et al. 2016). The study found that longer time available for crystallization caused larger crystal size, higher crystallinity, a higher void fraction, and lower particle density. Ordoubadi developed numerical methods to study the evaporation kinetics and internal diffusion of multi-solvent droplets in spray drying for particle formation applications (Ordoubadi et al. 2019). In Ordoubadi's study, Leucine was spray dried from a water/ethanol co-solvent system at the same drying temperature (20 ℃) and different water/ethanol ratios (1/0, 0.75/0.25, 0.5/0.5, 0.25/0.75 w/w). The dimensionless values of the time available for crystallization were correlated with the initial ethanol mass fraction. Different particle morphologies were observed and correlated with the initial ethanol mass fraction and ethanol mass fraction at saturation. An interesting new morphology featuring a porous structure with crystals growing into the center of the particle was observed at the highest initial ethanol mass fraction. However, the precise details of crystallization kinetics in a co-solvent system, including crystal growth mechanisms and resulting crystal size and the correlation between crystallization kinetics and the time available for crystallization in a co-solvent system, require further investigation. Therefore, this study extends the previous work of (Ordoubadi et al. 2019) for a fundamental study of the morphology and formation of spray-dried crystalline leucine particles with an emphasis on crystal growth and particle formation mechanisms.

The time available for crystallization is very sensitive to the initial droplet size, which leads to

additional complexity if the droplets are not uniform. As a result, crystallization kinetics and particle formation can be better studied in monodisperse model systems. The monodisperse droplet chain and monodisperse spray drying are two techniques commonly used to produce monodisperse droplets and dried particles. The monodisperse droplet chain uses a piezoceramic dispenser and produces monodisperse droplets when triggered by a pulse signal generated from a function generator. Droplets are injected into a heated airflow in a flow tube equipped with an imaging system for analysis of the initial droplet diameter. Dried particles are collected for characterization at the end of the flow tube using a membrane filter. A monodisperse droplet chain instrument has been discussed in detail elsewhere (Ordoubadi et al. 2019). Since monodisperse droplet chains produce droplets at each pulse signal, which is typically in the 100 Hz range, the production rates are much smaller than 1 mg/hr (Vehring et al. 2007). By contrast, monodisperse spray drying achieves a much higher production rate. Monodisperse spray drying systems consist of a monodisperse droplet generator and a spray dryer. Many different types of monodisperse droplet generators have been reported (Liu et al. 2015), and one type utilizing vibration forces generated by piezoelectric transducers has been commonly used in research studies (Rogers et al. 2012b, 2012a; Fu et al. 2011). A custom-designed vibrating orifice atomizer (Azhdarzadeh et al. 2016) integrated with a custom laboratory spray dryer (Wang et al. 2019; Ivey et al. 2018) has been discussed previously in detail. In this system, the pressurized liquid feed formed a liquid jet through an orifice plate installed in the atomizer. The jet then disintegrated into monodisperse droplets under a specific frequency provided by a function generator. Compared with the monodisperse droplet chain dispenser, the vibrating orifice atomizer operated with a much higher vibration frequency in the 100-200 kHz range (Wang et al. 2019). As a result, monodisperse spray drying is able to produce over a thousand times more

droplets, and consequently more final product, than the monodisperse droplet chain within the same time. However, the production rate of monodisperse spray drying is still not sufficient for the sample requirements of many typical powder assays. Thus, increasing the powder production rate of monodisperse spray drying becomes important and beneficial for particle design and characterization in research studies.

Certain multi-orifice designs have previously been shown to increase the production rate of monodisperse spray drying (Wu et al. 2007). Patel and Chen proposed a design of multiple ink-jet devices (Patel and Chen 2007) that can be grouped and mounted on the same plate to produce monodisperse droplets simultaneously. Each ink-jet device can be placed in an individual nozzle and supplied with liquid feed using individual tubing. However, this design of multiple ink-jet devices is not compatible with the custom spray dryer currently in use in our lab (Wang et al. 2019), and the re-design and re-manufacturing of the hardware is very time-consuming. Brenn designed a 62-hole plate to produce 62 liquid jets simultaneously and used laser drilling for manufacturing (Brenn et al. 1996). A liquid throughput up to 13.7 L/h was achieved using this nozzle plate. The diameter of the laser drilled holes was 63 μm with 400 μm between adjacent holes. The droplet size ranged from 123 μm to 181 μm depending on the working frequency, and the monodispersity of the droplets was confirmed by visual observation. This multi-orifice design is compatible with the custom vibrating orifice atomizer currently in use in our lab (Wang et al. 2019); however, using laser drilling to manufacture micro-orifices carries some technical limitations. The orifices manufactured by laser drilling have been shown to have rough and irregular edges (Brenn et al. 1996) that can change the geometry of the orifice, thereby affecting performance; they can also

make the orifice difficult to reproduce. This problem of rough and irregular edges becomes more significant for smaller orifices, greatly limiting the use of laser drilling in the manufacture of very small orifices. Moreover, for a multi-orifice plate, in which each orifice should ideally be identical in order to produce monodisperse droplets, the rough and irregular edges can negatively influence the uniformity of the orifices and consequently the monodispersity of the produced droplets. By contrast, the technique of gallium focused ion beam (Ga-FIB) milling is capable of patterning and machining on a sub-micron level, thus allowing for higher resolution fabrication than laser drilling. This fact provided another motivation of this study, which was to develop custom multi-orifice plates with cleaner orifice edges and smaller orifice sizes using Ga-FIB milling.

The primary aim of this study was to investigate the crystallization kinetics of crystalline particles spray dried from a co-solvent system using monodisperse spray drying in order to acquire a deeper understanding of particle morphology and the particle formation process. In addition, given the low production rate of monodisperse spray drying, this study also aimed to develop multi-orifice plates in order to increase the production rate by using Ga-FIB milling for cleaner orifice edges and smaller orifice sizes than those in commercial laser-drilled orifice plates. Since this study also aimed for the fragility testing of the spray-dried particles, it was necessary to produce and collect sufficient powders from the cyclone. Increasing the production rate of monodisperse spray drying, was therefore, a necessary component of this study investigating the performance of crystalline leucine particles. Ga-FIB milling was used to manufacture the orifices on a thin stainless-steel plate, and scanning electron microscopy was used to observe the orifice edges. A custom vibrating orifice atomizer and custom laboratory spray dryer (Wang et al. 2019) were used to produce monodisperse

particles. Leucine was selected as the crystallizing excipient since it was found to form fully crystalline particles from spray drying when it was the only solute (Feng et al. 2011; Lucas et al. 1999). Water/ethanol was selected as the co-solvent, not only because its use is common but, more importantly, because clear morphological differences in spray-dried leucine particles produced by a water/ethanol system as compared to an aqueous system (Ordoubadi et al. 2019) required further investigation. Leucine was dissolved in a water/ethanol co-solvent at different water/ethanol ratios and spray dried at different inlet temperatures. Numerical methods in previous work (Ordoubadi et al. 2019) were used to predict the droplet evaporation rate, internal solute transfer, and other droplet drying kinetics in the co-solvent spray drying. The crystallinity of the spray-dried leucine particles was confirmed using Raman spectroscopy, and the particle morphology was analyzed using scanning electron microscopy.

2.2. Materials and Methods

2.2.1. Materials

L-Leucine (Cat. No. BP385-100, Acros Organics BVBA, Geel, Belgium) was dissolved in demineralized water and ethanol to prepare the feed solutions for monodisperse spray drying. Two different water/ethanol ratios, 0.25:0.75 w/w water/ethanol and 0.5:0.5 w/w water/ethanol, were chosen in this study and compared with a control system of 100% water. The feed solution concentration of leucine, 0.5 mg/mL, was the same for all formulations. The co-solvent ratios and feed solution concentration were chosen because clear morphological differences were reported previously using these parameters (Ordoubadi et al. 2019), and this study aimed for further investigation of the reasons for these differences.

2.2.2. Monodisperse Spray Drying using a Dual-Orifice Plate

The monodisperse spray drying setup used in this study has been discussed previously in detail (Ivey et al. 2018). Briefly, a vibrating orifice atomizer was supplied with pressurized feed solution to generate monodisperse droplets. A dual-orifice plate with two 30-µm-diameter orifices was installed in the atomizer to form two separate liquid jets. A piezoelectric ceramic ring attached to the atomizer head was actuated by a function generator to vibrate at a certain frequency. Control of the jet exit velocity through the pressure difference across the orifice and the driving frequency achieved an optimal monodisperse droplet disintegration in Rayleigh jet disintegration regime, whereby the liquid jet disintegrates regularly into droplets of very similar diameter (Azhdarzadeh et al. 2016; Dumouchel 2008). Dispersing air was used to disperse the droplets in a turbulent gas jet in order to minimize droplet collisions. The tendency for droplet collisions increases as the distance between droplets decreases; therefore the distance between droplets should be maximized (Brenn et al. 1997). One method of achieving such maximized droplet distance is to use air to disperse the newly formed droplets right after disintegration from the liquid column. A droplet dispersion system was designed previously for this purpose (Liu et al. 2011). In this study a similar design was used in which air flows through a dispersing cap integrated with the atomizer and disperses the droplets, thus reducing the droplet collisions and maintaining the monodispersity of the spray-dried particles. A schematic of the vibrating orifice atomizer using a dual-orifice plate is shown in Figure 2. The inlet drying gas temperature was set to 20 °C, 40 °C and 80 °C for different formulations. The droplets were then dried into solid particles in a custom lab-scale spray dryer (Ivey et al. 2018) and collected in a glass bottle using a stainless-steel cyclone separator. The cyclone had a cylinder-on-cone design with a tangential inlet. The drying gas flow rate was set to 0.5 m^3/min to ensure efficient collection of

particles larger than 1 µm. The heat loss to surroundings generally depended on the inlet temperature, outlet temperature, and the Reynolds number in the drying chamber. From previous characterization experiments (Ivey 2018), the heat loss at a 0.5 m^3/min drying gas flow rate and inlet temperatures of 20 °C, 40 °C and 80 °C was determined to be around 0 kW, 0.06 kW and 0.22 kW, respectively. The liquid throughput was measured gravimetrically by using a small glass vial to collect the water flowing through the orifices in 2 min. Table 1 lists the detailed spray drying parameters. Table 2 lists all the formulations that were spray dried in this study.

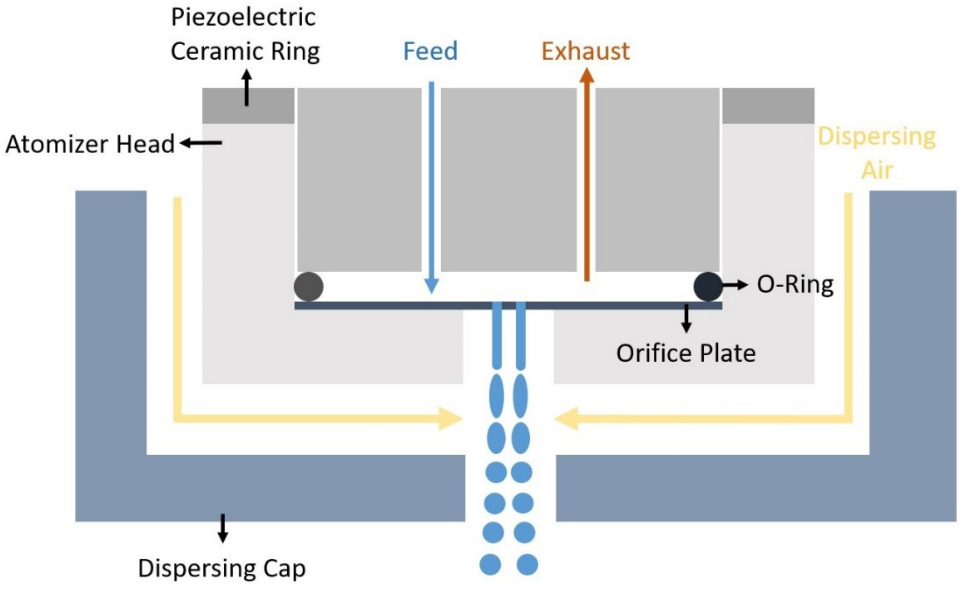

Figure 2 Schematic of the vibrating orifice atomizer using a dual-orifice plate

Table 1 Spray drying parameters

Parameter	Value
Pressure difference across orifice	100-200 kPa
Micro-orifice diameter	30 µm
Feed solution temperature	20 ± 1 °C
Inlet/outlet temperature	20 °C/20 °C, 40 °C/32 °C, 80 °C/56 °C (±1 °C)
Disperser cap orifice diameter	3.0 mm
Dispersing gas pressure	275 kPa
Dispersing gas flow rate	0.293 g/s
Dispersing gas temperature	20 ± 1 °C
Drying gas flow rate	0.5 m^3/min

Piezoelectric driving frequency	90 ± 10 kHz
Drying chamber diameter	0.2 m
Drying chamber height	1.85 m

Table 2 Formulations with drying temperatures

Feed concentration of leucine (mg/mL)	Water/ethanol w/w	Drying temperature (°C)
0.5	0.25/0.75	20
	0.25/0.75	40
	0.25/0.75	80
	0.5/0.5	20
	0.5/0.5	40
	0.5/0.5	80
	1/0	80

2.2.3. Powder Production Rate

The powder production rate for monodisperse spray drying using a single-orifice plate, $\dot{m}_{\mathrm{s}}$, was estimated as (Ivey et al. 2018)

$$\dot{m}_{\mathrm{s}} = c_{\mathrm{s}} Q = c_{\mathrm{s}} C_{\mathrm{d}} \frac{\pi d_{\mathrm{o}}^2}{4} \sqrt{\frac{2\Delta p}{\rho_{\mathrm{l}}}} \tag{18}$$

where c_{s} is the solids concentration of the feed solution, C_{d} is the discharge coefficient of the orifice, d_{o} is the orifice diameter (assuming a circular orifice), Δp is the pressure difference across the orifice and ρ_{l} is the liquid density. The discharge coefficient, C_{d}, is defined as the ratio of the actual or experimental flow rate to the theoretical flow rate. The discharge coefficient does not change significantly during atomization (assuming no clogging occurs) and varies only with different orifice geometry (Bayvel and Orzechowski 1993); thus it can be considered close to a constant for orifices with the same geometry. For example, the discharge coefficient is typically in the range of 0.7-0.8 for the circular orifice used in the vibrating orifice atomizer.

As shown in equation (18), the powder production rate is a function of three parameters: the solids

concentration of the feed solution, the orifice diameter, and the pressure difference across the orifice. However, for applications in respiratory drug delivery, particles with a specific aerodynamic diameter, d_a, are required, which is not explicitly expressed in the equation. Therefore, equation (18) was rearranged into a function containing d_a as following:

The solids concentration of the feed solution is related by (Vehring 2008) to the aerodynamic diameter of the spray-dried particle and the droplet diameter, d_D:

$$d_a = \left(\frac{\rho_P}{\rho_0}\right)^{\frac{1}{6}} \left(\frac{c_s}{\rho_0}\right)^{\frac{1}{3}} d_D \tag{19}$$

Here ρ_P is the particle density and ρ_0 is the unit density, 1 g/cm^3. The droplet diameter is related to the jet diameter, d_j, by (Rayleigh 1878):

$$d_D = 1.89 d_j = 1.89 d_o \tag{20}$$

This equation assumes that the vibrating orifice is operated with the optimal disturbance frequency and that the jet diameter is equivalent to the orifice diameter.

Equations (19) and (20) together give a relationship between d_a, c_s, and d_o which is

$$d_a = 1.89 \left(\frac{\rho_P}{\rho_0}\right)^{\frac{1}{6}} \left(\frac{c_s}{\rho_0}\right)^{\frac{1}{3}} d_o \tag{21}$$

The powder production rate using a multi-orifice plate is proportional to the number of orifices, *N*, since multiple liquid jets are produced simultaneously.

By combining equations (18) and (21), the powder production rate using a multi-orifice plate can be expressed as

$$\dot{m}_{s,N} = 0.165 C_d N \frac{d_a^3}{d_o} \sqrt{\frac{\rho_0^3}{\rho_l \rho_P} \Delta p} \tag{22}$$

For respiratory drug delivery, a specific target aerodynamic diameter of the particle is required in the range of 1-5 μm (Mehanna et al. 2014). From equation (22), the powder production rate for a given aerodynamic diameter of the spray-dried particle can only be increased by increasing the

pressure difference across the orifice, decreasing the orifice diameter, and increasing the number of orifices. The pressure difference across the orifice is limited by the mechanical strength of the orifice plate in order to avoid rupturing the orifice. In addition, monodisperse droplet generation relies on the Rayleigh disintegration regime (Azhdarzadeh et al. 2016; Dumouchel 2008), which places an upper limit on the jet exit velocity. The jet exit velocity is related to the pressure difference across the orifice, which also carries an upper limit in order to ensure monodisperse droplet generation. Decreasing the orifice diameter is another option to increase the powder production rate, and small orifices are desirable to produce respirable particles. Typical feed concentrations in spray drying of respirable products are limited to the range of 10-100 mg/mL, due to the solubility limitations of the actives and excipients. The aerodynamic diameter of respirable particles is limited to the range of 1-5 μm. Thus, from equation (21), the ideal orifice diameter in this case is in the range of 1-10 μm. However, as previously mentioned, it is difficult to manufacture orifices in this size range with clean orifice edges and good reproducibility (especially at the lower end) by using laser drilling. As a result, Ga-FIB milling was investigated to manufacture small orifices in this study. The last and also the best way to increase the powder production rate is to increase the number of the orifices. Multi-orifice plates can only work ideally if each orifice is identical to ensure monodisperse droplet generation. Again, laser drilling has its limitations in manufacturing uniform orifices, and Ga-FIB milling was investigated to manufacture multi-orifice plates.

Ga-FIB milling (Zeiss Orion HiM w/ Ga-FIB, Zeiss, Jena, Germany) was used to manufacture orifices on a 13-μm-thick circular stainless-steel plate. The aperture size of the Ga-FIB was 500 μm and the current was 30 nA. Dwell time was 5 μs. The node style was mitered, and the alignment

was outside/in. These equipment parameters were chosen to optimize the manufacturing quality while keeping the manufacturing time within a reasonable range. Using these parameters, the average milling time for one 30-µm orifice was around 25 min. Ideally, more orifices are preferred on the plate, but due to the rather long operation time and high cost of the equipment the dual-orifice plate was manufactured in the early stage of this study and used to produce the model particles. The orifice diameter was 30 µm and the distance between the two orifices was around 200 µm. This is two times larger than the minimum distance between orifices reported by (Brenn et al. 1996) as necessary to ensure separate liquid jets, which is around three times the orifice diameter.

2.2.4. Numerical Model for Droplet Evaporation and Diffusion Kinetics

Determining the droplet evaporation and diffusion kinetics during spray drying is a complicated mass and heat transfer problem, especially for the multi-solvent system. Numerical methods to predict the droplet evaporation rate and internal solute transfer in the multi-solvent system have previously been discussed in detail (Ordoubadi et al. 2019). In this study, numerical methods utilizing the Stefan-Fuchs model in conjunction with Fick's law of diffusion were used to calculate droplet evaporation and diffusion kinetics and to determine leucine concentration profiles inside the evaporating droplets. To model the evaporation of a single droplet, the Maxwell model neglects the radial convective fluxes around the droplet, while the Stefan-Fuchs model takes these radial convective fluxes into consideration, which gives more accurate results at higher temperatures and, therefore, was used in this study. To model the internal diffusion of the solute, Fick's law of diffusion was used. The numerical model is based on a well-mixed approximation which assumes the solvent compositions and temperatures are constant throughout the droplet, since the mass diffusivity of a

molecule such as leucine is at least one order of magnitude larger than that of ethanol and water and also the heat diffusivity. The numerical model also assumes zero partial pressure of the vapor in the drying gas. It is worth noting that the model is only valid up to the point of crystallization. With these assumptions, the generated numerical data agreed with the experimental data with only small differences (Ordoubadi et al. 2019). As a summary, the total evaporation rate of multi-solvent droplets, $\dot{m}_t$, was calculated from

$$\dot{m}_t = -2\pi d \rho_{\mathrm{t}} D_{\mathrm{g,m}} \ln\left(\frac{y_{\infty,\mathrm{g}}}{y_{\mathrm{s,g}}}\right) \tag{23}$$

in which d is the droplet diameter, ρ_{t} is the total gas density around the droplet, and $D_{\mathrm{g,m}}$ is the diffusion coefficient of the inert gas in the vapor mixture. $y_{\infty,\mathrm{g}}$ and $y_{\mathrm{s,g}}$ are the inert gas mass fractions under ambient conditions and near the droplet surface, respectively. The evaporation rate of each component, $\dot{m}_i$, was then calculated as

$$\dot{m}_i = \dot{m}_t \frac{y_{\infty,i}\beta_i - y_{\mathrm{s},i}}{\beta_i - 1} \tag{24}$$

where $y_{\infty,i}$ and $y_{\mathrm{s},i}$ are the vapor mass fractions of each component under ambient conditions and near the droplet surface, respectively; β_i can be approximated as $\left(\frac{y_{\mathrm{s,g}}}{y_{\infty,\mathrm{g}}}\right)^{\frac{D_{\mathrm{g,m}}}{D_{i,\mathrm{m}}}}$. Here $D_{i,\mathrm{m}}$ is the diffusion coefficient of each component in the vapor and gas mixture around the droplet.

Based on the total evaporation rate and the density of the liquid mixture, the diameter of the droplet was updated at each instance and the evaporation rate of the droplet was calculated from

$$\kappa = -\frac{\mathrm{d}d^2}{\mathrm{d}t} \tag{25}$$

The following modified Fick's law of diffusion for the inside of an evaporating droplet was then solved in conjunction with the appropriate boundary and initial conditions (Ordoubadi et al. 2019):

$$\frac{\partial C_j}{\partial t} = \frac{4D_j}{d^2}\left(\frac{\partial^2 C_j}{\partial R^2} + \frac{2}{R}\frac{\partial C_j}{\partial R}\right) - \frac{\kappa R}{2d^2}\frac{\partial C_j}{\partial R} \tag{26}$$

Here R is the radial coordinate non-dimensionalized by the instantaneous droplet radius, C_j is the

concentration of each solute at each radial location and D_j is the diffusion coefficient of each solute inside the droplet. For the water/ethanol co-solvent system, D_j can be approximated by

$$D_j\sqrt{\eta_{\mathrm{m}}} = x_{\mathrm{l,w}}D_{j,\mathrm{w}}\sqrt{\eta_{\mathrm{l,w}}} + x_{\mathrm{l,eth}}D_{j,\mathrm{eth}}\sqrt{\eta_{\mathrm{l,eth}}} \quad (27)$$

where η_{m}, $\eta_{\mathrm{l,w}}$ and $\eta_{\mathrm{l,eth}}$ are the liquid viscosities of the mixture, water, and ethanol at the droplet temperature, respectively; $x_{\mathrm{l,w}}$ and $x_{\mathrm{l,eth}}$ are the mole fractions of water and ethanol in the droplet, respectively; $D_{j,\mathrm{w}}$ and $D_{j,\mathrm{eth}}$ are the diffusion coefficients of solute *j* in water and ethanol, respectively. This equation also captures that the diffusion coefficient of each solute in the mixture depends not only on the solvent composition, but also on the droplet temperature which is affected by the drying temperature.

The surface concentration of each solute was then compared to the solubility of the solute at the respective solvent composition to find the appropriate particle formation parameters, such as the available time for crystallization.

2.2.5. Time Available for Crystallization

An important parameter to predict the crystallization kinetics during spray drying is the time available for crystallization, t_{c}, which is defined as (Ordoubadi et al. 2019; Baldelli et al. 2016)

$$t_{\mathrm{c}} = t_{\mathrm{D}} - t_{\mathrm{s}} \quad (28)$$

where t_{D} is the total lifetime of the droplet and t_{s} is the time for the solute to reach saturation. The time available for crystallization can be considered as the time window available for nucleation and crystal growth. As the droplet shrinks during evaporation, the solute concentration increases on the droplet surface, generally faster than inside the droplet (Vehring 2008; Vehring et al. 2007), and

reaches saturation there first, causing crystallization to start at the surface. Thus, in this study t_{s} is defined as the time from atomization to the point where the surface saturation of leucine reaches 1. However, nucleation may not happen instantaneously when the surface saturation reaches 1, and a certain level of supersaturation is usually required to trigger nucleation (Baldelli and Vehring 2016a). Therefore, an additional time point, namely the time to reach critical supersaturation at which the nucleation can commence instantaneously, is also important in determining the time available for crystallization (Ordoubadi et al. 2020). Based on the time to reach critical supersaturation, the time available for crystallization can be determined by

$$t_{\mathrm{c}}^{*} = t_{\mathrm{D}} - t_{\mathrm{n}} \tag{29}$$

where t_{n} represents the time to reach critical supersaturation. To determine this time point, the value of critical supersaturation, S_{n}, must be obtained first. He et al. proposed a model based on an evaporating droplet crystallization platform to predict the critical supersaturation at which nucleation can commence instantaneously (He et al. 2006). Based on the model, the critical supersaturation can be approximated by solving the following equation

$$\ln^3 S_{\mathrm{n},i} + \left[\ln\left(A_i/J_{\mathrm{n},i}\right)\right]\left[\ln^2 S_{\mathrm{n},i}\right] - B_i = 0 \tag{30}$$

where A_i is the diffusion-limited nucleation rate, $J_{\mathrm{n},i}$ is the nucleation rate at the point of critical supersaturation, and B_i is the thermodynamic parameter, defined as

$$B = \frac{16\pi v_{\mathrm{m},i}^2 \sigma_i^3}{3(kT)^3} \tag{31}$$

where $v_{\mathrm{m},i}$ is the volume of the solute molecule, σ is the surface energy of the solute in the solution, k is the Boltzmann constant, and T is the solution temperature in Kelvins. As noted in (He et al. 2006), the surface energy has a strong correlation with the solubility $C_{\mathrm{sol},i}$; thus the following correlation was used (Christoffersen et al. 1991)

$$\frac{\sigma_i d_{\mathrm{m},i}^2}{kT} = \frac{1}{\pi} \ln\left(\frac{\rho_i}{\gamma_{\mathrm{sol},i} C_{\mathrm{sol},i}}\right) \tag{32}$$

where $d_{\mathrm{m},i}$ is the molecular diameter calculated using the molecule volume, ρ_i is the crystal density, and $\gamma_{\mathrm{sol},i}$ is the activity coefficient of the solvent in the presence of the solute molecules at saturation. With the assumption of spherical molecules ($v_{\mathrm{m},i} = \frac{\pi}{6} d_{\mathrm{m},i}^3$), equation (31) and (32) can be combined, giving the following equation:

$$B = \frac{4}{27} \ln^3\left(\frac{\rho_i}{\gamma_{\mathrm{sol},i} C_{\mathrm{sol},i}}\right) \tag{33}$$

It was found by He et al. that $\ln\left(A_i / J_{\mathrm{n},i}\right)$ was almost constant for various compounds (~5.15), allowing an approximation of the critical supersaturation as a function of crystal and solution properties. For leucine in an aqueous solution, the crystalline leucine density, $\rho_{\mathrm{leu}} = 1293$ mg/mL, and the aqueous solubility, $C_{\mathrm{sol,leu}} = 22$ mg/mL at 25 °C, can be used to calculate the critical supersaturation (Ordoubadi et al. 2020). In addition, the activity coefficient of water in the presence of leucine molecules at saturation was estimated to be 1 (Ordoubadi et al. 2020). With these values inserted into equation (30), the critical supersaturation of leucine in an aqueous solution was determined to be equal to 3.5, indicating that leucine is expected to nucleate instantaneously at a supersaturation of 3.5 in a water droplet.

Assuming that the same methodology can be extended to multi-solvent systems, the surface energy of a solute, i, in a co-solvent system, σ_i, can be approximated from

$$\sigma_i = \sum x_j \sigma_{i,j} \tag{34}$$

where x_j is the mole fraction of the *j*th solvent, and $\sigma_{i,j}$ is the surface tension in pure solvent *j* obtained from equation (32). Hence the thermodynamic parameter can be written as

$$B = \frac{4}{27} \ln^3\left[\prod_j \left(\frac{\rho_i}{\gamma_{\mathrm{sol},ij} C_{\mathrm{sol},ij}}\right)^{x_j}\right] \tag{35}$$

where $\gamma_{\mathrm{sol},ij}$ is the solvent activity coefficient at the solubility concentration of the solute in the

jth solvent and $C_{\mathrm{sol},ij}$ is the solubility of the solute in the jth solvent. If these crystal and solution parameters are known, the critical supersaturation of the solute in a multi-solvent system can be determined. For example, given the leucine solubility of about 0.72 mg/mL in ethanol (PubChem n.d.) and assuming the activity coefficient to be equal to 1, the thermodynamic parameter of leucine in a water/ethanol mixture at 0.25/0.75 w/w water/ethanol is calculated to be about 30.7, and the solution of equation (30) gives the critical supersaturation $S_{\mathrm{n}} = 7.9$ or a concentration of 16.5 mg/mL with a solubility of about 2.1 mg/mL (Ordoubadi et al. 2019) in this solvent composition. Therefore, leucine is expected to nucleate instantaneously at the supersaturation of 7.9 in the water/ethanol 0.25/0.75 w/w solvent composition. Upon reaching the critical supersaturation point, we assume that the nucleation commences instantaneously, and the nucleation rate is sufficiently large. It is worth noting that this critical supersaturation point is not the onset of instability (the spinodal point) as this point falls inside the metastable region. Modeling or measurement of this is beyond the scope of this study. These supersaturation values were determined assuming the solvent composition remains constant, while the solvent composition may change during spray drying, which will be discussed later.

2.2.6. Particle Size Measurement

Particle size was measured in-process with an aerodynamic particle sizer (APS) (Model: 332100, TSI, Shoreview, USA) during spray drying (Wang et al. 2019). Briefly, a sampling port regulated by a two-way valve was opened immediately before every size measurement, and the APS was set to operate in-line at a standard flow rate of 5 L/min. The drying gas flow rate was reduced from the standard 0.5 m^3/min to 0.1 m^3/min during particle size measurement to prevent over-pressurizing

the APS. Particle size was measured every 15 min during spray drying, with each spray drying run typically taking 3-4 hours. Each measurement took 20 s to collect enough particles (>200 counts) to generate a particle size distribution.

2.2.7. Electron Microscopy

Microscopic images of the orifice plates were taken using a scanning electron microscope (SEM) (EVO M10, Zeiss, Jena, Germany). The orifice plates were placed on the SEM stubs for imaging. An accelerating voltage of 10 kV and working distance of 9-10 mm were used to capture the images. The orifice diameter was measured based on the SEM images using ImageJ software (ImageJ 1.53a, National Institutes of Health, USA).

Morphology of the spray-dried particles was analyzed using a field emission scanning electron microscope (FESEM) (Zeiss Sigma FESEM, Zeiss, Jena, Germany). Briefly, each particle sample was first placed on a SEM stub with a double-sided adhesive carbon tape to prevent an electron charging effect. The samples were then coated using a gold sputter (Desk II Gold Sputter, Denton Vacuum, NJ, USA) for 120 s. The in-lens detector, an accelerating voltage of 4-5 kV, and a working distance of 5-7 mm were used to capture the images.

2.2.8. Particle Crystallinity

A custom Raman spectroscopy system (Wang et al. 2017, 2019) was used to verify the solid phase of the spray-dried leucine particles. An aluminum sample holder with a conical cavity volume of 0.2 μL was used to load the collected sample powders for analysis. This setup utilized a 671 nm diode-pumped laser (Ventus 671, Laser Quantum, UK) with a maximum power of 500 mW. All

sample powders were analyzed under a nitrogen atmosphere with less than 3% RH at room temperature (21 ± 1 °C). Raw L-leucine material was measured directly and used as the crystalline reference. The spectrum of the saturated aqueous solution of L-leucine after subtracting the spectrum of water was used as the Raman reference for amorphous L-leucine (Feng et al. 2011) because an amorphous leucine powder reference could not be manufactured. Characteristic peaks of the reference spectra were used to determine the solid phase of L-leucine.

2.3. Results and Discussion

2.3.1. Multi-Orifice Plate

SEM images of the dual-orifice plate manufactured by Ga-FIB and two commercial orifice plates manufactured by laser drilling (Precision Pinhole, Edmund Optics, USA) are shown in Figure 3. The laser-drilled orifices had many irregular edges, and the geometry of one laser-drilled orifice was also irregular. These orifices with irregular edges and geometry were observed to produce deflected jets, leading to collisions between adjacent jets and subsequent loss of monodispersity in the spray-dried particles. By contrast, the dual-orifice plate manufactured by Ga-FIB had much cleaner orifice edges and regular orifice geometry. The diameter of the two orifices on the dual-orifice plate was measured as 31.2 ± 0.5 μm and 31.0 ± 0.6 μm respectively, showing that the two orifices were of a very similar size. These results can be expected since Ga-FIB provides higher resolution fabrication than laser-drilling. With clean orifice edges, regular geometry and similar orifice sizes, the dual-orifice plate is expected to produce monodisperse droplets and particles.

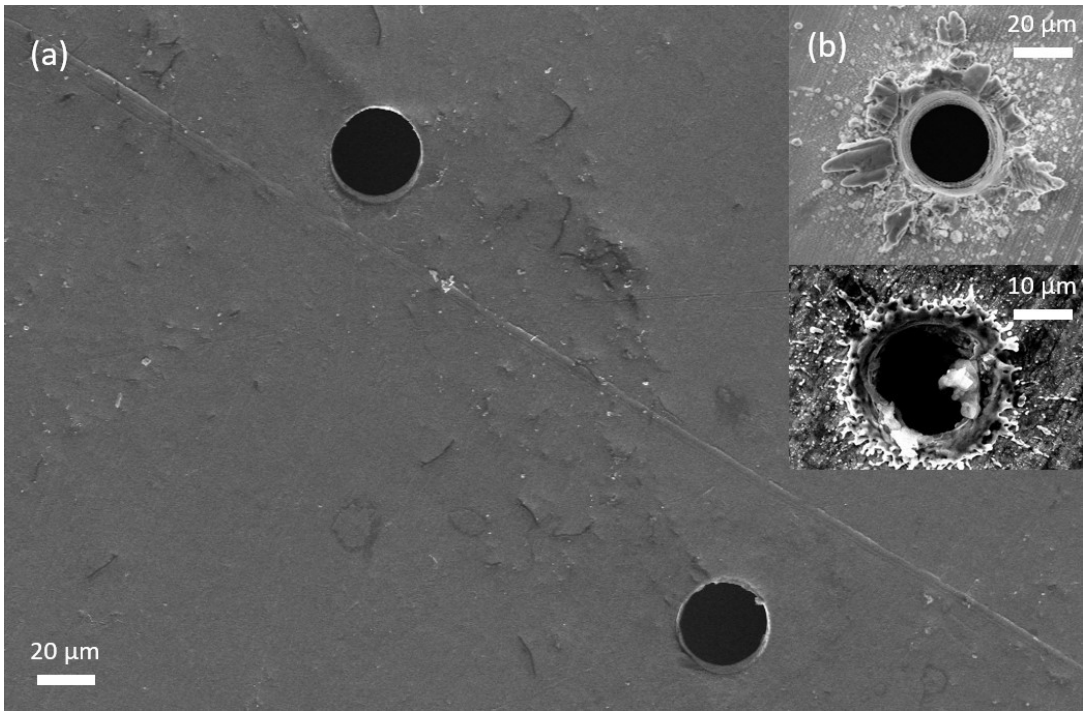

Figure 3 SEM image of orifice plate: (a) dual-orifice plate manufactured by Ga-FIB (b) commercial single-orifice plates manufactured by laser drilling. The laser-drilled orifices with irregular edges and geometry were observed to produce deflected jets, leading to collisions between adjacent jets and subsequent loss in the monodispersity of spray-dried particles.

A typical aerodynamic diameter distribution of spray-dried leucine particles using the dual-orifice plate is shown in Figure 4. This figure illustrates that the particles spray dried using the dual-orifice plate had a narrow size distribution with a small geometric standard deviation (GSD) of 1.12. It has been reported that spray-dried particles with GSDs ranging from 1.1-1.3 are considered monodisperse particles (Ivey et al. 2018). The correspondence in GSD for the dual-orifice plate proves that it is capable of producing highly monodisperse droplets and spray-dried particles. It can be observed that the particle distribution is slightly asymmetric, which is a known phenomenon likely due to droplet collisions and coalescence (Wang et al. 2019; Ivey et al. 2018). The aerodynamic diameter of the spray-dried particles from doublets was calculated to be around 4.2 µm, which explains the second small peak in the size distribution plot. It is possible to produce some

very fine particles, probably dried from the satellite droplets generated by the monodisperse atomizer. This phenomenon has also been reported before (Ivey et al. 2018). However, in this study any such fine particles were negligible, since the satellite formation was minimized by careful selection of the excitation frequency, and thus they did not appear in the particle size distribution. An SEM image confirming the high uniformity in particle size of one batch of spray-dried leucine particles is shown in Figure 5. When the pressure difference across the orifice is the same, the dual-orifice plate should produce around twice as much liquid throughput as the single-orifice plate due to the same orifice diameter (30 μm) and a similar discharge coefficient (0.7-0.8). In the liquid throughput test where the pressure difference across the orifice was set to a normal operating value (170 ± 10 kPa) for both orifice plates, the dual-orifice plate produced a water throughput of 1.17 g/min, and the single-orifice plate produced a water throughput of 0.58 g/min. These results confirm that the dual-orifice plate had a roughly doubled throughput and, consequently, a doubled powder production rate compared with the single-orifice plate. The powder production rates and collection yields of three further spray drying runs using the dual-orifice plate are shown in Table 3. The actual powder production rates of the three spray drying runs had an average value of 23.8 ± 2.0 mg/hr which was sufficient to produce the required sample mass for SEM and Raman spectroscopy analysis as well as the particle fragility testing within a reasonable spray drying time period. The collection yields of the three spray drying runs were in the range of 75-85%, indicating that there were losses of powders in the spray drying process probably due to wall deposition inside the spray dryer.

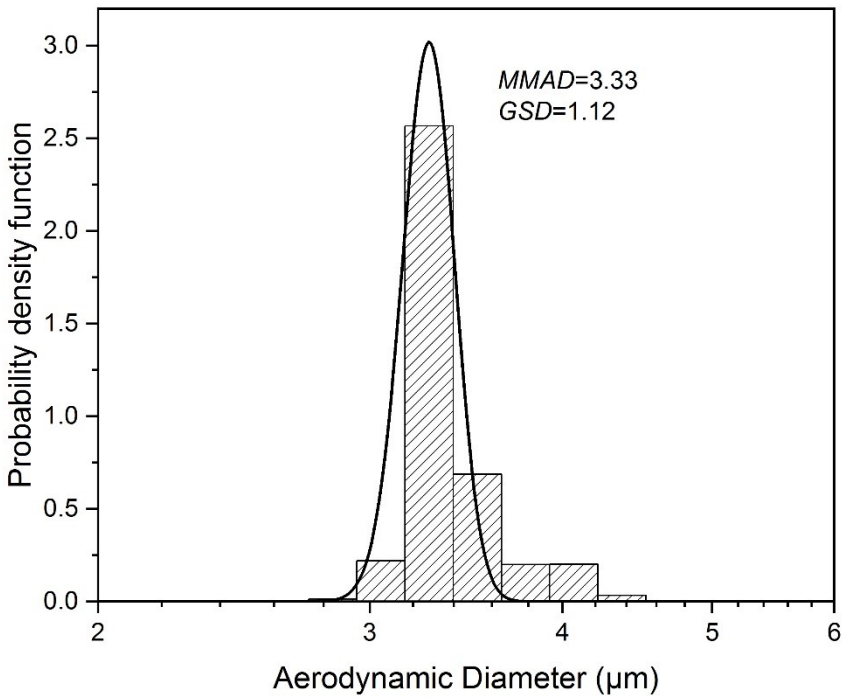

Figure 4 Aerodynamic diameter distribution of leucine particles spray dried from 0.25/0.75 w/w water/ethanol at 20 °C with a mass median aerodynamic diameter (MMAD) of 3.33 μm and geometric standard deviation (GSD) of 1.12

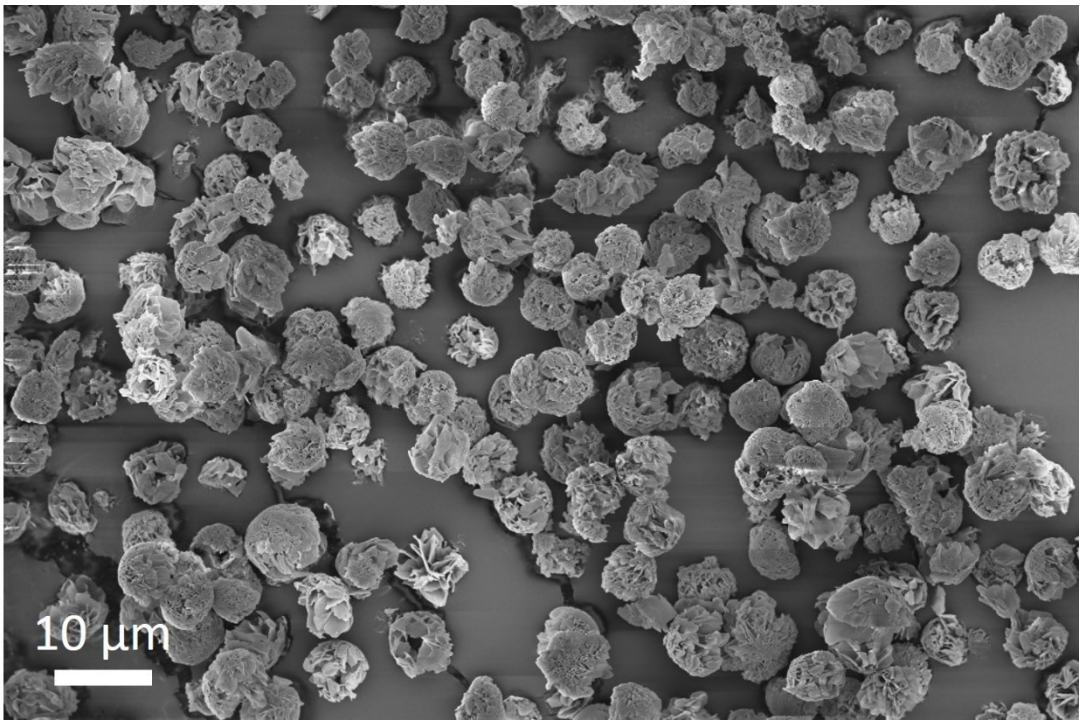

Figure 5 SEM image of leucine particles spray dried from 0.25/0.75 w/w water/ethanol at 20 °C using the dual-orifice plate

Table 3 Powder production rate and collection yield of three spray drying runs using the dual-orifice plate

Formulations	Actual Powder Production Rate (mg/hr)	Theoretical Powder Production Rate (mg/hr)	Collection Yield
L-0.25W/0.75E-20 °C	21.8	25.9	84.2%
L-0.25W/0.75E-40 °C	26.5	31.2	84.9%
L-0.25W/0.75E-80 °C	23.2	29.7	78.1%

L: Leucine; W: Water; E: Ethanol.

2.3.2. Crystallinity of Spray-dried Particles

It has been reported that neat leucine particles spray dried from an aqueous solution are fully crystalline (Feng et al. 2011; Lucas et al. 1999). There has also been evidence showing that leucine particles spray dried from ethanol are likewise crystalline (Najafabadi et al. 2004). To confirm that different water/ethanol ratios and drying temperatures do not change the crystallinity of spray-dried

leucine particles, four samples were selected for Raman spectroscopic analysis, including leucine spray dried from 0.25/0.75 w/w water/ethanol at 20 °C, 0.25/0.75 w/w water/ethanol at 80 °C, 0.5/0.5 w/w water/ethanol at 20 °C and 100% water at 80 °C. Raman spectra of the selected samples are shown in Figure 6 together with reference spectra for crystalline and amorphous leucine. Generally, crystalline and amorphous leucine show significantly different Raman spectra over the presented spectral region; the spectra of crystalline materials have sharper and more-defined peaks, while the corresponding peaks for the spectra of amorphous materials are broadened (Wang et al. 2014). As shown in Figure 6, the Raman spectra of all the measured samples are very similar to the reference spectrum for crystalline leucine. After subtraction of the reference for crystalline leucine, the characteristic peak of amorphous leucine around 750 cm^{-1} was not observed in the residual spectra. The residual spectrum for particles spray dried from 0.25/0.75 w/w water/ethanol at 20 °C is shown in Figure 6 as an example. Amorphous leucine content was not detected, or was below the detection limit of Raman spectroscopy (<1%), in the leucine particles spray dried from various water/ethanol ratios and drying temperatures in this study. Some minor differences can be observed in the spectra of spray-dried leucine compared with the reference spectrum of raw crystalline leucine material. The reference spectrum of raw crystalline leucine is considered as the polymorph I of leucine, which is expected under standard conditions (Feng et al. 2011). Since the transition temperature from polymorph I to polymorph II of leucine is 80 °C (Feng et al. 2011), the spray-dried leucine is very likely to still be in polymorph I. These minor differences might indicate some slight alteration of the unit cell geometry in spray-dried leucine particles compared with the raw crystalline leucine material, as reported before (Feng et al. 2011).

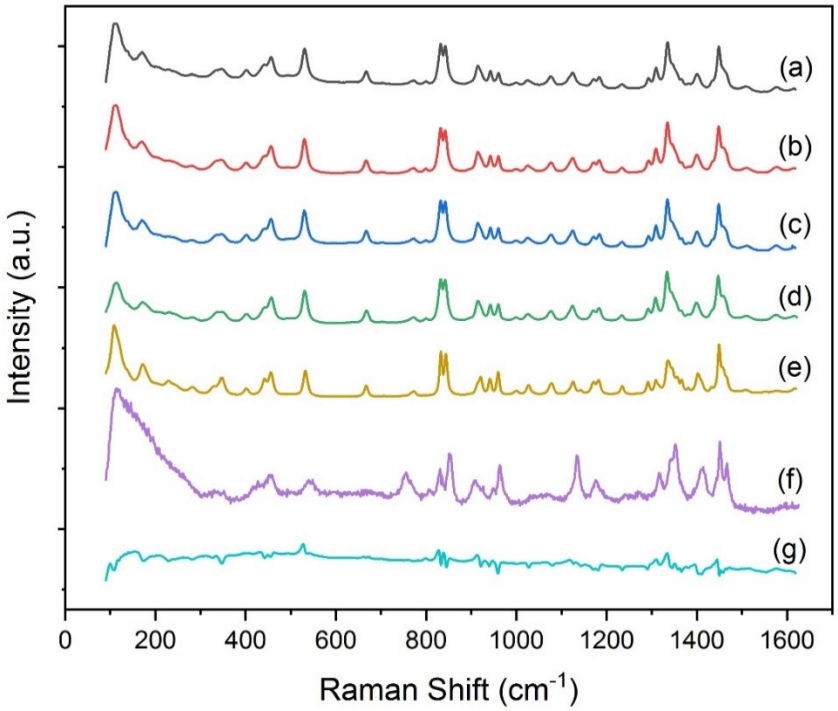

Figure 6 Raman spectra of leucine particles spray dried from (a) 0.25/0.75 w/w water/ethanol at 20 °C, (b) 0.25/0.75 w/w water/ethanol at 80 °C, (c) 0.5/0.5 w/w water/ethanol at 20 °C, (d) 100% water at 80 °C, and spectra for (e) reference crystalline leucine, (f) reference amorphous leucine, and (g) residual spectrum achieved by subtracting reference crystalline leucine from the spectrum of leucine particles spray dried from 0.25/0.75 w/w water/ethanol at 20 °C.

2.3.3. Crystal Size Analysis

SEM images of spray-dried leucine particles are shown in Figure 7. This figure illustrates the different crystal sizes on the surface of leucine particles that were spray dried from different solvent systems and at different drying temperatures. The well-defined domains in the size range of a few hundred nanometers or smaller are very likely individual crystals (Baldelli and Vehring 2016a). These SEM images are presented roughly in order of decreasing crystal size in Figure 7(a-g). As shown in Figure 7(a), leucine particles spray dried from 0.25/0.75 w/w water/ethanol at 20 °C had the largest crystals compared with other cases. These thin flakes were often curved, a feature likely caused by deformation by the electron beam or by templating by the droplet surface. Single crystals

with round contours have also been observed and discussed previously (Baldelli et al. 2016). The next case in Figure 7(b) is leucine spray dried from 0.25/0.75 w/w water/ethanol at 40 °C. The recognizable domains on the particle surface are smaller than in the previous case. The next three cases have similar crystal sizes. As shown in Figure 7(c-e), the domains are still noticeable but much smaller than in the first two cases. The last two cases in Figure 7(f-g) are also similar in that the surface of the particles is very smooth and can be explained by the presence of crystals that are too small to be noticeable. These differences in morphology of crystalline particles are supported by previous literature (Walton 2000), which states that crystalline particles can consist of sub-micron crystals or agglomerates with individual crystals bound together.

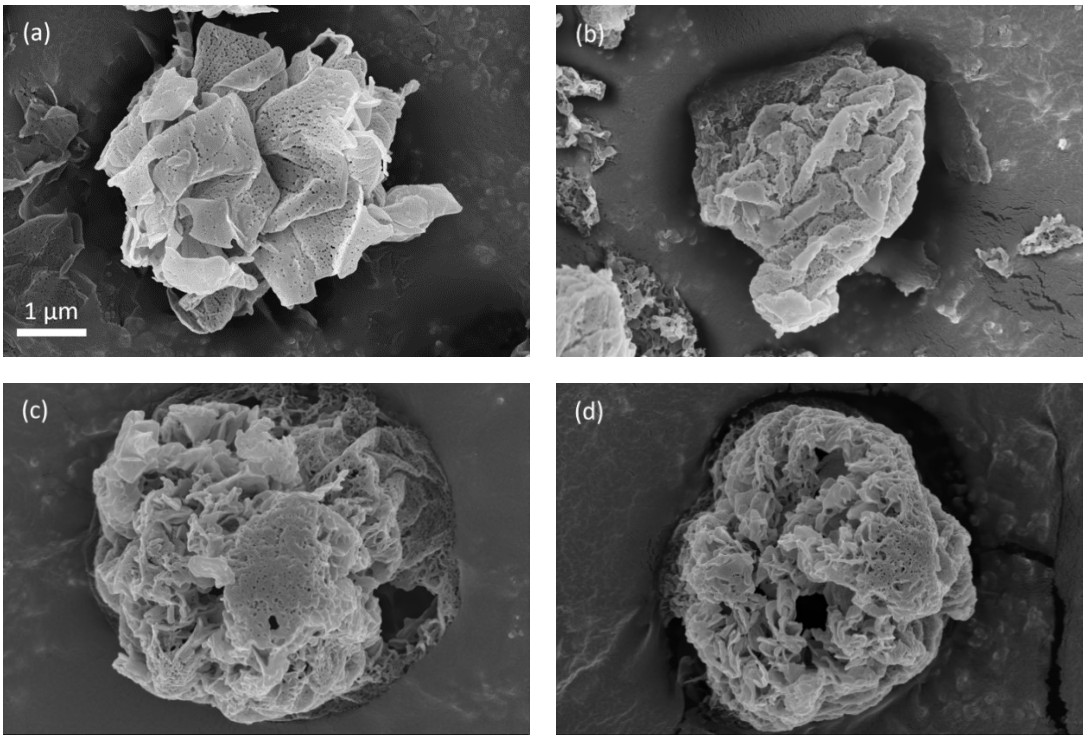

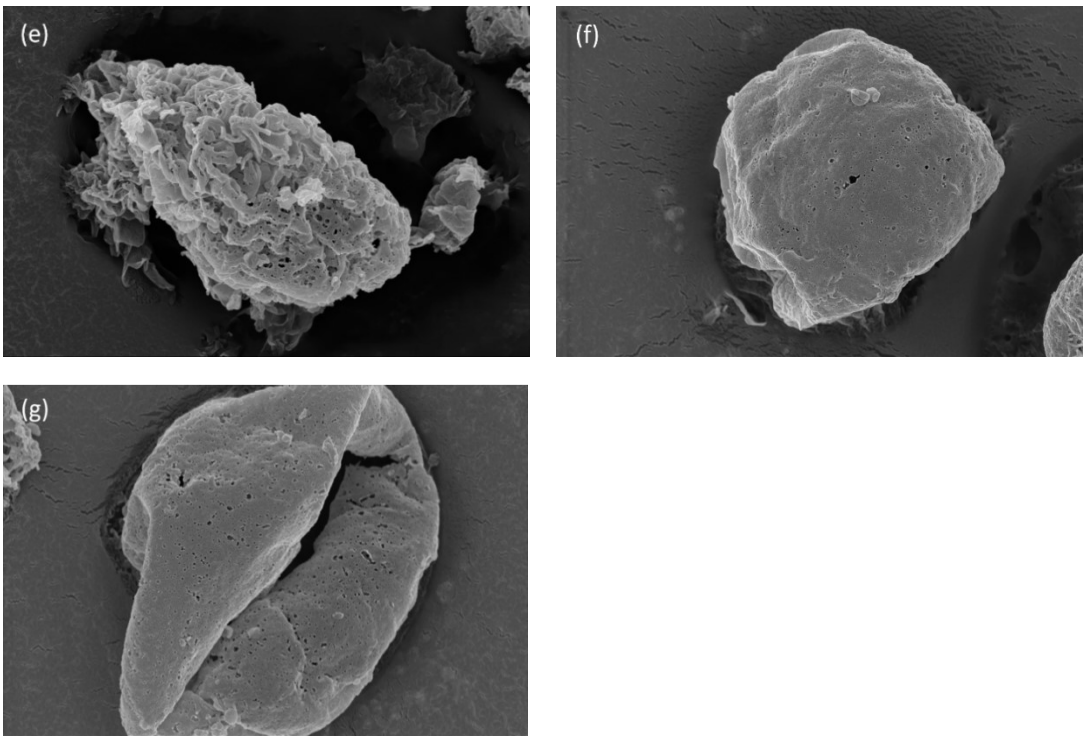

Figure 7 SEM images of leucine particles spray dried from (a) 0.25/0.75 w/w water/ethanol at 20 °C, (b) 0.25/0.75 w/w water/ethanol at 40 °C, (c) 0.25/0.75 w/w water/ethanol at 80 °C, (d) 0.5/0.5 w/w water/ethanol at 20 °C, (e) 0.5/0.5 w/w water/ethanol at 40 °C, (f) 0.5/0.5 w/w water/ethanol at 80 °C and (g) 100% water at 80 °C. The scale bar applies to all the images.

The solvent composition in the evaporating droplet versus drying time is determined using the numerical model and shown in Figure 8. The water/ethanol ratio in the co-solvent system determines the evaporation rate of the droplet and the solubility of the solute. In most cases, the water/ethanol ratio will change with time during spray drying, although it can also remain constant in a special case, i.e. the iso-compositional point (Ordoubadi et al. 2019). The iso-compositional point is similar to the azeotrope during distillation, but the droplet temperature during spray drying is much lower than the boiling temperature of the azeotrope of water and ethanol (Ordoubadi et al. 2019). As shown in Figure 8(a), when the water/ethanol ratio is initially 0.25/0.75, the mass fraction of ethanol generally remains constant throughout most of the spray drying process and decreases only close to the end, regardless of drying temperature. As a result, composition-dependent properties, including evaporation rate and solubility, will remain constant throughout most of the spray drying as well.

This correspondence occurs because the water/ethanol ratio is close to the iso-compositional point, which is 0.23/0.77 w/w water/ethanol (Ordoubadi et al. 2019). When surface saturation of leucine reaches 1, which means nucleation can begin in the co-solvent system, the water/ethanol ratio is still approximately 0.25/0.75. When the surface saturation of leucine reaches the critical supersaturation of 7.9 in 0.25/0.75 w/w water/ethanol, initiating instantaneous nucleation, the water/ethanol ratio increases slightly to around 0.32/0.68 w/w. These instances are indicated by the red arrows in Figure 8(a). It is worth noting that the critical supersaturation of 7.9 is determined based on the 0.25/0.75 w/w water/ethanol solvent composition. The actual water/ethanol ratio at the supersaturation of 7.9 has a small deviation from the assumed water/ethanol ratio, which can influence the calculated supersaturation value. Therefore, iterations on the calculations of the critical supersaturation and the water/ethanol ratio at critical supersaturation can be used to find the accurate critical supersaturation value. However, since the initial deviation of the water/ethanol ratio is relatively small, and for simplicity of calculations, the critical supersaturation value was assumed to be 7.9 for the case of initial water/ethanol ratio of 0.25/0.75 w/w. In comparison, as shown in Figure 8(b), when the water/ethanol ratio is initially 0.5/0.5, the mass fraction of ethanol rapidly decreases to zero. The iso-compositional point requires a relatively high ethanol fraction of ~75% in the solvent to keep the solvent composition constant. When the initial ethanol fraction in the solvent is lower than 75%, the ethanol fraction in the solvent will keep decreasing until no ethanol remains and the solution in the droplet turns into an aqueous solution. In all three cases shown in Figure 8(b), leucine reaches surface saturation after the mass fraction of ethanol decreases to zero, which means the droplet has turned into a leucine aqueous solution before crystallization can commence. Afterwards, when leucine reaches the critical supersaturation of 3.5 in an aqueous solution, the solvent is still water

only, confirming the critical supersaturation of 3.5 in this case. These instances are indicated by the red arrows in Figure 8(b). It is worth noting that the critical supersaturation varies significantly depending on the solvent composition, which needs to be considered in determining the crystallization kinetics.

It is hypothesized that a longer time available for crystallization allows more time for crystal growth in general, thus leading to larger crystal size. In addition, crystal size is also related to the nucleation rate and growth rate. According to a previous study using the standard nucleation and growth models (Seydel et al. 2006), both the nucleation rate and growth rate can be affected by the supersaturation level of the solute; however, the growth rate is much less affected than the nucleation rate, and thus the change in growth rate can be ignored. If the time available for crystallization is relatively short, the supersaturation of the solute will increase rapidly to a high level. Since a higher supersaturation leads to a higher nucleation rate (Handscomb et al. 2009; Seydel et al. 2006), many small crystals are formed quickly while the already established crystals do not have time to grow. By contrast, if the time available for crystallization is relatively long, the supersaturation will increase slowly, giving the already established crystals more time to grow before more nucleation occurs. This theory is also consistent with the hypothesis that a longer time available for crystallization leads to larger crystal size. Two different times available for crystallization—one based on a surface saturation equal to 1 (t_c) and the other based on a surface saturation equal to the previously determined critical supersaturation values of 7.9 for water/ethanol 0.25/0.75 w/w and 3.5 for water/ethanol 0.5/0.5 and 1/0 w/w (t_c^*) —were both numerically modeled and are shown in Table 4, presented in the same order as in Figure 7. As can be seen in Table 4, t_c^* is shorter than t_c for each case, which can be

expected since the critical supersaturation is reached later, while the relative magnitude of each case compared with other cases for t_c^* is actually consistent with t_c. A comparison of Figure 7 and Table 4 shows that leucine particles with larger crystals had relatively larger t_c and t_c^* than the ones with smaller crystals, while those with unnoticeable crystals had the smallest t_c and t_c^*. These results agree well with the theoretical predictions, confirming that both time available for crystallization can be used to qualitatively predict the crystal size of fully crystalline particles. Therefore, in the rest of this paper, either t_c or t_c^* can be used as the time available for crystallization for qualitative analysis. However, using the time available for crystallization to predict other crystallization processes such as polymorph changes was not covered in this study.

It is also important to understand how the process parameters, i.e. water/ethanol ratio and drying temperature, affect the time available for crystallization. Since the solubility of leucine in water/ethanol co-solvent is much lower than in an aqueous solution (Boraey et al. 2013), the saturation occurs much earlier in 0.25/0.75 w/w water/ethanol than in 0.5/0.5 w/w water/ethanol and pure water. Although the water/ethanol co-solvent increases the evaporation rate and shortens the time available for crystallization, the overall effect is that the time available for crystallization is longer in 0.25/0.75 w/w water/ethanol than in 0.5/0.5 w/w water/ethanol and pure water under the same drying temperature. Drying temperature mostly affects the evaporation rate of the droplet. Increasing the drying temperature increases the evaporation rate and simply shortens the time available for crystallization with the same co-solvent ratio.

(a)

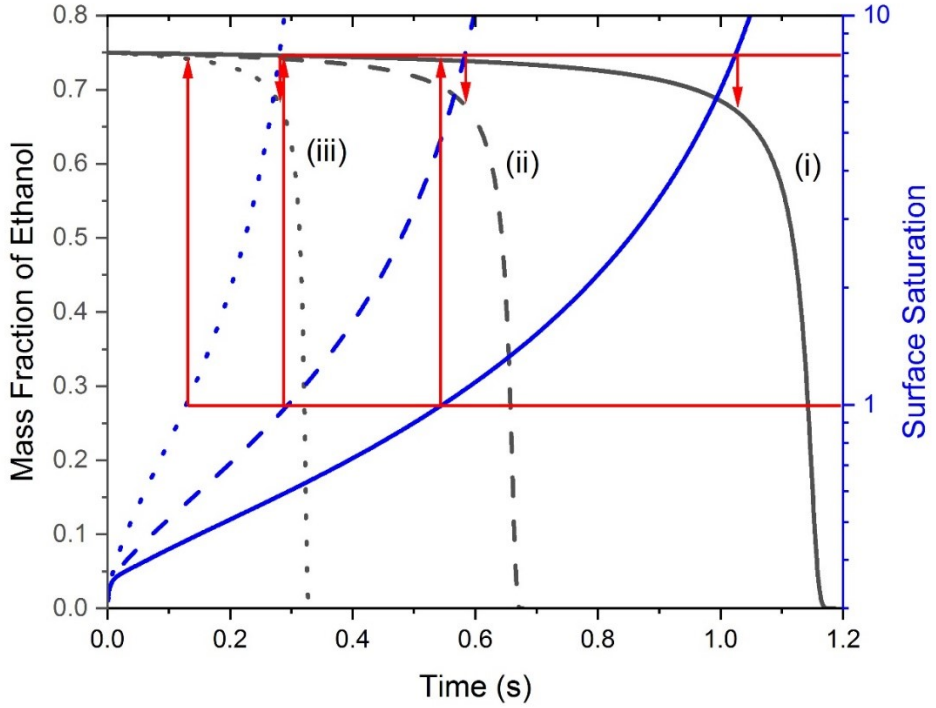
Mass Fraction of Ethanol
Surface Saturation
Time (s)
(i)
(ii)
(iii)
0.0
0.1
0.2
0.3
0.4
0.5
0.6
0.7
0.8
1
10
0.0
0.2
0.4
0.6
0.8
1.0
1.2

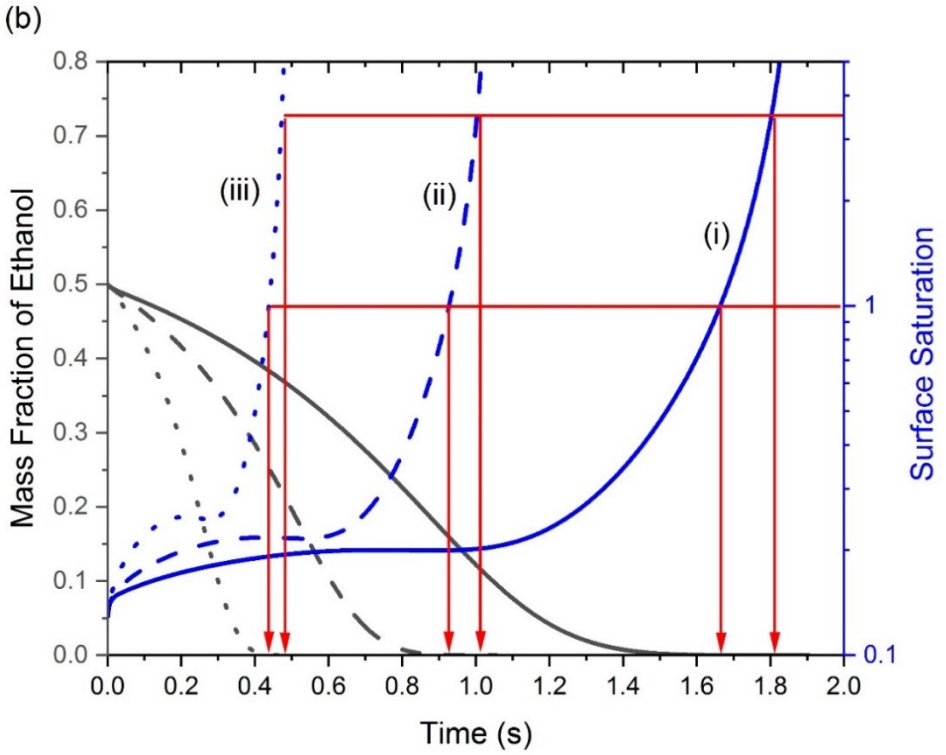

Figure 8 Mass fraction of ethanol and surface saturation of leucine in the evaporating droplet with initial water/ethanol ratio of (a) 0.25/0.75 w/w and (b) 0.5/0.5 w/w at a drying temperature of (i) 20 °C, (ii) 40 °C, and (iii) 80 °C. Red arrows point to the mass fraction of ethanol when surface saturation reaches 1 and the critical supersaturation (7.9 in [a] and 3.5 in [b]).

Table 4 Predicted time available for crystallization for all the cases

water/ethanol w/w	0.25/0.75	0.25/0.75	0.25/0.75	0.5/0.5	0.5/0.5	0.5/0.5	1/0
Drying temperature (°C)	20	40	80	20	40	80	80
Droplet lifetime (s)	1.19	0.68	0.33	1.90	1.06	0.50	0.74
Time to reach saturation (s)	0.55	0.30	0.13	1.66	0.93	0.44	0.68
Time to reach critical supersaturation (s)	1.02	0.58	0.28	1.85	1.03	0.48	0.73
t_c (s)	0.64	0.38	0.20	0.24	0.13	0.06	0.06
t_c^* (s)	0.17	0.10	0.05	0.05	0.03	0.02	0.01

2.3.4. Particle Morphology and Formation

SEM images of three leucine particles spray dried in different conditions are shown in Figure 9 to illustrate three different particle morphologies. Figure 9(a) shows a highly porous leucine particle consisting of very large crystal flakes throughout the particle. Figure 9(b) shows a leucine particle consisting of medium-sized crystals. The particle was broken and the internal structure shows that the particle was still porous with crystals throughout the interior of the particle. Figure 9(c) shows a leucine particle with a hollow structure and a relatively smooth shell.

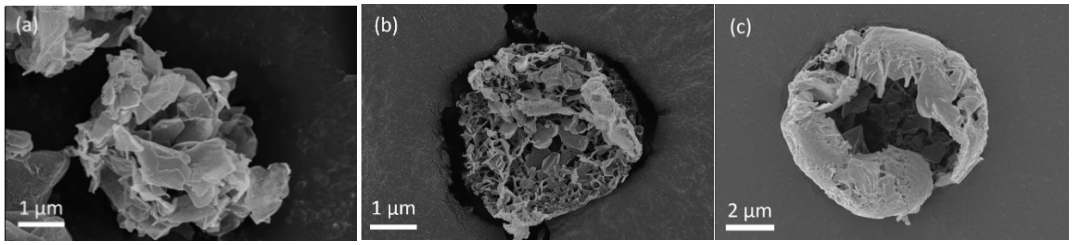

Figure 9 SEM images of leucine particles spray dried from (a) 0.25/0.75 w/w water/ethanol at 20 °C, (b) 0.5/0.5 w/w water/ethanol at 20 °C, and (c) 0.5/0.5 w/w water/ethanol at 80 °C

To understand and explain the morphology of the fully crystalline leucine particles, some particle formation theory should be reviewed. The dimensionless Peclet number, Pe, is very useful in explaining certain particle morphologies and is defined as (Boraey and Vehring 2014)

$$Pe_i = \frac{\kappa}{8D_i} \tag{36}$$

where κ is the evaporation rate and D_i is the diffusion coefficient of component i. This ratio describes how quickly the receding droplet surface shrinks compared to the diffusional motion of the solute inside the droplet. The surface enrichment, which is defined as the ratio of the solute concentration on the surface to the average solute concertation in the droplet for each component, can be approximated by (Vehring 2008; Vehring et al. 2007):

$$E_i = \frac{c_{s,i}}{c_{m,i}} = 1 + \frac{Pe_i}{5} + \frac{{Pe_i}^2}{100} - \frac{{Pe_i}^3}{4000} \tag{37}$$

This approximation assumes the steady state and is accurate within 1% when $Pe < 20$.

When the Peclet number is relatively small (close to 1 or less), the solute concentration is distributed almost evenly, with low surface enrichment. For solutes that do not crystalize, the droplet will likely be dried into a solid particle with a particle density close to the true density of the material. By contrast, when the Peclet number is much larger than 1, the solute concentration is much higher on the droplet surface while the solute concentration is very low inside the droplet, causing a much higher surface enrichment. In this case, a shell may be formed (Vehring 2008; Vehring et al. 2007). The Peclet numbers and surface enrichment calculated using numerical methods are shown in Figure 10. Here some of the Peclet numbers can be seen to change over time due to the changes in water/ethanol ratios, causing corresponding changes in the evaporation rate and diffusion coefficient. Consequently, in some of the cases the surface enrichments do not increase consistently over time, but rather increase first and then decrease, due to the decreases in the Peclet numbers. For all the cases the Peclet numbers are smaller than 3.5, and the surface enrichments are smaller than 1.8. However, it has been shown that leucine spray dried from an aqueous solution forms hollow and low-density particles (Lucas et al. 1999), which cannot be explained by the calculated Peclet numbers and surface enrichment. One plausible explanation is that the Peclet number of the leucine increases drastically at the point of crystallization occurring at the surface at t_c or t_c^*, indicated by circles and squares on Figure 10, respectively. After the crystals are formed, the mobility of the leucine is no longer dependent on the diffusion of leucine molecules but rather on the diffusion of whole leucine crystals. The diffusion coefficient of leucine crystals is orders of magnitude smaller than that of leucine molecules, making the Peclet number much larger. The Peclet numbers of leucine crystals of different diameters (assuming spherical crystals) in pure water and

ethanol at a drying temperature of 20 °C were calculated using numerical methods in conjunction with the Stokes-Einstein equation (Ziaee et al. 2019) and plotted in Figure 11. As shown in the figure, as the leucine nucleates and leucine crystals start to grow, the Peclet number of the leucine crystal increases rapidly to much larger than 1 in both water and ethanol solvent. For water/ethanol co-solvent the Peclet number will lie between these two extreme cases. Therefore, if the leucine crystals are formed at the droplet surface they cannot diffuse to the interior, and if the crystals are formed in the interior they will be swept up by the receding droplet surface, leading to the accumulation of leucine crystals at the droplet surface. When the volume fraction of the crystals at the droplet surface exceeds a certain level, a shell may be formed (Handscomb et al. 2009).

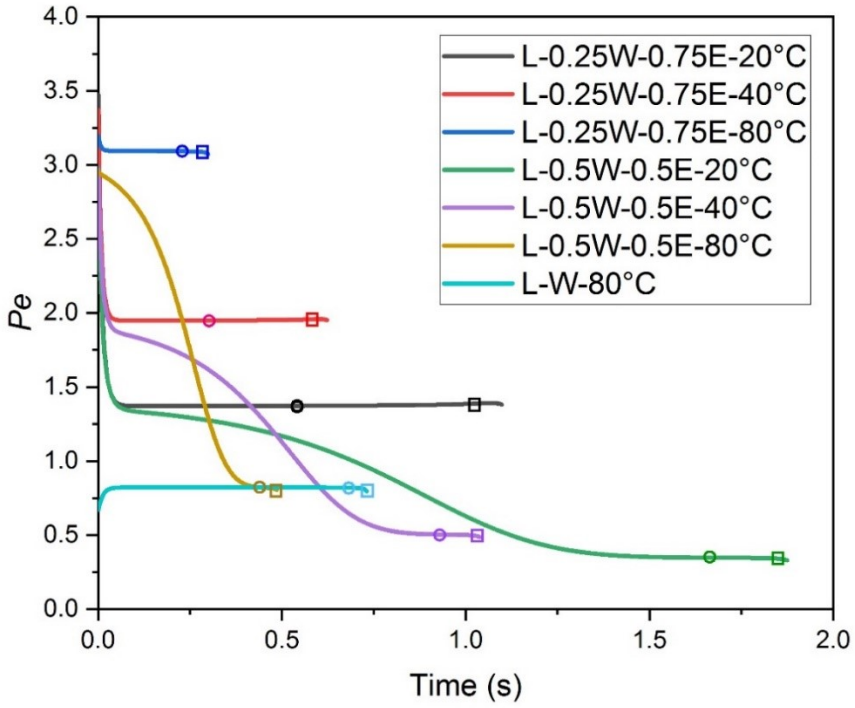

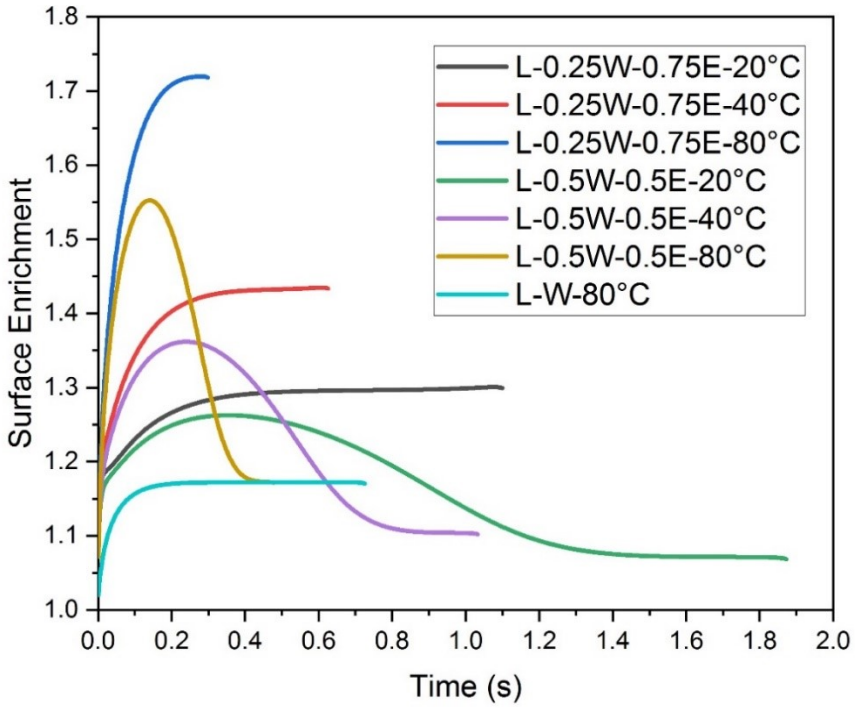

Figure 10 Peclet number (top) and surface enrichment (bottom) as a function of time for all the cases. L: Leucine; W: Water; E: Ethanol. Circles indicate the points at which surface saturation reaches 1, and squares indicate the point at which surface saturation reaches the critical supersaturation.

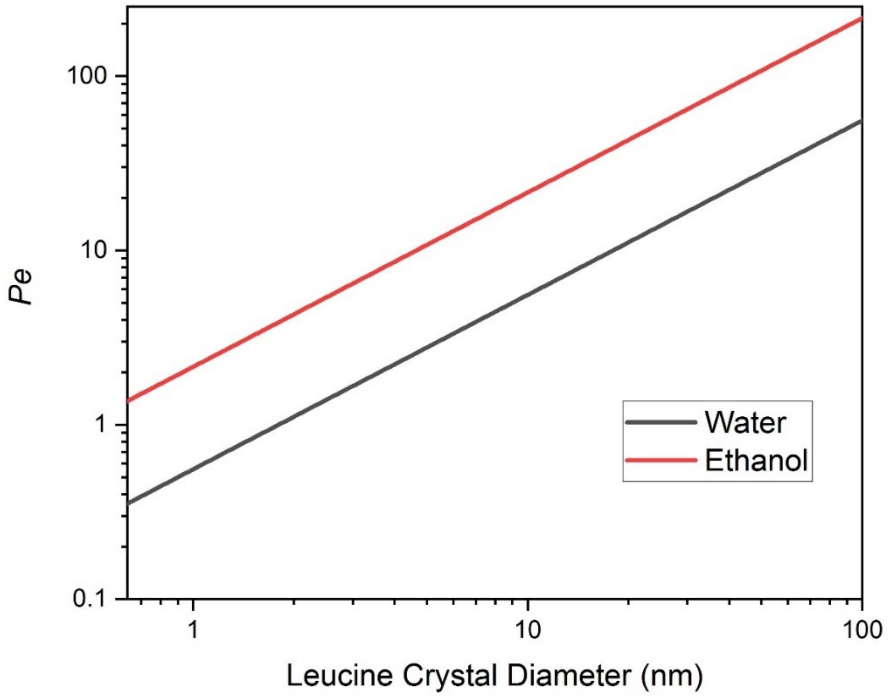

Figure 11 Peclet number of leucine at a drying temperature of 20 °C as a function of crystal diameter in water and ethanol

With the help of particle formation theory as well as the calculated times available for crystallization, the particle morphologies in Figure 9 can now be explained. If the time available for crystallization is relatively long and the supersaturation increases relatively slowly, there will be more than sufficient time for the crystals to grow to larger sizes and to the interior of the particle before more nucleation occurs. Of the three cases, the particle in Figure 9(a) had the longest time available for crystallization, which explains the porous structure with large crystals throughout the interior of the particle. If the time available for crystallization is relatively short and the supersaturation increases relatively quickly, the nanocrystals accumulated at the droplet surface do not have sufficient time to grow larger and to the interior of the particle before the particle is dry. Of the three cases, the particle in Figure 9(c) had the shortest time available for crystallization,

which explains its hollow structure with an empty interior and relatively smooth shell containing much smaller crystals. The particle in Figure 9(b) had a medium time available for crystallization and a medium increasing speed of supersaturation, which explains the medium-sized crystals, as the time available for crystallization in this case was still sufficient for the crystals to grow to the interior of the particle. These three cases are shown schematically in Figure 12.

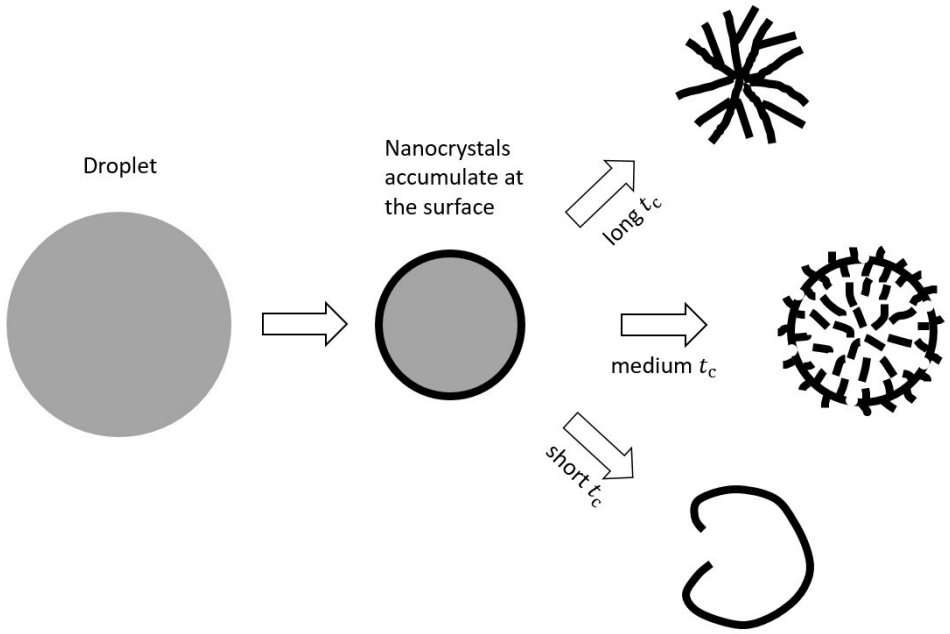

Figure 12 Schematic of the particle formation process for the three cases with different times available for crystallization

2.3.5. Particle Fragility

Crystalline spray-dried particles with different interior structures are likely to have different physical properties, e.g. fragility. SEM images of two batches of leucine particles spray dried in different conditions are shown in Figure 13. Figure 13(a) shows that leucine particles consisting of large

crystals throughout the interior structure were mostly unbroken, while Figure 13(b) shows many broken leucine particles (some of these indicated by red circles) which had a hollow structure with an empty interior and a thin shell consisting of nanocrystals. Leucine particles with a similar hollow structure were also found to be mostly fractured in a previous work (Lucas et al. 1999). These particles were likely broken during collection in the cyclone due to particle-particle or particle-wall collisions (Zhou et al. 2019) since leucine particles with a similar hollow structure collected by a membrane filter have been shown elsewhere to be unbroken (Ordoubadi et al. 2019). One possible explanation is that leucine particles consisting of large crystals bound together in the interior had a strong and stable structure, while leucine particles consisting of nanocrystals in the hollow shell lacked the interior structure, thus increasing their fragility. Keeping the particles unbroken is important in respiratory drug delivery applications because broken particles have reduced particle size and an exposed interior structure that may affect the product performance.

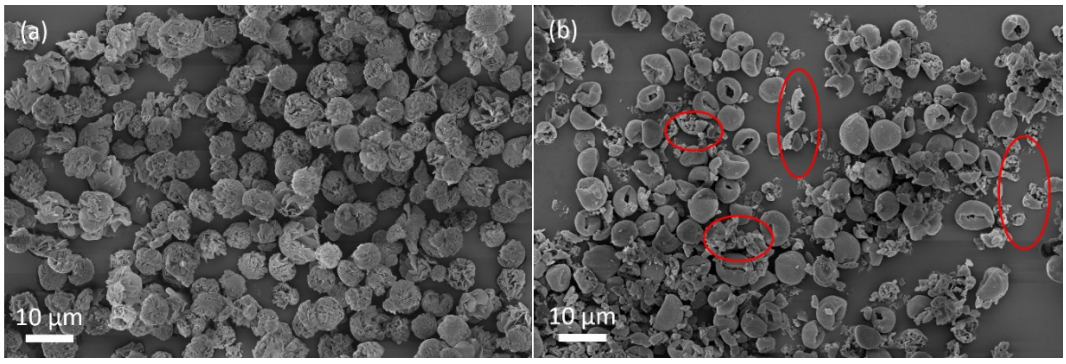

Figure 13 SEM images of spray-dried leucine particles from (a) 0.25/0.75 w/w water/ethanol at 20 °C (b) 100% water at 80 °C. Red circles indicate some of the broken particles.

2.4. Conclusions

Compared with laser drilling, Ga-FIB milling is capable of manufacturing multi-orifice plates with

cleaner orifice edges, regular orifice geometry and smaller orifice sizes while maintaining the monodispersity of spray-dried microparticles. Ga-FIB milling is also compatible with substances like stainless steel that are acceptable for pharmaceutical manufacturing. The powder production rate using the dual-orifice plate manufactured by Ga-FIB milling was sufficient for microscopic and spectroscopic analysis, and also for particle fragility testing. However, plates with more orifices are required for tests requiring larger sample masses, and smaller orifices are required for efficient manufacture of respirable products. Another limitation is that Ga-FIB milling is costly and time-consuming; therefore, more economical and efficient manufacturing techniques for the development of multi-orifice plates should also be considered.

Co-solvent ratio and drying temperature are two important parameters that control the crystallization kinetics in co-solvent spray drying. A higher water/ethanol ratio and higher drying temperature lead to a shorter time available for crystallization and, consequently, a more rapid increase in supersaturation. Increasing the time available for crystallization allows hollow and highly fragile particles consisting of nanocrystals to develop into stronger and more stable porous particles consisting of large crystals throughout the interior. Therefore, the co-solvent ratio and drying temperature must be well controlled in particle design and manufacturing processes to obtain target particle morphology and properties. The numerical methods used in this study are capable of determining the solvent environment as a function of time, which is also beneficial in studying the effects of the solvent environment on other crystallization characteristics including degree of polymorphism, nucleation rate, etc. It is also important to realize for the development of respirable dry powder products that even if particles have the same size, composition, and solid phase, they

can still behave differently depending on the crystal size and interior structure. These findings and methods can be applied to other materials that form fully crystalline particles in spray drying in order to predict particle morphology and properties.

2.5. References

Arpagaus, C., Collenberg, A., Rütti, D., Assadpour, E., and Jafari, S.M. (2018). Nano spray drying for encapsulation of pharmaceuticals. *Int. J. Pharm.,* 546(1–2):194–214.

Azhdarzadeh, M., Shemirani, F.M., Ruzycki, C.A., Baldelli, A., Ivey, J., Barona, D., Church, T., Lewis, D., Olfert, J.S., Finlay, W.H., and Vehring, R. (2016). An atomizer to generate monodisperse droplets from high vapor pressure liquids. *At. Sprays,* 26(2):121–134.

Baldelli, A., Power, R.M., Miles, R.E.H., Reid, J.P., and Vehring, R. (2016). Effect of crystallization kinetics on the properties of spray dried microparticles. *Aerosol Sci. Technol.,* 50(7):693–704.

Baldelli, A. and Vehring, R. (2016). Control of the radial distribution of chemical components in spray-dried crystalline microparticles. *Aerosol Sci. Technol.,* 50(10):1130–1142.

Bayvel, L. and Orzechowski, Z. (1993). Liquid Atomization. Taylor & Francis.

Boraey, M.A., Hoe, S., Sharif, H., Miller, D.P., Lechuga-Ballesteros, D., and Vehring, R. (2013). Improvement of the dispersibility of spray-dried budesonide powders using leucine in an ethanol-water cosolvent system. *Powder Technol.,* 236:171–178.

Boraey, M.A. and Vehring, R. (2014). Diffusion controlled formation of microparticles. *J. Aerosol Sci.,* 67:131–143.

Brenn, G., Durst, F., and Tropea, C. (1996). Monodisperse sprays for various purposes - Their production and characteristics. *Part. Part. Syst. Charact.,* 13(3):179–185.

Brenn, G., Helpiö, T., and Durst, F. (1997). A new apparatus for the production of monodisperse sprays at high flow rates. *Chem. Eng. Sci.,* 52(2):237–244.

Carr, A.G., Mammucari, R., and Foster, N.R. (2011). Particle formation of budesonide from alcohol-modified subcritical water solutions. *Int. J. Pharm.,* 405(1–2):169–180.

Christoffersen, J., Rostrup, E., and Christoffersen, M.R. (1991). Relation between interfacial surface tension of electrolyte crystals in aqueous suspension and their solubility; a simple derivation based on surface nucleation. *J. Cryst. Growth,* 113(3–4):599–605.

Dumouchel, C. (2008). On the experimental investigation on primary atomization of liquid streams. *Exp. Fluids,* 45(3):371–422.

Feng, A.L., Boraey, M.A., Gwin, M.A., Finlay, P.R., Kuehl, P.J., and Vehring, R. (2011). Mechanistic models facilitate efficient development of leucine containing microparticles for pulmonary drug delivery. *Int. J. Pharm.,* 409(1–2):156–163.

Fu, N., Zhou, Z., Jones, T.B., Tan, T.T.Y., Wu, W.D., Lin, S.X., Chen, X.D., and Chan, P.P.Y. (2011). Production of monodisperse epigallocatechin gallate (EGCG) microparticles by spray drying for high antioxidant activity retention. *Int. J. Pharm.,* 413(1–2):155–166.

Gharsallaoui, A., Roudaut, G., Chambin, O., Voilley, A., and Saurel, R. (2007). Applications of spray-drying in microencapsulation of food ingredients: An overview. *Food Res. Int.,*

40(9):1107–1121.

Handscomb, C.S., Kraft, M., and Bayly, A.E. (2009). A new model for the drying of droplets containing suspended solids. *Chem. Eng. Sci.,* 64(4):628–637.

He, G., Bhamidi, V., Tan, R.B.H., Kenis, P.J.A., and Zukoski, C.F. (2006). Determination of critical supersaturation from microdroplet evaporation experiments. *Cryst. Growth Des.,* 6(5):1175–1180.

Ivey, J.W. (2018). Particle Formation from Evaporating Microdroplets for Inhaled Drug Delivery. University of Alberta.

Ivey, J.W., Bhambri, P., Church, T.K., Lewis, D.A., and Vehring, R. (2018). Experimental investigations of particle formation from propellant and solvent droplets using a monodisperse spray dryer. *Aerosol Sci. Technol.,* 52(6):702–716.

Lee, Y.Y., Wu, J.X., Yang, M., Young, P.M., Van Den Berg, F., and Rantanen, J. (2011). Particle size dependence of polymorphism in spray-dried mannitol. *Eur. J. Pharm. Sci.,* 44(1–2):41–48.

Li, L., Sun, S., Parumasivam, T., Denman, J.A., Gengenbach, T., Tang, P., Mao, S., and Chan, H.K. (2016). L-Leucine as an excipient against moisture on in vitro aerosolization performances of highly hygroscopic spray-dried powders. *Eur. J. Pharm. Biopharm.,* 102:132–141.

Liu, W., Chen, X.D., and Selomulya, C. (2015). On the spray drying of uniform functional microparticles. *Particuology,* 22:1–12.

Liu, W., Wu, W.D., Selomulya, C., and Chen, X.D. (2011). Uniform chitosan microparticles prepared by a novel spray-drying technique. *Int. J. Chem. Eng.,* 2011.

Lu, W., Wang, S., Lin, R., Yang, X., and Cheng, Z. (2020). Unveiling the importance of process parameters on droplet shrinkage and crystallization behaviors of easily crystalline material during spray drying. *Dry. Technol.,* 0(0):1–11.

Lucas, P., Kerry, A., Potter, U.J., and Staniforth, J.N. (1999). Enhancement of Small Particle Size Dry Powder Aerosol Formulations using an Ultra Low Density Additive. *Pharm. Res.,* 16:1643–1647.

McDonagh, A.F. and Tajber, L. (2019). The control of paracetamol particle size and surface morphology through crystallisation in a spray dryer. *Adv. Powder Technol.,* 31(1):287–299.

Mehanna, M.M., Mohyeldin, S.M., and Elgindy, N.A. (2014). Respirable nanocarriers as a promising strategy for antitubercular drug delivery. *J. Control. Release,* 187:183–197.

Najafabadi, A.R., Gilani, K., Barghi, M., and Rafiee-Tehrani, M. (2004). The effect of vehicle on physical properties and aerosolisation behaviour of disodium cromoglycate microparticles spray dried alone or with L-leucine. *Int. J. Pharm.,* 285(1–2):97–108.

Ordoubadi, M., Gregson, F.K.A., Melhem, O., Barona, D., Miles, R.E.H., D'Sa, D., Gracin, S., Lechuga-Ballesteros, D., Reid, J.P., Finlay, W.H., and Vehring, R. (2019). Multi-Solvent Microdroplet Evaporation: Modeling and Measurement of Spray-Drying Kinetics with Inhalable Pharmaceutics. *Pharm. Res.,* 36(7).

Ordoubadi, M., Gregson, F.K.A., Wang, H., Nicholas, M., Gracin, S., Lechuga-Ballesteros, D., Reid, J.P., Finlay, W.H., and Vehring, R. (2020). On the particle formation of leucine in spray drying of inhalable microparticles. *Int. J. Pharm.,* (November):120102.

Patel, K.C. and Chen, X.D. (2007). Production of spherical and uniform-sized particles using a laboratory ink-jet spray dryer. *Asia-Pacific J. Chem. Eng.,* 2(5):415–430.

PubChem (n.d.). Leucine. Available at https://pubchem.ncbi.nlm.nih.gov/compound/Leucine (Accessed 1 December 2020).

Rayleigh, Lord (1878). On the Instability of Jets. *Proc. London Math. Soc.,* s1-10(1):4–13.

Rogers, S., Fang, Y., Qi Lin, S.X., Selomulya, C., and Dong Chen, X. (2012a). A monodisperse spray dryer for milk powder: Modelling the formation of insoluble material. *Chem. Eng. Sci.,* 71:75–84.

Rogers, S., Wu, W.D., Lin, S.X.Q., and Chen, X.D. (2012b). Particle shrinkage and morphology of milk powder made with a monodisperse spray dryer. *Biochem. Eng. J.,* 62:92–100.

Schmitz-Schug, I., Kulozik, U., and Foerst, P. (2016). Modeling spray drying of dairy products - Impact of drying kinetics, reaction kinetics and spray drying conditions on lysine loss. *Chem. Eng. Sci.,* 141:315–329.

Seydel, P., Blömer, J., and Bertling, J. (2006). Modeling particle formation at spray drying using population balances. *Dry. Technol.,* 24(2):137–146.

Shishir, M.R.I. and Chen, W. (2017). Trends of spray drying: A critical review on drying of fruit and vegetable juices. *Trends Food Sci. Technol.,* 65:49–67.

Sosnik, A. and Seremeta, K.P. (2015). Advantages and challenges of the spray-drying technology for the production of pure drug particles and drug-loaded polymeric carriers. *Adv. Colloid Interface Sci.,* 223:40–54.

Tontul, I. and Topuz, A. (2017). Spray-drying of fruit and vegetable juices: Effect of drying conditions on the product yield and physical properties. *Trends Food Sci. Technol.,* 63:91–102.

Vehring, R. (2008). Pharmaceutical particle engineering via spray drying. *Pharm. Res.,* 25(5):999–1022.

Vehring, R., Foss, W.R., and Lechuga-Ballesteros, D. (2007). Particle formation in spray drying. *J. Aerosol Sci.,* 38(7):728–746.

Walton, D.E. (2000). The morphology of spray-dried particles a qualitative view. *Dry. Technol.,* 18(9):1943–1986.

Wang, H., Barona, D., Oladepo, S., Williams, L., Hoe, S., Lechuga-Ballesteros, D., and Vehring, R. (2017). Macro-Raman spectroscopy for bulk composition and homogeneity analysis of multi-component pharmaceutical powders. *J. Pharm. Biomed. Anal.,* 141:180–191.

Wang, H., Boraey, M.A., Williams, L., Lechuga-Ballesteros, D., and Vehring, R. (2014). Low-frequency shift dispersive Raman spectroscopy for the analysis of respirable dosage forms. *Int. J. Pharm.,* 469(1):197–205.

Wang, H., Nobes, D.S., and Vehring, R. (2019). Particle Surface Roughness Improves Colloidal Stability of Pressurized Pharmaceutical Suspensions. *Pharm. Res.,* 36(3):1–17.

Wu, W.D., Patel, K.C., Rogers, S., and Chen, X.D. (2007). Monodisperse droplet generators as potential atomizers for spray drying technology. *Dry. Technol.,* 25(12):1907–1916.

Zhou, H., Hu, Z., Zhang, Q., Wang, Q., and Lv, X. (2019). Numerical study on gas-solid flow characteristics of ultra-light particles in a cyclone separator. *Powder Technol.,* 344:784–796.

Ziaee, A., Albadarin, A.B., Padrela, L., Femmer, T., O'Reilly, E., and Walker, G. (2019). Spray drying of pharmaceuticals and biopharmaceuticals: Critical parameters and experimental process optimization approaches. *Eur. J. Pharm. Sci.,* 127(January 2019):300–318.

Chapter 3. Powder Dispersibility of Various Two-Component Particle Systems on Exposure to High Relative Humidity

3.1. Introduction

The nasal route of drug delivery has been used not only for local disease treatment, but also for systemic drug delivery (Illum 2003). Recently, nasal delivery of vaccines, especially those protecting against respiratory infectious disease such as influenza and COVID-19, has attracted increasing research interest. One reason for this interest lies in the potential of nasal vaccines to obtain a local immune response in addition to a systemic immune response, with the combination of the two responses theoretically providing superior protection against respiratory infections (Trows and Scherließ 2016; Illum 2002). A further reason lies in the fact that, compared with parenterally administered vaccines, nasally delivered vaccines are easier and safer to administer (Trows and Scherließ 2016). Dry powder formulations of vaccines for nasal delivery have attracted especial interest recently because unlike the liquid vaccines used for nasal delivery, which typically require low-temperature storage and transport, i.e. a functional cold chain (Wang et al. 2012), dry powder formulations demonstrate increased storage stability without the need for preservatives or extensive cold chain infrastructure (Bartos et al. 2018; Pozzoli et al. 2016; Wang et al. 2012; Garmise et al. 2007; Ishikawa et al. 2002). Hence, dry powder formulations are particularly attractive for global distribution of vaccines (Garmise et al. 2006).

Along with the advantages they carry over their liquid counterparts, dry powder formulations of vaccines for nasal delivery also bring specific requirements to powder development and production.

For example, dry powder formulations for nasal delivery must contain an appropriately large particle size (diameter > 10 μm) to allow sufficient drug deposition in the nasal cavity while minimizing lung deposition (Schroeter et al. 2011, 2015). Moreover, the particle size distribution should be reproducible for consistent product performance (Garmise et al. 2006). The powders should also demonstrate high stability at room temperature for long-term storage and shipping (Wang et al. 2012). Particularly important for nasal delivery is powder dispersibility, which is defined as the ability of powders to disperse into individual particles or flowable agglomerates with external dispersion forces (Vehring 2008), since this property can influence the drug delivery efficiency, i.e. the delivered dose. Factors affecting powder dispersibility have been studied extensively, with particles featuring corrugated surfaces having been found the most dispersible because of their lower density and smaller radius of curvature at the contact zones (Weiler et al. 2010). However, powder dispersibility can decrease sharply due to capillary forces or material bridging when powders are exposed, even briefly, to a high-humidity environment. If unprotected dry powder dosage forms are removed from their packaging in a humid environment but not administered to patients immediately, powder dispersibility may decrease quickly and an incorrect or no dose may be delivered if some or all of the undispersed powder remains in the delivery device. It is therefore desirable to design dry powders to maintain a relatively high dispersibility at least on brief exposure to a high-humidity environment. There are several studies investigating this powder property; however, the powders in these studies are designed for drug delivery to the lung, with a particle size in the range of 1-5 μm (Sibum et al. 2020; Cui et al. 2018; Li et al. 2016, 2017; Zhou et al. 2014). For the large particle size required for nasal delivery, the shell formation kinetics are different (Ordoubadi et al. 2020), so that the results from these studies are not directly applicable here. Strategies to achieve out-of-

package robustness for dry powder dosage forms with large particle size for nasal delivery require further investigation.

Trehalose is a disaccharide often used as an excipient to stabilize biological actives for pharmaceutical applications (Feng et al. 2011). However, sugar excipients like trehalose become very cohesive in atmospheric conditions (Feng et al. 2011), likely requiring additional protection against humidity. Previous studies have shown that powders containing leucine or trileucine demonstrate enhanced dispersibility (Boraey et al. 2013; Lechuga-Ballesteros et al. 2008), and continue to do so when the powders are exposed to moisture (Sibum et al. 2020; Shetty et al. 2018; Li et al. 2016, 2017). Formulations containing pullulan, a linear exopolysaccharide, have been shown to feature corrugated particle surfaces (Carrigy et al. 2019), which are known to improve powder dispersibility (Baldelli and Vehring 2016b). Furthermore, because of the high glass transition temperature of pullulan (Carrigy et al. 2019), formulations containing pullulan are expected to undergo less plasticization and material bridging than unprotected trehalose when exposed to moisture, thus potentially maintaining its dispersibility.

In this study, the dispersibility on exposure to high humidity of three two-component particle systems, trehalose/leucine, trehalose/trileucine, and trehalose/pullulan, was compared to the dispersibility of unprotected trehalose particles. For formulation and process design, particle engineering via spray drying was utilized because it provides the theoretical tools for accelerated design of complex structured microparticles (Vehring 2008). Conventional spray drying produces polydisperse droplets and particles, which complicate calculation of the shell formation process and

can directly influence the powder dispersibility. Polydisperse droplet sizes may lead to variations in particle morphology, including shell thickness, which can also impact powder dispersibility and robustness. To eliminate these complexities, the effect of moisture on powder dispersibility is better studied in a monodisperse model. Monodisperse spray drying uses a vibrating orifice generator instead of a twin-fluid atomizer (Carrigy and Vehring 2019) and has recently been scaled up (Wang et al. 2021) to produce sufficient powder quantities for the dispersibility tests planned in this study.

3.2. Materials and Methods

3.2.1. Materials

Trehalose dihydrate (Cat. No. BP2687-1, Fisher Scientific, NJ, USA), trileucine (Product No. L0879, Sigma-Aldrich Corp., Missouri, USA), pullulan (Product No. J66961, Alfa Aesar, MA, USA), and L-leucine (Cat. No. BP385-100, Acros Organics BVBA, Geel, Belgium) were dissolved in demineralized water to prepare the feed solutions for monodisperse spray drying.

3.2.2. Monodisperse Spray Drying

A monodisperse spray drying setup utilizing a dual-orifice plate (Wang et al. 2021) was used to manufacture model particles for this study. Briefly, monodisperse droplets were generated using a custom vibrating orifice atomizer (Azhdarzadeh et al. 2016), with the liquid feed being pressurized to form jets through the micro-orifice plate. The dual-orifice plate, manufactured by gallium focused ion beam milling, produced two separate liquid jets simultaneously, thus doubling the liquid throughput and, consequently, the powder production rate of a conventional single-orifice plate (Wang et al. 2021). A piezoelectric ceramic ring attached to the head of the atomizer vibrated at a

chosen frequency controlled by a function generator. Controlling the driving frequency and the jet exit velocity via the pressure difference across the orifice achieved disintegration of the liquid jets into monodisperse droplets in the Rayleigh breakup regime (Azhdarzadeh et al. 2016). To minimize droplet collisions, pressurized air was used to disperse the droplets in a turbulent flow from a disperser cap. The monodisperse droplets were then dried in a custom spray dryer (Ivey et al. 2018) into solid particles. Compressed air was selected as the drying gas since no flammable chemicals were used. The spray-dried particles were separated in a stainless-steel cyclone and collected in a glass collection bottle. The inlet and outlet drying gas temperatures were 80 ± 1 °C and 56 ± 1 °C, respectively. The drying gas flow rate was set to 500 standard liters per minute (SLPM) so that particles > 1 μm could be efficiently separated and collected. The outlet relative humidity (RH) was predicted to be ~2%. Based on the predicted outlet RH, the dry basis moisture content of trehalose was predicted to be less than 1% from the moisture sorption isotherms for amorphous trehalose (Hancock and Dalton, 1999). Since all the formulations in this study contain at least 70% trehalose, the moisture contents of all the spray-dried particles were expected to be comparable with that of trehalose which were considered to be minimal. The details of the chosen spray drying parameters are shown in Table 5.

Table 5 Spray drying parameters

Parameter	Value
Pressure difference across orifice	100-200 kPa
Orifice diameter	30 μm

Inlet temperature	80 ± 1 °C
Outlet temperature	56 ± 1 °C
Predicted outlet RH	~2%
Disperser cap orifice diameter	3.0 mm
Dispersing gas pressure	275 kPa
Drying gas flow rate	500 SLPM
Piezoelectric driving frequency	85 ± 5 kHz

3.2.3. Two-Component Particle System Design

For nasal drug delivery, the particle size distribution should be large enough so that only a small fraction of particles have aerodynamic diameters of less than 10 μm, to avoid delivery to the lung (Schroeter et al. 2011, 2015). The particle size resulting from spray drying can be easily designed according to a mass balance consideration. For a two-component particle system, the particle morphology and internal distribution can also be predicted and explained by particle formation theory.

The aerodynamic diameter of spray-dried particles can be expressed as

$$d_{\mathrm{a}} = \left(\frac{\rho_{\mathrm{P}}}{\rho_0}\right)^{\frac{1}{6}} \left(\frac{c_{\mathrm{F}}}{\rho_0}\right)^{\frac{1}{3}} d_{\mathrm{D}} \tag{38}$$

where ρ_{P} is the particle density, ρ_0 is the unit density, c_{F} is the feed solution concentration, and d_{D} is the droplet diameter.

The time necessary to dry the droplets, i.e. the droplet drying time, τ_{D}, can be approximated by

$$\tau_{\mathrm{D}} = \frac{d_0^2}{\kappa} \tag{39}$$

where d_0 is the initial droplet diameter, and κ is the evaporation rate, which depends on the chosen process parameters.

A dimensionless Peclet number, Pe, is very useful in predicting the internal distribution of the formulation components and particle morphology and is defined as

$$Pe_i = \frac{\kappa}{8D_i} \tag{40}$$

where D is the diffusion coefficient, and i represents component i. The Peclet number describes how quickly the droplet evaporates compared with the diffusional motion of the solutes.

For the design of core-shell type particles the surface enrichment of component i, E_i, is a useful parameter. It is defined as the ratio of the surface concentration, $c_{\mathrm{s},i}$, to the average concentration, $c_{\mathrm{m},i}$, and can be approximated by

$$E_i = \frac{c_{\mathrm{s},i}}{c_{\mathrm{m},i}} = 1 + \frac{Pe_i}{5} + \frac{Pe_i^2}{100} - \frac{Pe_i^3}{4000} \tag{41}$$

Equation (41) is accurate within 1% for $Pe < 20$, assuming an asymptotic state (Boraey and Vehring 2014).

For crystallizing components or excipients with low solubility that precipitate via spinodal decomposition (Ordoubadi et al. 2021), the time for a component to reach a critical surface concentration, $\tau_{\mathrm{c},i}$, is another important parameter, expressed as

$$\tau_{\mathrm{c},i} = \tau_{\mathrm{D}}\left(1 - \left(\frac{c_{0,i}}{c_{\mathrm{c},i}} E_i\right)^{\frac{2}{3}}\right) \tag{42}$$

where $c_{0,i}$ and $c_{\mathrm{c},i}$ are the initial concentration and critical concentration of component i. Upon reaching the critical surface concentration, the component starts to crystallize or precipitate via spinodal decomposition. The precipitation window, or the time available for crystallization, is defined as

$$\tau_{\mathrm{p},i} = \tau_{\mathrm{D}} - \tau_{\mathrm{c},i} = \tau_{\mathrm{D}}\left(\frac{c_{0,i}}{c_{\mathrm{c},i}} E_i\right)^{\frac{2}{3}} \tag{43}$$

Using equations (38)-(43), the spray-dried particle size, the internal component distribution during evaporation, and the kinetics of phase separation and shell formation for all excipients in this study can be predicted.

In monodisperse droplet generation, the droplet diameter is approximately twice the orifice diameter (Wu et al. 2007). From a 30 μm-orifice and a 10 mg/mL initial feed solution concentration for all the candidate formulations, the aerodynamic diameter of the spray-dried particle in this study is estimated to be in the range of 10-20 μm, which is at the lower end of particle sizes encountered in nasal delivery. These particles were chosen for the study because they are likely more difficult to protect from the effect of moisture uptake than the bigger particles due to the higher specific surface area. For the spray drying conditions in this study, trehalose has a relatively low Peclet number around 1, leading to an even distribution throughout the droplet, while pullulan has a relatively high Peclet number on the order of 10. Therefore, pullulan has a large surface enrichment and can form a shell covering the trehalose core. Since pullulan has a relatively high glass transition temperature of ~261 °C (Carrigy et al. 2019), the pullulan shell is hypothesized to protect the trehalose core on exposure to high relative humidity, thus enhancing the powder dispersibility. In the trehalose/trileucine system, trehalose and trileucine have similar and relatively low Peclet numbers around 1. However, trileucine has a much lower solubility (7 mg/mL) than trehalose (690 mg/mL) (Wang et al. 2019), which causes the trileucine to reach the critical concentration for phase separation early, enabling the formation of a shell. The high surface activity of trileucine may also aid the process (Vehring 2008). It has been shown that particle systems containing trileucine have low density and corrugated particle surfaces, both of which traits reduce cohesiveness and enhance

aerosol performance (Lechuga-Ballesteros et al. 2008). The trehalose/trileucine system has also shown improved dispersibility on exposure to moisture (Sibum et al. 2020). In the trehalose/leucine system, leucine also has a relatively low Peclet number of around 0.8, as well as a relatively low solubility of 22 mg/mL. If the initial saturation is sufficient, leucine can reach supersaturation early and may crystallize at the droplet surface, leading to the formation of a crystalline shell of leucine (Ordoubadi et al. 2020). It has been shown that leucine not only enhances powder dispersibility, but also protects powders against moisture (Li et al. 2016, 2017).

In this study, the total feed solution concentration for all formulations was 10 mg/mL. Three two-component particle systems at different compositions including trehalose/trileucine (97/3 w/w), trehalose/pullulan (70/30 w/w), and trehalose/leucine (90/10, 80/20, 70/30 w/w) were formulated and their dispersibility characterized as the emitted dose from dry powder inhalers compared with that of trehalose particles. These compositions were chosen because, according to previous studies (Sibum et al. 2020; Carrigy et al. 2019; Li et al. 2017) and the results of particle formation calculations, the protective excipients of these particle systems were likely to provide enough surface coverage around the trehalose core to enhance powder dispersibility. It is worth noting that only 3% trileucine formulated in the trehalose/trileucine system instead of 30% as in other systems was due to the lower solubility of trileucine in aqueous solution.

3.2.4. Aerodynamic Particle Sizer (APS)

For in-process particle monodispersity monitoring and measurement of the particle size distribution, an aerodynamic particle sizer (APS) (Model: 332100, TSI, Shoreview, USA) was used to

isokinetically sample particles and repeatedly measure size distribution for 20 s every 15 minutes during the entire spray drying process, which typically lasts 3-4 hours. The driving frequency to the microjet atomizer needs to be adjusted to restore monodispersity in case the in-line measured particle size distribution shifts towards polydispersity and the geometric standard deviation exceeds 1.2.

3.2.5. Preconditioning of Powder Samples

The sample powders were filled into size 3 hydroxypropyl methylcellulose capsules (Quali-V®-I, Qualicaps, Inc., Madrid, Spain) in a dry environment (<2% RH) that was verified using a hygrometer (MI70 Measurement Indicator with HMP77B humidity and temperature probe, Vaisala, Vantaa, Finland). The powder mass filled into each capsule ranged from 20 to 40 mg. The filled capsules were then closed and kept in a dry environment or in a humid environment for 10, 20, 30, and 60 min before being pierced and actuated from a dry powder inhaler. For the humid environment group, the filled capsules were placed in open petri dishes inside an environmental chamber (Photostability Test Chamber Model No. CEO910W-4, Thermal Product Solutions, PA, USA) set to 90% RH and 25 °C.

3.2.6. Emitted Dose Measurements

Dispersibility of the preconditioned powder samples was characterized using the emitted dose from a dry powder inhaler (Seebri® Breezhaler®, Novartis International AG, Basel, Switzerland). The dry powder inhaler was connected to an Alberta Idealized Throat with a custom 3D-printed mouthpiece adapter for actuation and flow rate control. The actuation flow rate was controlled by a critical flow

controller (Critical Flow Controller Model TPK 2000, Copley Scientific Limited, Nottingham, UK) for a constant flow rate of 60 or 15 L/min for 2.4 s. The capsules were pierced manually in the dry powder inhaler to prepare for actuation. Emitted dose from the device, defined as the percentage of powder mass emitted from the total filled powder in the capsule, was assessed. The filled powder mass was determined by gravimetrically weighing the empty and filled capsule, and the emitted powder mass was determined by gravimetrically weighing the dry powder inhaler with the capsule installed before and after actuation. The emitted dose for each case was measured in duplicate.

3.2.7. Scanning Electron Microscopy (SEM)

The spray-dried particles stored in a dry box and those exposed to 90% RH and 25° C for 30 and 60 min were analyzed for particle morphology using field emission scanning electron microscopy (Zeiss Sigma FESEM, Zeiss, Jena, Germany). The particle samples were gold-coated for 120 s using a sputter coater (Desk II Gold Sputter, Denton Vacuum, NJ, USA) and then imaged using the in-lens detector set to 3-5 kV accelerating voltage at a working distance of 4-7 mm. The particles exposed to the humid environment were analyzed immediately after exposure.

3.2.8. Raman Spectroscopy

The sample spray-dried particles stored in a dry box and the particles exposed to 90% RH and 25 °C for 30 and 60 min were qualitatively analyzed for solid phase using a custom Raman spectroscopy instrument (Wang et al. 2017). Before the capsules were opened and the particles analyzed, they were taken out of the environmental chamber and kept at room conditions (21 ± 1 °C and 30-50% RH) for less than 20 min. A 671 nm diode-pumped laser (Ventus 671, Laser

Quantum, UK) was used for the Raman system, which had a maximum power of 500 mW. The sample materials were placed on the sample holder in a cavity with a volume of 0.2 µL. The sample materials were analyzed at room temperature (21 ± 1 °C) and under dry conditions (< 3% RH) in a nitrogen atmosphere. Raw materials of trehalose, leucine, and trileucine were measured directly as the crystalline references, and raw material of pullulan was measured directly as the amorphous reference. Spray-dried trehalose was measured as the amorphous reference, as described elsewhere (Wang et al. 2019). The amorphous leucine reference was achieved by subtracting the spectrum of water from the spectrum of saturated aqueous leucine solution (Feng et al. 2011).

3.2.9. Statistical Analysis

The emitted dose measurements were reported as mean ± standard deviation and were analyzed statistically by a two-tailed student's t-test. Statistically insignificant differences were indicated for p-value larger than 0.05.

3.3. Results and Discussion

3.3.1. Particle Size

The mass median aerodynamic diameter (MMAD) and geometric standard deviation (GSD) for all spray-dried formulations are shown in Table 6. The MMADs were in the range of 13-17 µm as designed. It is generally believed that the GSD of monodisperse spray-dried particles should be less than 1.3 (Ivey et al. 2018). The GSDs for all formulations prepared in this study were in the range

of 1.09-1.14, demonstrating high uniformity in the size of the spray-dried particles produced by the dual-orifice atomizer.

Table 6 MMAD and GSD for all spray-dried formulations

Formulation	MMAD (μm)	GSD
Tre	16.1	1.09
Tre97Tri3	13.3	1.12
Tre70Pu30	14.2	1.14
Tre70Leu30	15.1	1.11
Tre80Leu20	16.3	1.09
Tre90Leu10	15.3	1.11

MMAD: mass median aerodynamic diameter
GSD: geometric standard deviation

3.3.2. Crystallinity

The Raman spectroscopy analysis results for the spray-dried trehalose/pullulan 70/30 and trehalose/trileucine 97/3 formulations are shown in Figure 14. As reported elsewhere (Wang et al. 2019), trehalose does not crystallize in typical spray drying conditions. To verify the solid phases of pullulan and trileucine, the amorphous trehalose reference was subtracted from the spectra of spray-dried formulations. After the subtraction process, the residual spectrum of trehalose/pullulan 70/30 was found to be very similar to the amorphous pullulan reference, and the residual spectrum of trehalose/trileucine 97/3 showed no evidence of crystalline trileucine since no characteristic fingerprint peaks could be detected. Therefore, as expected, pullulan and trileucine were confirmed

to be amorphous, forming amorphous shells covering the trehalose core.

The Raman spectroscopy analysis results for spray-dried trehalose/leucine 90/10, 80/20 and 70/30 are shown in Figure 15. After the amorphous trehalose reference has been subtracted, the three residual spectra are all similar to the crystalline leucine reference with a lattice mode at ~180 cm^{-1} and without any evidence of amorphous leucine, confirming that leucine was crystalline in all three spray-dried trehalose/leucine formulations. It is worth noting that as little as 10% leucine in the formulation leads to fully crystalline leucine in these spray-dried particles. A previous study (Feng et al. 2011) showed that a minimum of 25% leucine was necessary to achieve fully crystalline leucine in the spray-dried trehalose/leucine particles under the conditions of this study. This deviation may stem from the different particle sizes and, consequently, the different times available for crystallization. Instead of using equation (43), the time available for crystallization of leucine in the trehalose/leucine system was determined more precisely as the window from the time for leucine to reach the critical concentration to the time for trehalose to reach the critical concentration, i.e. $t_{\mathrm{c,tre}} - t_{\mathrm{c,leu}}$ (Ordoubadi et al. 2020). The critical concentration of leucine, which is reached at a supersaturation of 3.5 (Ordoubadi et al. 2020), is 77 mg/mL, and the critical concentration of trehalose is 830 mg/mL (Ordoubadi et al. 2020). Under the chosen conditions in this study, the Peclet number of leucine and trehalose was around 0.8 and 1 respectively, and the droplet evaporation rate was approximately 4.9 $\mu m^2/ms$. With these values inserted into equation (38)-(42), the time available for crystallization can then be determined. In Feng et al.'s study the spray-dried particles containing 10% leucine, of which the crystallinity was 53%, had a MMAD of 2.0 μm and time available for crystallization of 0.1 ms, while in this study the spray-dried particles with the same leucine fraction, yet completely crystalline, had a MMAD of 15.3 μm and a time available for

crystallization of 4.1 ms. Longer time available for crystallization gives more time for the solute to crystallize, thus leading to a higher degree of crystallinity.

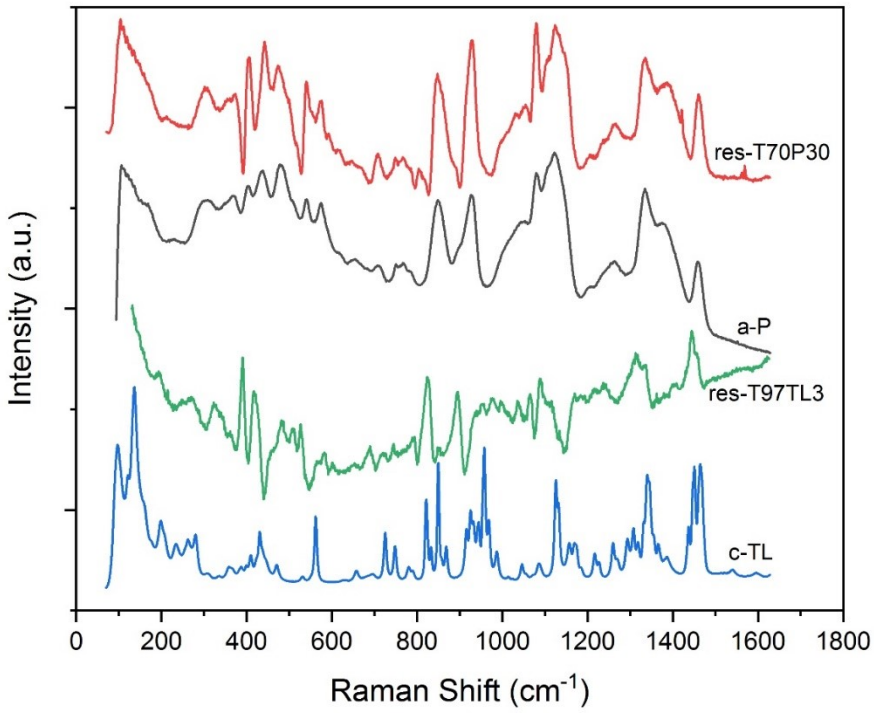

Figure 14 Raman spectroscopy analysis of spray-dried trehalose/pullulan and trehalose/trileucine particles. Legend: "res-T70P30" is the residual spectrum after the amorphous trehalose reference has been subtracted from the spray-dried trehalose/pullulan 70/30, "a-P" is the raw amorphous pullulan reference, "res-T97TL3" is the residual spectrum after the amorphous trehalose reference has been subtracted from the spray-dried trehalose/trileucine 97/3, and "c-TL" is the raw crystalline trileucine reference.

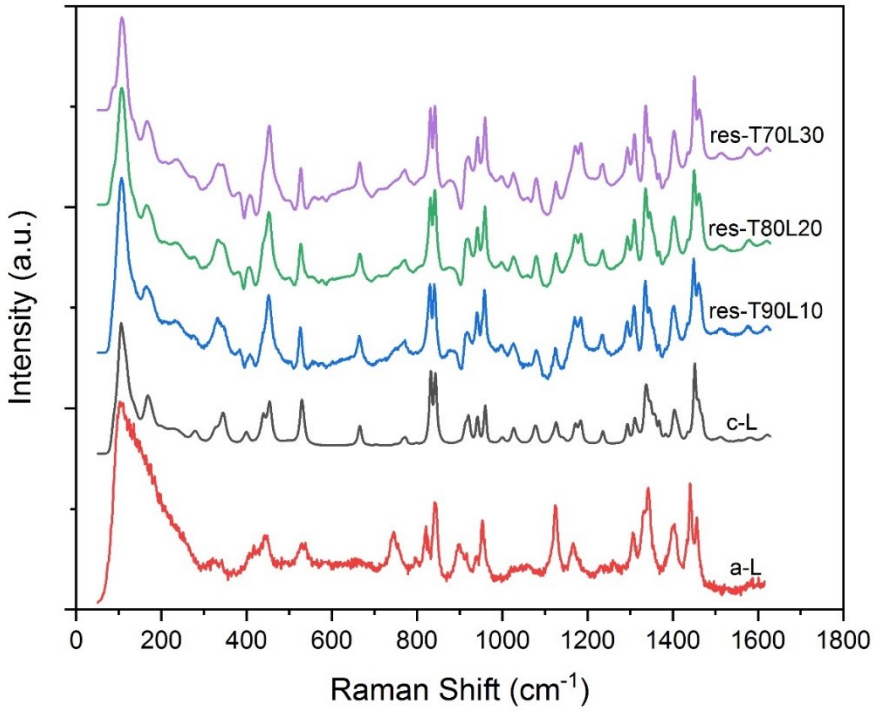

Figure 15 Raman spectroscopy analysis of spray-dried trehalose/leucine particles. Legend: The spectra labeled "res-" are the residual spectra after the amorphous trehalose reference has been subtracted from the three different spray-dried trehalose/leucine formulations, "c-L" is the raw crystalline leucine reference, and "a-L" is the amorphous leucine reference.

3.3.3. Particle Morphology

The SEM images of spray-dried particles for all the formulations are shown in Figure 16. In all cases, the particles showed uniform particle size, confirming the results from the APS measurements. Some particles of a slightly larger size can be observed in the images. These particles were dried from doublets or triplets due to droplet coalescence, which is a known phenomenon reported previously in monodisperse spray drying using a microjet atomizer (Wang et al. 2019; Ivey et al. 2018). The trehalose particles generally had spherical shapes with small dimples on the particle surface, a trait that has also been observed in previous studies (Carrigy et al. 2019; Ordoubadi et al.

2019; Wang et al. 2019). Spray-dried particles of trehalose/trileucine 97/3 and trehalose/pullulan 70/30 had highly corrugated particle surfaces, which are caused by the early formation and subsequent collapse of amorphous trileucine and pullulan shells when they still lack mechanical strength. Spray-dried particles of trehalose/leucine 70/30, 80/20, and 90/10 were generally spherical without much corrugation. Some well-defined domains, which are likely individual leucine crystals, can be observed on the particle surfaces. An interesting particle morphology can be found on some particles of trehalose/leucine 80/20, which had multiple protrusions on the particle surface. These are possibly larger individual crystals, and only some particles in this batch exhibited this morphology, which points to the randomness of the onset of nucleation in the particle formation process.

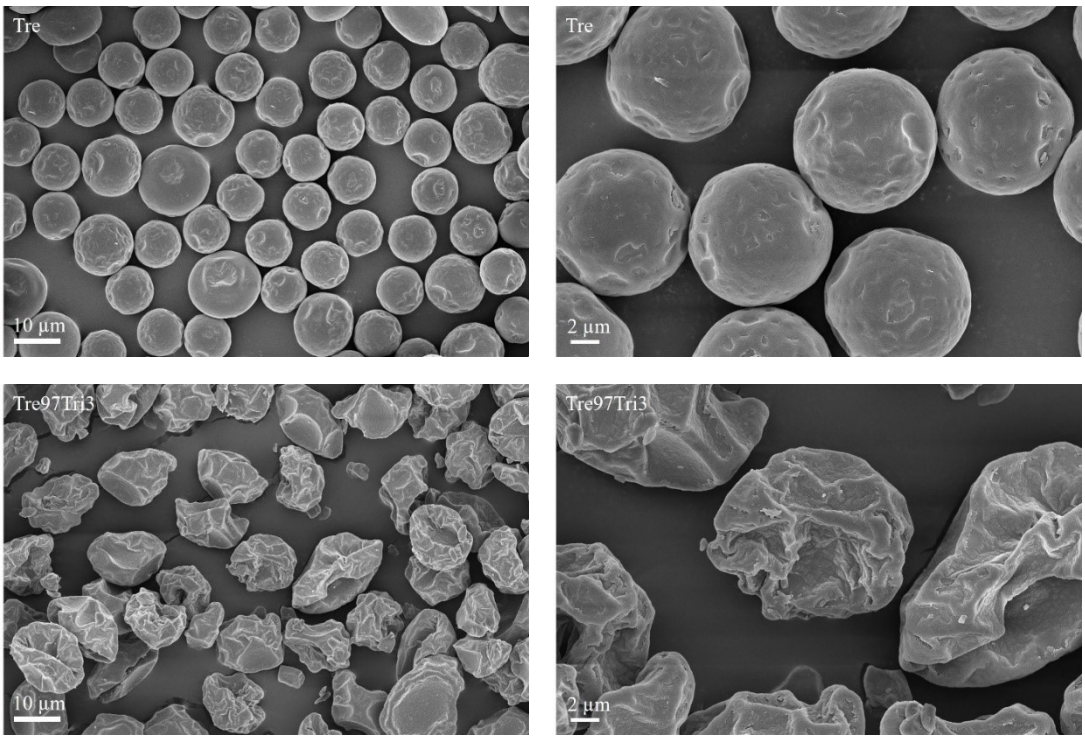

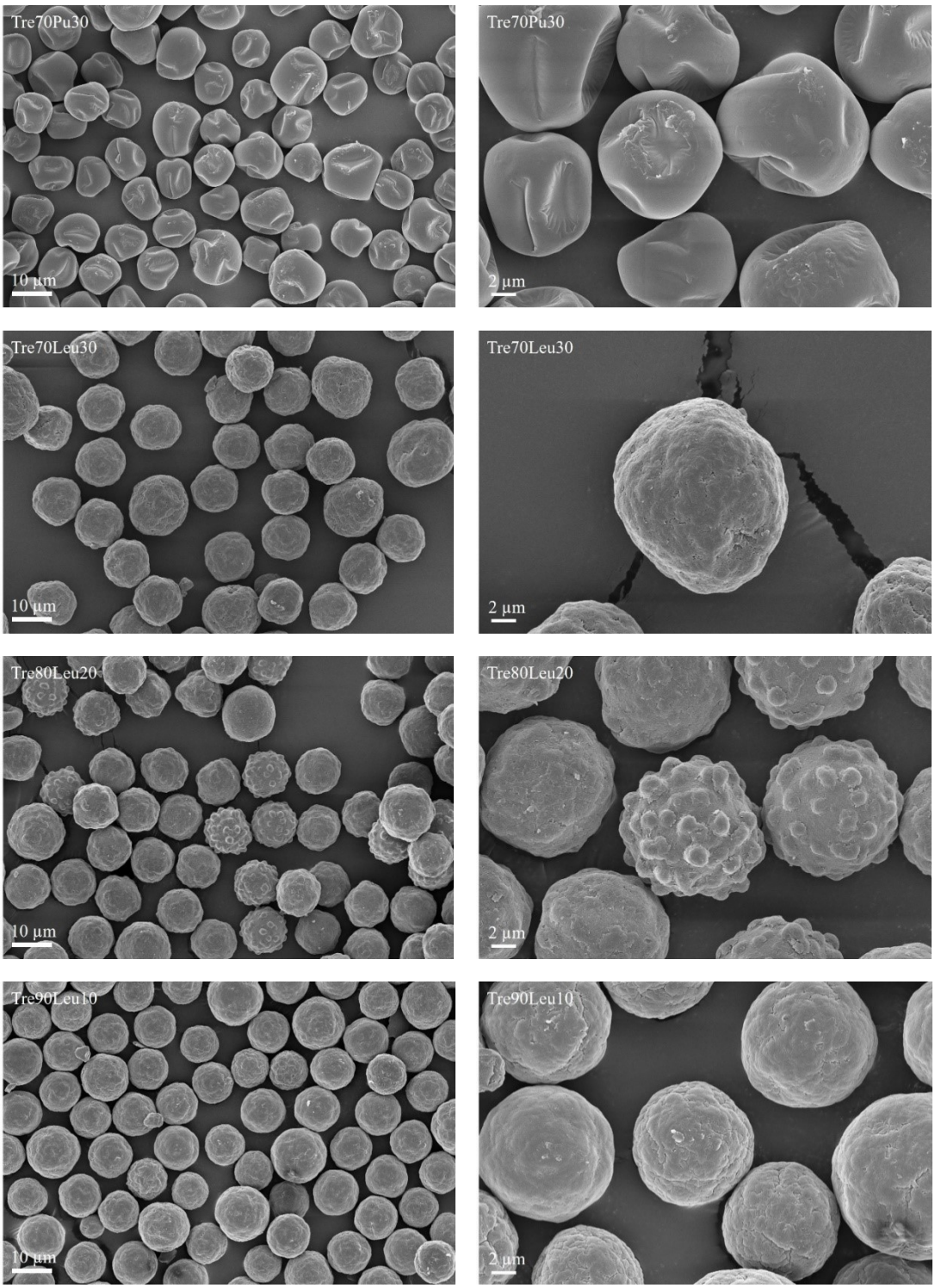

Figure 16 SEM images of all spray-dried formulations: trehalose, trehalose/trileucine 97/3, trehalose/pullulan 70/30, and trehalose/leucine 70/30, 80/20, and 90/10.

3.3.4. Powder Dispersibility

The emitted dose measurements for trehalose, trehalose/pullulan 70/30, trehalose/leucine 70/30, and

trehalose/trileucine 97/3 are shown in Figure 17. The DPI actuation flow rate was set to 60 L/min, and the capsules filled with the spray-dried powders were exposed to 90% RH and 25 °C for 0 min, 30 min, and 60 min before being measured. From Figure 17, we can see that at a 60 L/min flow rate all the formulations had relatively high emitted doses (>90%) prior to humidity exposure with statistically insignificant differences, which is not surprising due to the large particle size of the powders. After 30 min exposure to 90% RH and 25 °C, the emitted dose of trehalose decreased to 68.9 ± 6.9%, while all three two-component systems maintained high emitted doses (>90%) with statistically insignificant differences. This shows that after 30 min exposure to a relatively high-humidity environment the three two-component systems were all able to maintain powder dispersibility, as measured by emitted dose, compared with pure trehalose particles. After 60 min exposure to 90% RH and 25 °C, hardly any trehalose particles were emitted from the device. The emitted dose for the Trehalose/pullulan 70/30 was also significantly reduced, to 7.5 ± 0.2%, a result likely due to the plasticization of the amorphous pullulan shell. Since pullulan has a higher glass transition temperature than trehalose (Carrigy et al. 2019), the pullulan shell may maintain dispersibility for the shorter period of time, but in the extreme case of an hour's exposure to high humidity the pullulan shell may still undergo sufficient plasticization to increase cohesion in the powder. Trehalose/trileucine 97/3 showed a greater decrease in the emitted dose, to 42.8 ± 23%. The addition of trileucine to the dry powder formulation led to corrugated particle surfaces, which may provide more protection than the fairly smooth pullulan surfaces. However, because of the relatively low concentration of trileucine in the formulation, the trileucine shell might be relatively thin and likely to plasticize due to its amorphous nature, thus explaining the limited protection it offers against humidity.

The emitted dose of trehalose/leucine 70/30 after 60 min exposure to humidity showed only a slight decrease to 90.3 ± 10%. The hydrophobic, crystalline leucine shell is able to reduce cohesive forces, thus enhancing the powder's dispersibility (Boraey et al. 2013). In addition, the crystalline leucine shell has very low water uptake and no plasticization, which reduces the interactions between particle surface and moisture, thus providing protection against moisture (Li et al. 2016). This improvement in powder dispersibility was shown to remain quite effective for a very long exposure to humidity, demonstrating that the trehalose/leucine 70/30 particle system had the best powder dispersion performance against moisture of the three two-component particle systems. Therefore, the trehalose/leucine system was selected as the optimal formulation system to maintain powder dispersibility on exposure to high humidity for further investigations into the effectiveness of lower mass fractions of leucine, which will be discussed later.

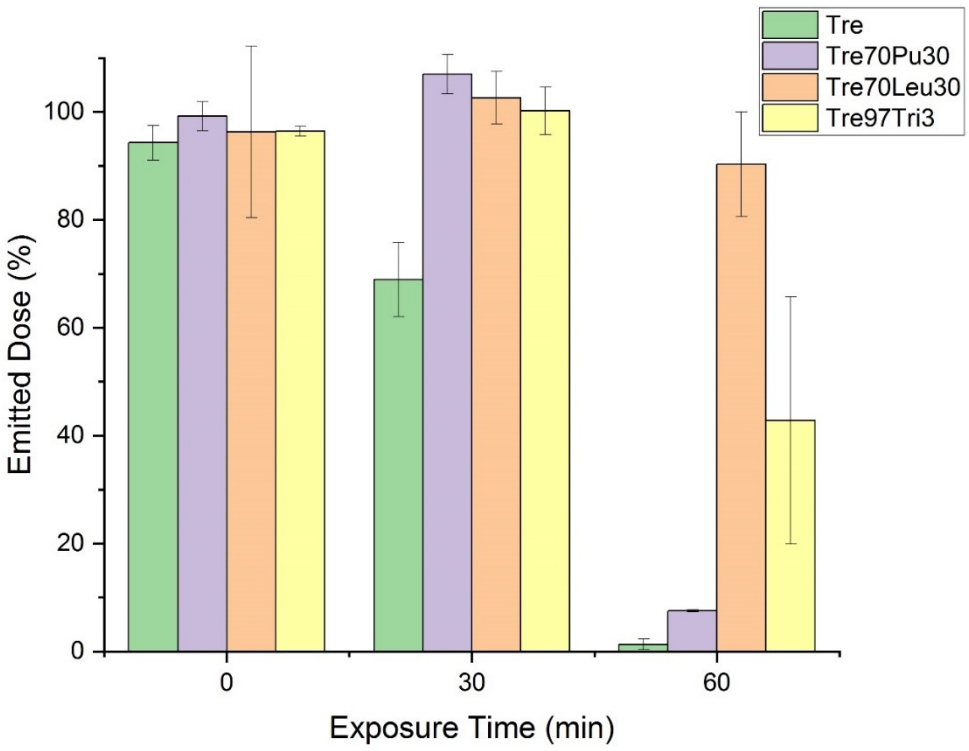

Figure 17 Emitted dose measurements at 60 L/min actuation flow rate for trehalose, trehalose/pullulan 70/30, trehalose/leucine 70/30, and trehalose/trileucine 97/3. These dry powder formulations were exposed to 90% RH and

25 °C for 0 min, 30 min, and 60 min. The error bars represent the percentage difference between the measurements.

The emitted doses of trehalose/leucine 90/10, 80/20, 70/30, as well as those of the pure trehalose particles, are shown in Figure 18. The actuation flow rate was reduced to 15 L/min to provide a more difficult scenario, and the humidity exposure time was set to 0, 10, 20, 30, and 60 min. From Figure 18, we can see that at the 15 L/min flow rate neat trehalose powder indeed shows a reduced emitted dose of 65.6 ± 8.4% as compared to the > 90% at 60 L/min. Yet, all trehalose/leucine formulations had higher emitted doses than neat trehalose even without exposure to humidity, showing that the addition of as little as 10% leucine in the dry powder formulation enhanced the powder dispersibility. Among the three trehalose/leucine formulations, surprisingly, trehalose/leucine 80/20 had the highest emitted dose (102.5 ± 5.5%). This may be due to the observed surface morphology of some trehalose/leucine 80/20 particles, whose many protrusions on the particle surface may greatly increase the corrugation of the particle surface and enhance the powder dispersibility.

After 10 min exposure to 90% RH and 25 °C the emitted dose of trehalose decreased from 65.6 ± 8.4% to 42.8 ± 23%, while the emitted doses of the three trehalose/leucine formulations were preserved. These results show that the powder dispersibility of trehalose particles is affected rather quickly, after only 10 min exposure to humidity under these conditions, while the coverage of a crystalline leucine shell provides very effective protection. After 20 min exposure to humidity, the emitted dose of trehalose decreased further to 15.4 ± 6.4%, while the emitted doses of trehalose 70/30 and 80/20 remained unchanged. Trehalose/leucine 90/10 showed a slight decrease in the emitted dose, to 71.0 ± 0.7%, which may be due to the thinner leucine shell. After 30 min exposure to humidity, all the trehalose/leucine formulations showed moderate decreases in the emitted doses.

However, even trehalose/leucine 90/10, with the lowest emitted dose among the three trehalose/leucine formulations, still had a much higher emitted dose (42.7 ± 5.7%) than trehalose (10.0 ± 3.3%), showing the improvement relative to pure trehalose particles. After 60 min exposure to humidity, trehalose/leucine 90/10 was no longer able to provide protection and maintain the powder dispersibility. Trehalose/leucine 80/20 and 70/30 showed decreases in the emitted doses to 36.5 ± 16.2% and 23.5 ± 3.3% respectively, indicating that these formulations were still able to provide some protection after 60 min exposure. It is worth noting that in all cases trehalose/leucine 80/20 had a comparable emitted dose to that of trehalose/leucine 70/30 with statistically insignificant differences, despite its lower leucine mass fraction. Although trehalose/leucine 70/30 is supposed to provide higher surface coverage of leucine and a thicker leucine shell for better protection against moisture, the observed morphology of trehalose/leucine 80/20, with its higher surface corrugation, enhances powder dispersibility yet further.

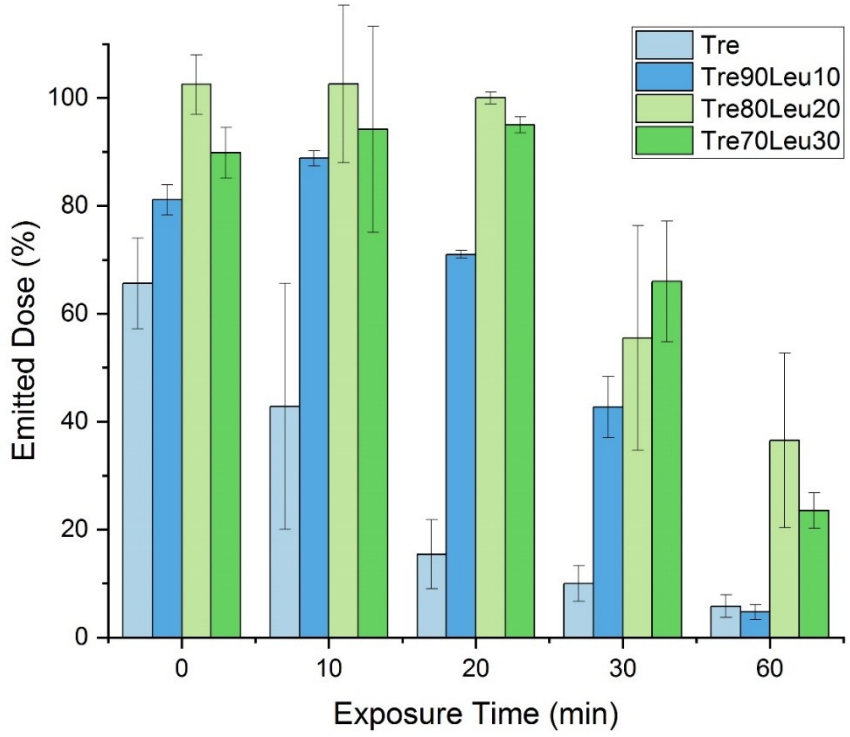

Figure 18 Emitted dose measurements at 15 L/min actuation flow rate for trehalose, trehalose/leucine 90/10, 80/20, and 70/30. These spray-dried powders were exposed to 90% RH and 25 °C for 0 min, 10 min, 20 min, 30 min, and 60 min. The error bars represent the percentage difference between the measurements.

3.3.5. Effects of moisture on particle morphology and crystallinity

The SEM images of the trehalose and the trehalose/leucine 90/10, 80/20, and 70/30 spray-dried particles after 30 min and 60 min exposure to humidity are shown in Figure 19 and Figure 20, respectively. From Figure 19, we can see that after 30 min exposure to humidity many trehalose particles were fused together, while no material bridging or fusing was observed between trehalose/leucine 90/10, 80/20, and 70/30 particles. All trehalose/leucine formulations were able to prevent particle fusing after 30 min exposure to humidity, thus maintaining powder dispersibility. In Figure 20, after 60 min exposure to humidity trehalose particles were no longer discernible; the material now had the appearance of large solid blocks. A high degree of fusing and loss of particle shape was also observed for trehalose/leucine 90/10. This observation agreed with the very low

emitted doses of trehalose and trehalose/leucine 90/10 particles after 60 min exposure to humidity. By contrast, a relatively low degree of fusing between particles was observed for trehalose/leucine 80/20 and 70/30, which agreed with their relatively higher emitted doses.

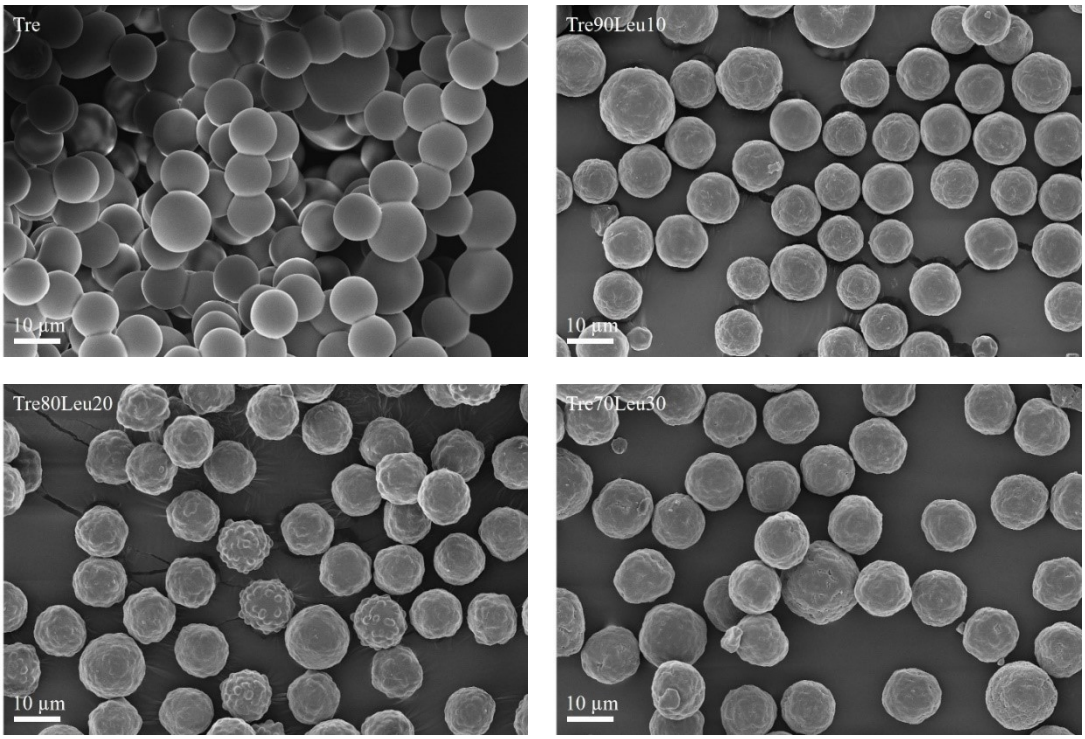

Figure 19 SEM images of spray-dried trehalose, and trehalose/leucine 90/10, 80/20, and 70/30 after 30 min exposure to 90% RH and 25 °C.

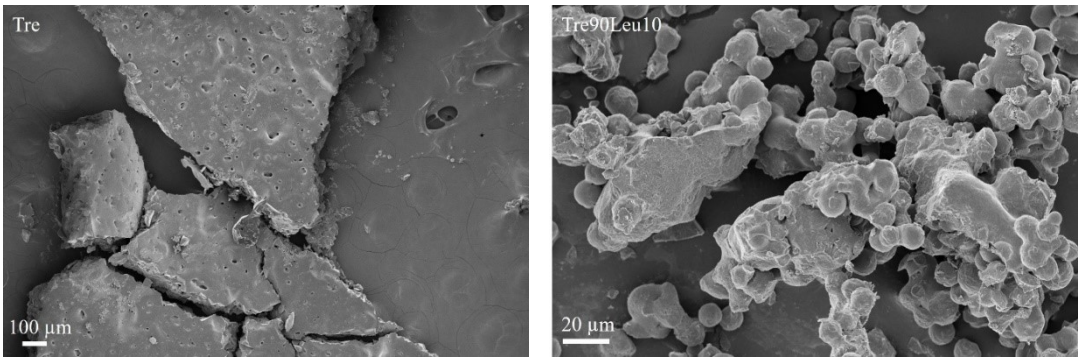

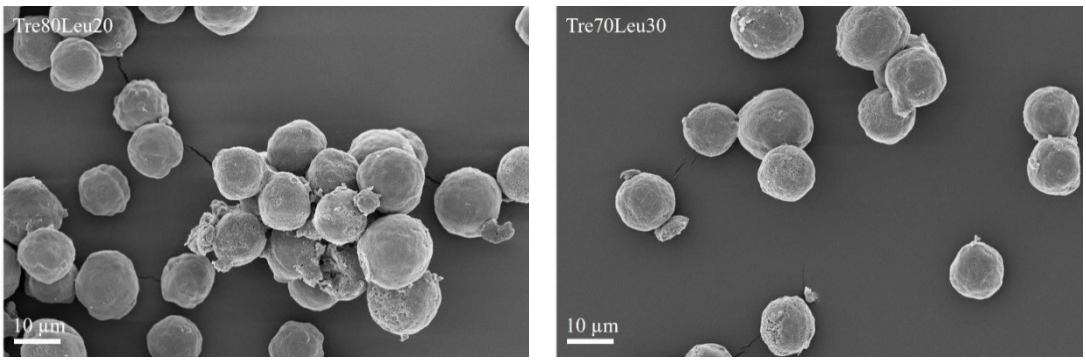

Figure 20 SEM images of spray-dried trehalose, and trehalose/leucine 90/10, 80/20, and 70/30 after 60 min exposure to 90% RH and 25 °C.

Raman spectroscopy analysis results for the spray-dried trehalose/leucine particles after 30 min exposure to 90% RH and 25 °C are shown in Figure 21. To verify the solid phase of trehalose, the crystalline leucine reference was subtracted from the spectra for trehalose/leucine 90/10, 80/20 and 70/30. The residual spectra as well as the spectrum of trehalose were very similar to the amorphous trehalose reference, and the characteristic sharp peaks from the crystalline trehalose were not detected, indicating its fully amorphous nature. Therefore, after 30 min exposure to 90% RH and 25 °C, the solid phase of trehalose was confirmed to be amorphous in all cases, irrespective of the presence of leucine. Raman spectra for the same formulations after 60 min exposure to 90% RH and 25 °C are shown in Figure 22. After subtraction of the crystalline leucine reference, the residual spectra are all similar to the crystalline trehalose reference, and no evidence of amorphous trehalose can be found. Therefore it can be concluded that after 60 min exposure to 90% RH and 25 °C, the trehalose had crystallized in all spray-dried trehalose/leucine and in the neat trehalose particles. The spectroscopy analysis shows that under these test conditions the addition of leucine does not change the crystallization behavior of trehalose. This result is not totally unexpected since the crystalline leucine shell is composed of a patchwork of individual leucine nanocrystals (Ordoubadi et al. 2020), and thus the shell does not prevent diffusion of water to the trehalose core. Although leucine may

not be able to prevent the plasticization of trehalose, the crystalline leucine shell can still preserve the powder dispersibility, even at a high water content in the particles.

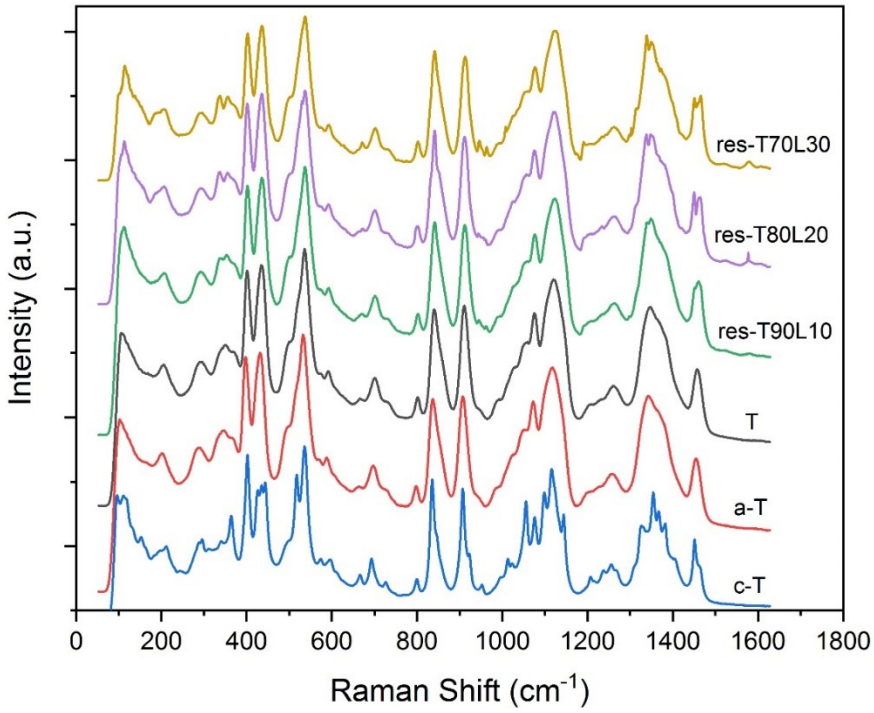

Figure 21 Raman spectroscopy analysis of spray-dried trehalose/leucine and pure trehalose particles after 30 min exposure to 90% RH and 25 °C. Legend: The spectra labeled "res-" are the residual spectra after the crystalline leucine reference has been subtracted from the three different spray-dried trehalose/leucine formulations, "T" is the spectrum of spray-dried pure trehalose particles, "a-T" is the amorphous trehalose reference, and "c-T" is the raw crystalline trehalose reference.

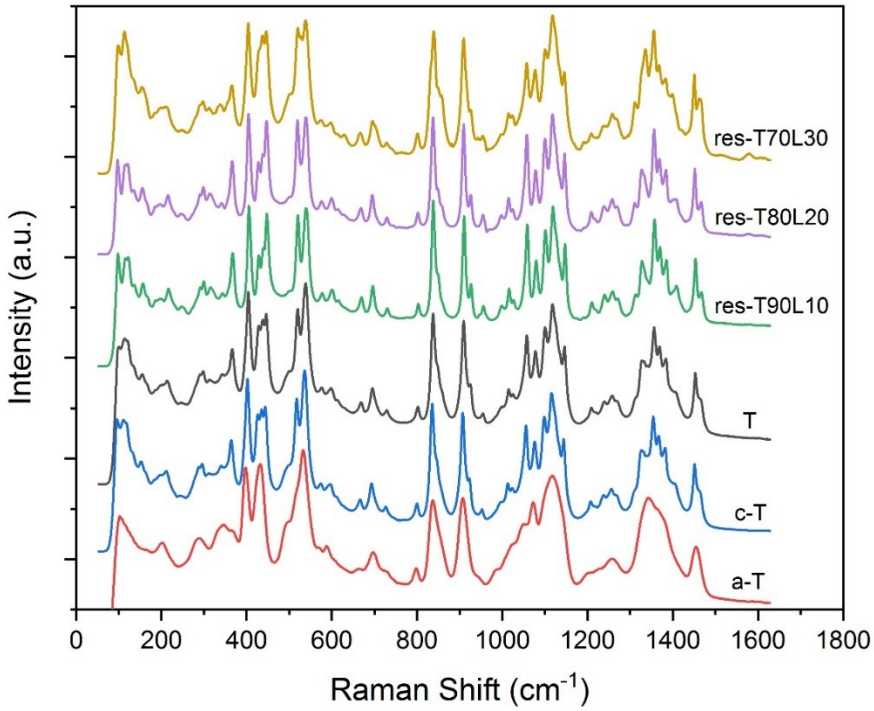

Figure 22 Raman spectroscopy analysis of spray-dried trehalose/leucine and pure trehalose particles after 60 min exposure to 90% RH and 25 °C. Legend: The spectra labeled "res-" are the residual spectra after the crystalline leucine reference has been subtracted from the three different spray-dried trehalose/leucine formulations, "T" is the spectrum of spray-dried pure trehalose particles, "c-T" is the raw crystalline trehalose reference, and "a-T" is the amorphous trehalose reference.

3.4. Conclusions

Unlike pure trehalose particles, leucine, trileucine, and pullulan as shell forming excipients were capable of maintaining powder dispersibility when exposed to a high-humidity environment in a simulated out-of-package scenario. The trehalose/leucine system was the most promising in protecting particles against moisture in a size range suitable for nasal delivery. The powder dispersibility of trehalose decreased quickly after 10 min exposure to 90% RH and 25 °C and decreased significantly after 30 min exposure, due to material bridging and fusing, while the trehalose/leucine system effectively reduced the effect of material bridging and fusing and improved

the powder dispersibility within 30 min exposure to a high-humidity environment. From the spectroscopy analysis, the crystalline leucine shell may not be able to prevent the water uptake and crystallization of trehalose, but it can nevertheless keep the powders dispersible even at a high moisture content. Thus, leucine may be considered an appropriate shell-forming excipient, providing robustness for nasal dry powder vaccines and other biologics for which a trehalose-based formulation platform is advantageous. Compared with particles for lung delivery, smaller amounts of leucine are needed to form a crystalline shell on large particles for nasal administration, thereby preserving a larger payload capacity in the particles. Future studies may investigate the surface composition of trehalose/leucine particles quantitatively to better understand the effect of leucine surface coverage using surface analysis techniques such as X-ray photoelectron spectroscopy.

3.5. References

Azhdarzadeh, M., Shemirani, F.M., Ruzycki, C.A., Baldelli, A., Ivey, J., Barona, D., Church, T., Lewis, D., Olfert, J.S., Finlay, W.H., and Vehring, R. (2016). An atomizer to generate monodisperse droplets from high vapor pressure liquids. *At. Sprays,* 26(2):121–134.

Baldelli, A. and Vehring, R. (2016). Analysis of cohesion forces between monodisperse microparticles with rough surfaces. *Colloids Surfaces A Physicochem. Eng. Asp.,* 506:179–189.

Bartos, C., Pallagi, E., Szabó-Révész, P., Ambrus, R., Katona, G., Kiss, T., Rahimi, M., and Csóka, I. (2018). Formulation of levodopa containing dry powder for nasal delivery applying the quality-by-design approach. *Eur. J. Pharm. Sci.,* 123(March):475–483.

Boraey, M.A., Hoe, S., Sharif, H., Miller, D.P., Lechuga-Ballesteros, D., and Vehring, R. (2013). Improvement of the dispersibility of spray-dried budesonide powders using leucine in an ethanol-water cosolvent system. *Powder Technol.,* 236:171–178.

Boraey, M.A. and Vehring, R. (2014). Diffusion controlled formation of microparticles. *J. Aerosol Sci.,* 67:131–143.

Carrigy, N.B., Ordoubadi, M., Liu, Y., Melhem, O., Barona, D., Wang, H., Milburn, L., Ruzycki, C.A., Finlay, W.H., and Vehring, R. (2019). Amorphous pullulan trehalose microparticle platform for respiratory delivery. *Int. J. Pharm.,* 563(March):156–168.

Carrigy, N.B. and Vehring, R. (2019). Engineering stable spray-dried biologic powder for inhalation*., in Pharmaceutical Inhalation Aerosol Technology, A.J. Hickey, S.R. da Rocha, eds,* pp. 291–326.

Cui, Y., Zhang, X., Wang, W., Huang, Z., Zhao, Z., Wang, G., Cai, S., Jing, H., Huang, Y., Pan, X., and Wu, C. (2018). Moisture-resistant co-spray-dried netilmicin with l-leucine as dry powder inhalation for the treatment of respiratory infections. *Pharmaceutics,* 10(4).

Feng, A.L., Boraey, M.A., Gwin, M.A., Finlay, P.R., Kuehl, P.J., and Vehring, R. (2011). Mechanistic models facilitate efficient development of leucine containing microparticles for pulmonary drug delivery. *Int. J. Pharm.,* 409(1–2):156–163.

Garmise, R.J., Mar, K., Crowder, T.M., Hwang, C.R., Ferriter, M., Huang, J., Mikszta, J.A., Sullivan, V.J., and Hickey, A.J. (2006). Formulation of a dry powder influenza vaccine for nasal delivery. *AAPS PharmSciTech,* 7(1):1–7.

Garmise, R.J., Staats, H.F., and Hickey, A.J. (2007). Novel dry powder preparations of whole inactivated influenza virus for nasal vaccination. *AAPS PharmSciTech,* 8(4).

Hancock, B.C., Dalton, C.R., 1999. The Effect of Temperature on Water Vapor Sorption by Some Amorphous Pharmaceutical Sugars. *Pharm. Dev. Technol.* 4, 125–131. https://doi.org/10.1080/10837459908984232

Illum, L. (2003). Nasal drug delivery - Possibilities, problems and solutions. *J. Control. Release,* 87(1–3):187–198.

Illum, L. (2002). Nasal drug delivery: New developments and strategies. *Drug Discov. Today,* 7(23):1184–1189.

Ishikawa, F., Murano, M., Hiraishi, M., Yamaguchi, T., Tamai, I., and Tsuji, A. (2002). Insoluble powder formulation as an effective nasal drug delivery system. *Pharm. Res.,* 19(8):1097–1104.

Ivey, J.W., Bhambri, P., Church, T.K., Lewis, D.A., and Vehring, R. (2018). Experimental investigations of particle formation from propellant and solvent droplets using a monodisperse spray dryer. *Aerosol Sci. Technol.,* 52(6):702–716.

Lechuga-Ballesteros, D., Charan, C., Stults, C.L.M., Stevenson, C.L., Miller, D.P., Vehring, R., Tep, V., and Kuo, M.C. (2008). Trileucine improves aerosol performance and stability of spray-dried powders for inhalation. *J. Pharm. Sci.,* 97(1):287–302.

Lechuga-Ballesteros, D., Charan, C., Stults, C.L.M., Stevenson, C.L., Miller, D.P., Vehring, R., Tep, V., and Kuo, M. (2008). Trileucine improves aerosol performance and stability of spray-dried powders for inhalation. *J. Pharm. Sci.,* 97(1):287–302.

Li, L., Leung, S.S.Y., Gengenbach, T., Yu, J., Gao, G. (Fiona), Tang, P., Zhou, Q. (Tony), and Chan, H.K. (2017). Investigation of L-leucine in reducing the moisture-induced deterioration of spray-dried salbutamol sulfate power for inhalation. *Int. J. Pharm.,* 530(1–2):30–39.

Li, L., Sun, S., Parumasivam, T., Denman, J.A., Gengenbach, T., Tang, P., Mao, S., and Chan, H.K. (2016). L-Leucine as an excipient against moisture on in vitro aerosolization performances of highly hygroscopic spray-dried powders. *Eur. J. Pharm. Biopharm.,* 102:132–141.

Ordoubadi, M., Gregson, F.K.A., Melhem, O., Barona, D., Miles, R.E.H., D'Sa, D., Gracin, S., Lechuga-Ballesteros, D., Reid, J.P., Finlay, W.H., and Vehring, R. (2019). Multi-Solvent Microdroplet Evaporation: Modeling and Measurement of Spray-Drying Kinetics with Inhalable Pharmaceutics. *Pharm. Res.,* 36(7).

Ordoubadi, M., Gregson, F.K.A., Wang, H., Carrigy, N.B., Nicholas, M., Gracin, S., Lechuga-Ballesteros, D., Reid, J.P., Finlay, W.H., and Vehring, R. (2021). Trileucine as a Dispersibility Enhancer of Spray-Dried Inhalable Microparticles. Manuscript submitted for

publication.
Ordoubadi, M., Gregson, F.K.A., Wang, H., Nicholas, M., Gracin, S., Lechuga-Ballesteros, D., Reid, J.P., Finlay, W.H., and Vehring, R. (2020). On the particle formation of leucine in spray drying of inhalable microparticles. *Int. J. Pharm.,* (November):120102.
Pozzoli, M., Rogueda, P., Zhu, B., Smith, T., Young, P.M., Traini, D., and Sonvico, F. (2016). Dry powder nasal drug delivery: challenges, opportunities and a study of the commercial Teijin Puvlizer Rhinocort device and formulation. *Drug Dev. Ind. Pharm.,* 42(10):1660–1668.
Schroeter, J.D., Garcia, G.J.M., and Kimbell, J.S. (2011). Effects of surface smoothness on inertial particle deposition in human nasal models. *J. Aerosol Sci.,* 42(1):52–63.
Schroeter, J.D., Tewksbury, E.W., Wong, B.A., and Kimbell, J.S. (2015). Experimental measurements and computational predictions of regional particle deposition in a sectional nasal model. *J. Aerosol Med. Pulm. Drug Deliv.,* 28(1):20–29.
Shetty, N., Park, H., Zemlyanov, D., Mangal, S., Bhujbal, S., and Zhou, Q. (Tony) (2018). Influence of excipients on physical and aerosolization stability of spray dried high-dose powder formulations for inhalation. *Int. J. Pharm.,* 544(1):222–234.
Sibum, I., Hagedoorn, P., Kluitman, M.P.G., Kloezen, M., Frijlink, H.W., and Grasmeijer, F. (2020). Dispersibility and storage stability optimization of high dose isoniazid dry powder inhalation formulations with L-leucine or trileucine. *Pharmaceutics,* 12(1):1–14.
Trows, S. and Scherließ, R. (2016). Carrier-based dry powder formulation for nasal delivery of vaccines utilizing BSA as model drug. *Powder Technol.,* 292:223–231.
Vehring, R. (2008). Pharmaceutical particle engineering via spray drying. *Pharm. Res.,* 25(5):999–1022.
Wang, H., Barona, D., Oladepo, S., Williams, L., Hoe, S., Lechuga-Ballesteros, D., and Vehring, R. (2017). Macro-Raman spectroscopy for bulk composition and homogeneity analysis of multi-component pharmaceutical powders. *J. Pharm. Biomed. Anal.,* 141:180–191.
Wang, H., Nobes, D.S., and Vehring, R. (2019). Particle Surface Roughness Improves Colloidal Stability of Pressurized Pharmaceutical Suspensions. *Pharm. Res.,* 36(3):1–17.
Wang, S.H., Kirwan, S.M., Abraham, S.N., Staats, H.F., and Hickey, A.J. (2012). Stable dry powder formulation for nasal delivery of anthrax vaccine. *J. Pharm. Sci.,* 101(1):31–47.
Wang, Z., Ordoubadi, M., Wang, H., and Vehring, R. (2021). Morphology and Formation of Crystalline Leucine Microparticles from a co-Solvent System using Multi-Orifice Monodisperse Spray Drying. *Aerosol Science and Technology*, 2021, doi 10.1080/02786826.2021.1904129.
Weiler, C., Egen, M., Trunk, M., and Langguth, P. (2010). Force control and powder dispersibility of spray dried particles for inhalation. *J. Pharm. Sci.,* 99(1):303–316.
Wu, W.D., Patel, K.C., Rogers, S., and Chen, X.D. (2007). Monodisperse droplet generators as potential atomizers for spray drying technology. *Dry. Technol.,* 25(12):1907–1916.
Zhou, Q., Gengenbach, T., Denman, J.A., Yu, H.H., Li, J., and Chan, H.K. (2014). Synergistic antibiotic combination powders of colistin and rifampicin provide high aerosolization efficiency and moisture protection. *AAPS J.,* 16(1):37–47.

Chapter 4. Conclusion

Monodisperse spray drying has the advantage of producing uniform particles, which reduces complexities in studying droplet-size-sensitive objects over polydisperse spray drying. However, the low powder production rate of monodisperse spray drying produces insufficient sample masses for typical powder assays, thus limiting the use of monodisperse spray drying in research studies. In this study, monodisperse spray drying was scaled up to produce sufficient powder masses for typical powder assays. Using scaled-up monodisperse spray drying, the crystallization kinetics of spray-dried leucine particles and the environmental robustness of three two-component particle systems were then investigated.

In Chapter 2, Ga-FIB-manufactured dual-orifice plate was demonstrated to successfully increase the powder production rate of monodisperse spray drying while maintaining the monodispersity of the spray-dried particles. However, several improvements should be considered in future research, including plates with more than two orifices for tests requiring larger sample masses, smaller orifices for efficient production of respirable powders, and more economical and efficient manufacturing techniques to reduce the high costs and long operating time of Ga-FIB milling. The crystallization kinetics of spray-dried leucine particles from a co-solvent system were investigated utilizing the scaled-up monodisperse spray drying. The results indicated that co-solvent ratio and spray drying temperature are two important parameters controlling the time available for crystallization and, consequently, the crystallization kinetics. Lower water/ethanol ratios and lower spray drying temperatures correspond to a longer time available for crystallization and more stable porous particles with large crystal size, while higher water/ethanol ratios and higher spray drying temperatures correspond to a shorter time available for crystallization and hollow and fragile

particles composed of nanocrystals. These results highlight the importance of carefully controlling the co-solvent ratio and spray drying temperature during particle design and manufacturing processes in order to achieve desired product properties.

The environmental robustness of trehalose in combination with leucine, pullulan, or trileucine was investigated using the scaled-up monodisperse spray drying presented in Chapter 3. All three shell-forming excipients were found capable of protecting the trehalose against moisture and maintaining its powder dispersibility, while the trehalose/leucine was the most promising system in a size range suitable for nasal drug delivery. It was found that as low as 10% leucine in the formulation can form a crystalline leucine shell and provide protection. Although spectroscopy analysis indicated that the crystalline leucine shell may not be able to prevent the moisture uptake and crystallization of trehalose, the powder dispersibility can still be well maintained even at a high moisture content in the particles. Therefore, leucine is a promising shell-forming excipient to provide environmental robustness for a trehalose-based formulation platform for nasal dry powder delivery.

References

Arpagaus, C., Collenberg, A., Rütti, D., Assadpour, E., and Jafari, S.M. (2018). Nano spray drying for encapsulation of pharmaceuticals. *Int. J. Pharm.,* 546(1–2):194–214.

Azhdarzadeh, M., Shemirani, F.M., Ruzycki, C.A., Baldelli, A., Ivey, J., Barona, D., Church, T., Lewis, D., Olfert, J.S., Finlay, W.H., and Vehring, R. (2016). An atomizer to generate monodisperse droplets from high vapor pressure liquids. *At. Sprays,* 26(2):121–134.

Baldelli, A., Power, R.M., Miles, R.E.H., Reid, J.P., and Vehring, R. (2016). Effect of crystallization kinetics on the properties of spray dried microparticles. *Aerosol Sci. Technol.,* 50(7):693–704.

Baldelli, A. and Vehring, R. (2016a). Control of the radial distribution of chemical components in spray-dried crystalline microparticles. *Aerosol Sci. Technol.,* 50(10):1130–1142.

Baldelli, A. and Vehring, R. (2016b). Analysis of cohesion forces between monodisperse microparticles with rough surfaces. *Colloids Surfaces A Physicochem. Eng. Asp.,* 506:179–189.

Bartos, C., Pallagi, E., Szabó-Révész, P., Ambrus, R., Katona, G., Kiss, T., Rahimi, M., and Csóka, I. (2018). Formulation of levodopa containing dry powder for nasal delivery applying the quality-by-design approach. *Eur. J. Pharm. Sci.,* 123(March):475–483.

Bayvel, L. and Orzechowski, Z. (1993). Liquid Atomization. Taylor & Francis.

Boraey, M.A., Hoe, S., Sharif, H., Miller, D.P., Lechuga-Ballesteros, D., and Vehring, R. (2013). Improvement of the dispersibility of spray-dried budesonide powders using leucine in an ethanol-water cosolvent system. *Powder Technol.,* 236:171–178.

Boraey, M.A. and Vehring, R. (2014). Diffusion controlled formation of microparticles. *J. Aerosol Sci.,* 67:131–143.

Brenn, G., Durst, F., and Tropea, C. (1996). Monodisperse sprays for various purposes - Their production and characteristics. *Part. Part. Syst. Charact.,* 13(3):179–185.

Brenn, G., Helpiö, T., and Durst, F. (1997). A new apparatus for the production of monodisperse sprays at high flow rates. *Chem. Eng. Sci.,* 52(2):237–244.

Cal, K. and Sollohub, K. (2010). Spray drying technique. I: Hardware and process parameters. *J. Pharm. Sci.,* 99(2):575–586.

Carr, A.G., Mammucari, R., and Foster, N.R. (2011). Particle formation of budesonide from alcohol-modified subcritical water solutions. *Int. J. Pharm.,* 405(1–2):169–180.

Carrigy, N.B., Ordoubadi, M., Liu, Y., Melhem, O., Barona, D., Wang, H., Milburn, L., Ruzycki, C.A., Finlay, W.H., and Vehring, R. (2019). Amorphous pullulan trehalose microparticle platform for respiratory delivery. *Int. J. Pharm.,* 563(March):156–168.

Carrigy, N.B. and Vehring, R. (2019). Engineering stable spray-dried biologic powder for inhalation*., in Pharmaceutical Inhalation Aerosol Technology, A.J. Hickey, S.R. da Rocha, eds,* pp. 291–326.

Christoffersen, J., Rostrup, E., and Christoffersen, M.R. (1991). Relation between interfacial surface tension of electrolyte crystals in aqueous suspension and their solubility; a simple derivation based on surface nucleation. *J. Cryst. Growth,* 113(3–4):599–605.

Cui, Y., Zhang, X., Wang, W., Huang, Z., Zhao, Z., Wang, G., Cai, S., Jing, H., Huang, Y., Pan, X., and Wu, C. (2018). Moisture-resistant co-spray-dried netilmicin with l-leucine as dry powder

inhalation for the treatment of respiratory infections. *Pharmaceutics,* 10(4).

Dumouchel, C. (2008). On the experimental investigation on primary atomization of liquid streams. *Exp. Fluids,* 45(3):371–422.

Erbay, Z., Koca, N., Kaymak-ertekin, F., and Ucuncu, M. (2014). Optimization of spray drying process in cheese. *Food Bioprod. Process.,* 93(April 2013):156–165.

Feng, A.L., Boraey, M.A., Gwin, M.A., Finlay, P.R., Kuehl, P.J., and Vehring, R. (2011). Mechanistic models facilitate efficient development of leucine containing microparticles for pulmonary drug delivery. *Int. J. Pharm.,* 409(1–2):156–163.

Fu, N., Zhou, Z., Jones, T.B., Tan, T.T.Y., Wu, W.D., Lin, S.X., Chen, X.D., and Chan, P.P.Y. (2011). Production of monodisperse epigallocatechin gallate (EGCG) microparticles by spray drying for high antioxidant activity retention. *Int. J. Pharm.,* 413(1–2):155–166.

Garmise, R.J., Mar, K., Crowder, T.M., Hwang, C.R., Ferriter, M., Huang, J., Mikszta, J.A., Sullivan, V.J., and Hickey, A.J. (2006). Formulation of a dry powder influenza vaccine for nasal delivery. *AAPS PharmSciTech,* 7(1):1–7.

Garmise, R.J., Staats, H.F., and Hickey, A.J. (2007). Novel dry powder preparations of whole inactivated influenza virus for nasal vaccination. *AAPS PharmSciTech,* 8(4).

Gharsallaoui, A., Roudaut, G., Chambin, O., Voilley, A., and Saurel, R. (2007). Applications of spray-drying in microencapsulation of food ingredients: An overview. *Food Res. Int.,* 40(9):1107–1121.

Hancock, B.C., Dalton, C.R., 1999. The Effect of Temperature on Water Vapor Sorption by Some Amorphous Pharmaceutical Sugars. *Pharm. Dev. Technol.* 4, 125–131. https://doi.org/10.1080/10837459908984232

Handscomb, C.S., Kraft, M., and Bayly, A.E. (2009). A new model for the drying of droplets containing suspended solids. *Chem. Eng. Sci.,* 64(4):628–637.

He, G., Bhamidi, V., Tan, R.B.H., Kenis, P.J.A., and Zukoski, C.F. (2006). Determination of critical supersaturation from microdroplet evaporation experiments. *Cryst. Growth Des.,* 6(5):1175–1180.

Huang, L.X., Kumar, K., and Mujumdar, A.S. (2006). A comparative study of a spray dryer with rotary disc atomizer and pressure nozzle using computational fluid dynamic simulations. *Chem. Eng. Process. Process Intensif.,* 45(6):461–470.

Illum, L. (2003). Nasal drug delivery - Possibilities, problems and solutions. *J. Control. Release,* 87(1–3):187–198.

Illum, L. (2002). Nasal drug delivery: New developments and strategies. *Drug Discov. Today,* 7(23):1184–1189.

Ishikawa, F., Murano, M., Hiraishi, M., Yamaguchi, T., Tamai, I., and Tsuji, A. (2002). Insoluble powder formulation as an effective nasal drug delivery system. *Pharm. Res.,* 19(8):1097–1104.

Ivey, J.W. (2018). Particle Formation from Evaporating Microdroplets for Inhaled Drug Delivery. University of Alberta.

Ivey, J.W., Bhambri, P., Church, T.K., Lewis, D.A., and Vehring, R. (2018). Experimental investigations of particle formation from propellant and solvent droplets using a monodisperse spray dryer. *Aerosol Sci. Technol.,* 52(6):702–716.

Jain, M., Lohare, G., Bari, M., Chavan, R., Barhate, S., and Shah, C. (2012). Spray Drying in Pharmaceutical Industry: A Review. *Res. J. Pharm. Dos. Forms Technol.,* 4(2):74–79.

Lechuga-Ballesteros, D., Charan, C., Stults, C.L.M., Stevenson, C.L., Miller, D.P., Vehring, R., Tep, V., and Kuo, M.C. (2008). Trileucine improves aerosol performance and stability of spray-dried powders for inhalation. *J. Pharm. Sci.,* 97(1):287–302.

Lechuga-Ballesteros, D., Charan, C., Stults, C.L.M., Stevenson, C.L., Miller, D.P., Vehring, R., Tep, V., and Kuo, M. (2008). Trileucine improves aerosol performance and stability of spray-dried powders for inhalation. *J. Pharm. Sci.,* 97(1):287–302.

Lee, Y.Y., Wu, J.X., Yang, M., Young, P.M., Van Den Berg, F., and Rantanen, J. (2011). Particle size dependence of polymorphism in spray-dried mannitol. *Eur. J. Pharm. Sci.,* 44(1–2):41–48.

Li, L., Leung, S.S.Y., Gengenbach, T., Yu, J., Gao, G. (Fiona), Tang, P., Zhou, Q. (Tony), and Chan, H.K. (2017). Investigation of L-leucine in reducing the moisture-induced deterioration of spray-dried salbutamol sulfate power for inhalation. *Int. J. Pharm.,* 530(1–2):30–39.

Li, L., Sun, S., Parumasivam, T., Denman, J.A., Gengenbach, T., Tang, P., Mao, S., and Chan, H.K. (2016). L-Leucine as an excipient against moisture on in vitro aerosolization performances of highly hygroscopic spray-dried powders. *Eur. J. Pharm. Biopharm.,* 102:132–141.

Lin, S P and Reitz, R.D. (1998). Drop and Spray Formation. *Annu. Rev. Fluid Mech.,* 30:85–105.

Liu, W., Chen, X.D., and Selomulya, C. (2015). On the spray drying of uniform functional microparticles. *Particuology,* 22:1–12.

Liu, W., Wu, W.D., Selomulya, C., and Chen, X.D. (2011). Uniform chitosan microparticles prepared by a novel spray-drying technique. *Int. J. Chem. Eng.,* 2011.

Lu, W., Wang, S., Lin, R., Yang, X., and Cheng, Z. (2020). Unveiling the importance of process parameters on droplet shrinkage and crystallization behaviors of easily crystalline material during spray drying. *Dry. Technol.,* 0(0):1–11.

Lucas, P., Kerry, A., Potter, U.J., and Staniforth, J.N. (1999). Enhancement of Small Particle Size Dry Powder Aerosol Formulations using an Ultra Low Density Additive. *Pharm. Res.,* 16:1643–1647.

McDonagh, A.F. and Tajber, L. (2019). The control of paracetamol particle size and surface morphology through crystallisation in a spray dryer. *Adv. Powder Technol.,* 31(1):287–299.

Mehanna, M.M., Mohyeldin, S.M., and Elgindy, N.A. (2014). Respirable nanocarriers as a promising strategy for antitubercular drug delivery. *J. Control. Release,* 187:183–197.

Najafabadi, A.R., Gilani, K., Barghi, M., and Rafiee-Tehrani, M. (2004). The effect of vehicle on physical properties and aerosolisation behaviour of disodium cromoglycate microparticles spray dried alone or with L-leucine. *Int. J. Pharm.,* 285(1–2):97–108.

Ordoubadi, M., Gregson, F.K.A., Melhem, O., Barona, D., Miles, R.E.H., D'Sa, D., Gracin, S., Lechuga-Ballesteros, D., Reid, J.P., Finlay, W.H., and Vehring, R. (2019). Multi-Solvent Microdroplet Evaporation: Modeling and Measurement of Spray-Drying Kinetics with Inhalable Pharmaceutics. *Pharm. Res.,* 36(7).

Ordoubadi, M., Gregson, F.K.A., Wang, H., Carrigy, N.B., Nicholas, M., Gracin, S., Lechuga-Ballesteros, D., Reid, J.P., Finlay, W.H., and Vehring, R. (2021). Trileucine as a Dispersibility Enhancer of Spray-Dried Inhalable Microparticles. Manuscript submitted for publication.

Ordoubadi, M., Gregson, F.K.A., Wang, H., Nicholas, M., Gracin, S., Lechuga-Ballesteros, D., Reid, J.P., Finlay, W.H., and Vehring, R. (2020). On the particle formation of leucine in spray

drying of inhalable microparticles. *Int. J. Pharm.,* (November):120102.

Patel, K.C. and Chen, X.D. (2007). Production of spherical and uniform-sized particles using a laboratory ink-jet spray dryer. *Asia-Pacific J. Chem. Eng.,* 2(5):415–430.

Plateau, J. (1873). Statique expérimentale et théorique des liquides soumis aux seules forces moléculaires.

Pozzoli, M., Rogueda, P., Zhu, B., Smith, T., Young, P.M., Traini, D., and Sonvico, F. (2016). Dry powder nasal drug delivery: challenges, opportunities and a study of the commercial Teijin Puvlizer Rhinocort device and formulation. *Drug Dev. Ind. Pharm.,* 42(10):1660–1668.

PubChem (n.d.). Leucine. Available at https://pubchem.ncbi.nlm.nih.gov/compound/Leucine (Accessed 1 December 2020).

Ranz, W.E. (1956). On spray and spraying.

Rayleigh, Lord (1878). On the Instability of Jets. *Proc. London Math. Soc.,* s1-10(1):4–13.

Rogers, S., Fang, Y., Qi Lin, S.X., Selomulya, C., and Dong Chen, X. (2012a). A monodisperse spray dryer for milk powder: Modelling the formation of insoluble material. *Chem. Eng. Sci.,* 71:75–84.

Rogers, S., Wu, W.D., Lin, S.X.Q., and Chen, X.D. (2012b). Particle shrinkage and morphology of milk powder made with a monodisperse spray dryer. *Biochem. Eng. J.,* 62:92–100.

Schmitz-Schug, I., Kulozik, U., and Foerst, P. (2016). Modeling spray drying of dairy products - Impact of drying kinetics, reaction kinetics and spray drying conditions on lysine loss. *Chem. Eng. Sci.,* 141:315–329.

Schroeter, J.D., Garcia, G.J.M., and Kimbell, J.S. (2011). Effects of surface smoothness on inertial particle deposition in human nasal models. *J. Aerosol Sci.,* 42(1):52–63.

Schroeter, J.D., Tewksbury, E.W., Wong, B.A., and Kimbell, J.S. (2015). Experimental measurements and computational predictions of regional particle deposition in a sectional nasal model. *J. Aerosol Med. Pulm. Drug Deliv.,* 28(1):20–29.

Seydel, P., Blömer, J., and Bertling, J. (2006). Modeling particle formation at spray drying using population balances. *Dry. Technol.,* 24(2):137–146.

Shetty, N., Park, H., Zemlyanov, D., Mangal, S., Bhujbal, S., and Zhou, Q. (Tony) (2018). Influence of excipients on physical and aerosolization stability of spray dried high-dose powder formulations for inhalation. *Int. J. Pharm.,* 544(1):222–234.

Shishir, M.R.I. and Chen, W. (2017). Trends of spray drying: A critical review on drying of fruit and vegetable juices. *Trends Food Sci. Technol.,* 65:49–67.

Sibum, I., Hagedoorn, P., Kluitman, M.P.G., Kloezen, M., Frijlink, H.W., and Grasmeijer, F. (2020). Dispersibility and storage stability optimization of high dose isoniazid dry powder inhalation formulations with L-leucine or trileucine. *Pharmaceutics,* 12(1):1–14.

Sosnik, A. and Seremeta, K.P. (2015). Advantages and challenges of the spray-drying technology for the production of pure drug particles and drug-loaded polymeric carriers. *Adv. Colloid Interface Sci.,* 223:40–54.

Sterling, A.M. and Sleicher, C.A. (1975). The instability of capillary jets. *J. Fluid Mech.,* 68(3):477–495.

Tontul, I. and Topuz, A. (2017). Spray-drying of fruit and vegetable juices: Effect of drying conditions on the product yield and physical properties. *Trends Food Sci. Technol.,* 63:91–102.

Trows, S. and Scherließ, R. (2016). Carrier-based dry powder formulation for nasal delivery of

vaccines utilizing BSA as model drug. *Powder Technol.,* 292:223–231.

Vehring, R. (2008). Pharmaceutical particle engineering via spray drying. *Pharm. Res.,* 25(5):999–1022.

Vehring, R., Foss, W.R., and Lechuga-Ballesteros, D. (2007). Particle formation in spray drying. *J. Aerosol Sci.,* 38(7):728–746.

Walton, D.E. (2000). The morphology of spray-dried particles a qualitative view. *Dry. Technol.,* 18(9):1943–1986.

Wang, H., Barona, D., Oladepo, S., Williams, L., Hoe, S., Lechuga-Ballesteros, D., and Vehring, R. (2017). Macro-Raman spectroscopy for bulk composition and homogeneity analysis of multi-component pharmaceutical powders. *J. Pharm. Biomed. Anal.,* 141:180–191.

Wang, H., Boraey, M.A., Williams, L., Lechuga-Ballesteros, D., and Vehring, R. (2014). Low-frequency shift dispersive Raman spectroscopy for the analysis of respirable dosage forms. *Int. J. Pharm.,* 469(1):197–205.

Wang, H., Nobes, D.S., and Vehring, R. (2019). Particle Surface Roughness Improves Colloidal Stability of Pressurized Pharmaceutical Suspensions. *Pharm. Res.,* 36(3):1–17.

Wang, S.H., Kirwan, S.M., Abraham, S.N., Staats, H.F., and Hickey, A.J. (2012). Stable dry powder formulation for nasal delivery of anthrax vaccine. *J. Pharm. Sci.,* 101(1):31–47.

Wang, Z., Ordoubadi, M., Wang, H., and Vehring, R. (2021). Morphology and Formation of Crystalline Leucine Microparticles from a co-Solvent System using Multi-Orifice Monodisperse Spray Drying. *Aerosol Science and Technology*, 2021, doi 10.1080/02786826.2021.1904129.

Weber, C. (1931). Zum Zerfall eines Flüssigkeitsstrahles. *ZAMM - J. Appl. Math. Mech. / Zeitschrift für Angew. Math. und Mech.,* 11(2):136–154.

Weiler, C., Egen, M., Trunk, M., and Langguth, P. (2010). Force control and powder dispersibility of spray dried particles for inhalation. *J. Pharm. Sci.,* 99(1):303–316.

Wisniewski, R. (2015). Spray Drying Technology Review. *Int. Conf. Environ. Syst.,* (July):1–9.

Wu, W.D., Patel, K.C., Rogers, S., and Chen, X.D. (2007). Monodisperse droplet generators as potential atomizers for spray drying technology. *Dry. Technol.,* 25(12):1907–1916.

Zhou, H., Hu, Z., Zhang, Q., Wang, Q., and Lv, X. (2019). Numerical study on gas-solid flow characteristics of ultra-light particles in a cyclone separator. *Powder Technol.,* 344:784–796.

Zhou, Q., Gengenbach, T., Denman, J.A., Yu, H.H., Li, J., and Chan, H.K. (2014). Synergistic antibiotic combination powders of colistin and rifampicin provide high aerosolization efficiency and moisture protection. *AAPS J.,* 16(1):37–47.

Ziaee, A., Albadarin, A.B., Padrela, L., Femmer, T., O'Reilly, E., and Walker, G. (2019). Spray drying of pharmaceuticals and biopharmaceuticals: Critical parameters and experimental process optimization approaches. *Eur. J. Pharm. Sci.,* 127(January 2019):300–318.